



UNITED AIRCRAFT CORPORATION

United Aircraft Research Laboratories

EAST HARTFORD, CONNECTICUT



JRM 602	N70 - 35832	(THRU)
	109	1
FAC	CR-113099	(CATEGORY)
	7	20

(ACCESSION NUMBER) (NASA CR OR TMX OR AD NUMBER)

Reproduced by
**NATIONAL TECHNICAL
INFORMATION SERVICE**
Springfield, Va 22151

United Aircraft Research Laboratories



EAST HARTFORD, CONNECTICUT

Report J910563-14

Further Research on Instabilities in
Atmospheric Flow Systems Associated
with Clear Air Turbulence

NASA Contract NASW-1582

REPORTED BY Richard C Stoeffler
Richard C. Stoeffler

APPROVED BY James W Clark
James W. Clark, Chief
Fluid and Systems Dynamics

DATE June 1970

NO OF PAGES 105

COPY NO

FOREWORD

Analytical and experimental fluid mechanics investigations were performed to investigate instabilities in atmospheric flow systems associated with clear air turbulence. This research was a continuation of investigations reported in NASA Contractor Report CR-1604. The program was conducted by United Aircraft Research Laboratories under Contract NASW-1582 with National Aeronautics and Space Administration Headquarters, Washington, D. C., 20546. The program was under the technical direction of the Chief, Fluid Dynamics Branch, Code RRF, Office of Advanced Research and Technology.

Report J910563-14

Further Research on Instabilities in Atmospheric Flow
Systems Associated with Clear Air Turbulence

TABLE OF CONTENTS

	<u>Page</u>
SUMMARY	1
RESULTS AND CONCLUSIONS	2
INTRODUCTION.	4
STABILITY OF TWO-DIMENSIONAL, STRAIGHT, STRATIFIED SHEAR FLOWS HAVING "S-SHAPED" VELOCITY PROFILES.	6
Review of Flows Having Hyperbolic Tangent Profiles	6
Stability Criteria of Hazel for "S-Shaped" Velocity Profiles	9
Summary of Experiments with "S-Shaped" Velocity Profiles	11
Concluding Remarks	13
INTERACTION OF LONG-WAVELENGTH WAVES WITH TWO-DIMENSIONAL, STRAIGHT, STRATIFIED SHEAR FLOWS	16
Theoretical Criteria of Phillips and Haurwitz	16
Summary of Experimental Results.	20
Concluding Remarks	24
APPLICATION TO ATMOSPHERIC SHEAR FLOWS.	25
Review of the Fundamental Flow Phenomenon.	25
Wavelengths of Instabilities that Might Occur.	27
Analyses of CAT Associated with Mountain Lee Waves	28
Analyses of CAT Over Thunderstorms	39
Concluding Remarks	41
RECOMMENDATIONS FOR "IN SITU" MEASUREMENTS OF CAT ENCOUNTERS AND IMPROVED METHODS FOR PREDICTING CAT	43
"In Situ" Measurements	43
Improved CAT Prediction Methods.	47

TABLE OF CONTENTS (Continued)

	<u>Page</u>
REFERENCES	51
LIST OF SYMBOLS.	53
Appendix I - DESCRIPTION OF EQUIPMENT AND PROCEDURES	56
II - METHOD FOR FITTING HAZEL'S THEORETICAL VELOCITY PROFILE TO DATA FOR "S-SHAPED" VELOCITY PROFILES.	59
III - PRELIMINARY STUDIES OF THE STABILITY OF "THREE-DIMENSIONAL", STRAIGHT, STRATIFIED SHEAR FLOWS.	61

TABLE

FIGURES

Further Research on Instabilities in Atmospheric Flow
Systems Associated with Clear Air Turbulence

SUMMARY

Additional analytical and experimental fluid mechanics studies were conducted to investigate instabilities in atmospheric flow systems associated with clear air turbulence.

The experimental portion of the program was conducted using the UARL Open Water Channel which allows investigation of flows having wide ranges of shear and density stratification. The program was primarily directed toward studies of the stability of straight, stratified shear flows with particular emphasis on the effects of velocity profile shape on stability, and on the interaction of shear flows with long-wavelength internal waves. The results of these studies were used to evaluate theoretical methods used in analyses of CAT encounters involving wave-induced shear-layer instabilities.

The results of these and past fluid mechanics investigations were then applied in an investigation of atmospheric shear flows. Aircraft and rawinsonde data were used in analyses of six cases in which clear air turbulence was associated with mountain lee waves. In addition, three cases were analyzed in which stratospheric clear air turbulence was encountered over thunderstorms. The results provide additional evidence that stable layers in the atmosphere can be destabilized by increases in shear which occur as the layers undergo long-wavelength, large-amplitude motions, as in flows through lee waves and flows forced up and over thunderstorms.

Recommendations were made for equipment and procedures that might be used in future flight research programs to obtain "in situ" measurements of the wave-induced instability phenomenon. Recommendations were also made for possible approaches, based on knowledge of this phenomenon, that might lead to improved CAT prediction along flight routes.

RESULTS AND CONCLUSIONS

1. The water channel experiments to investigate the stability of straight, stratified, shear flows having "S-shaped" velocity profiles confirmed that the shape of the velocity profile affects the dimensionless wavenumber, αd^* , of the instabilities which can occur. The values of αd observed in experiments with "S-shaped" profiles were significantly larger than those observed previously in experiments with hyperbolic tangent profiles. This result is in agreement with the theoretical stability criteria of Hazel for "S-shaped" profiles and Drazin for hyperbolic tangent profiles.

2. The experimental results and the theoretical stability criteria were also in agreement regarding the critical value of Richardson number. Both "S-shaped" and hyperbolic tangent profiles are stable for Richardson numbers greater than 0.25.

3. Although the values of dimensionless wavenumber, αd , at which instabilities occur at a Richardson number of 0.25 are larger for "S-shaped" profiles than for hyperbolic tangent profiles, the actual wavelengths, λ , are about the same (assuming that the shear layer thicknesses, the velocity differences across the shear layer, and the mean shears at the center of the shear layers are approximately equal). The theory indicates that the higher values of αd are due mainly to higher values of the parameter d necessary to describe "S-shaped" profiles. The experimental results tend to confirm this.

4. The preceding conclusion also applies to the wavelengths of instabilities that can be expected when stable shear layers in the atmosphere are destabilized by long-wavelength waves (i.e., wave-induced instabilities), such as mountain lee waves. If the shear-layer thickness, the velocity difference across the shear layer, and the mean shear at the center of the layer are fixed, then the wavelength of the instability occurring when the Richardson number decreases to 0.25 will be about the same, whether the profile is an "S" or a hyperbolic tangent. This wavelength is closely approximated by the wavelength given by Drazin's theory, $\lambda_E = (2\pi/\sqrt{2}) \cdot 2d$, where d is taken as half the shear-layer thickness.

*The characteristic breakdown flow pattern consists of waves which develop into vortices and turbulence. The wavenumber α is $2\pi/\lambda$, where λ is the wavelength of the instability, d is one of several parameters which describe the velocity profile (d is approximately half of the shear-layer thickness for hyperbolic tangent profiles, but this is not a good approximation for "S-shaped" profiles).

5. Water channel experiments were also conducted to investigate wave-induced instabilities in straight, stratified, shear flows. Theoretical predictions of the wave-induced shear were in good agreement with measured values. Moreover, the occurrence, or lack of occurrence, of instabilities in the shear layers was predicted quite well using the same method used for analyses of clear air turbulence encounters in the atmosphere.

6. The analyses of six cases in which CAT occurred in mountain lee waves provide further evidence that stable layers in the atmosphere can be destabilized by increases in shear which occur as the layers flow through the long-wavelength lee waves. Stable layers in the stratosphere were identified using rawinsonde data. The stability of these layers in the lee wave region was predicted by estimating the changes in shear that occurred near lee wave crests and troughs and applying the criterion $R_1 > 0.25$ for stability. Drazin's criterion was used to estimate the unstable wavelengths that might occur in these layers. In most cases, the estimated wavelengths were in fair to good agreement with wavelengths observed in the isentropes reconstructed from aircraft and rawinsonde data.

7. Similar analyses were made for three cases in which clear air turbulence was encountered over thunderstorms. In these cases, it was suspected that instabilities were induced as the flow was forced up and over thunderstorms. The results indicated that in at least one case it is probable that this phenomenon occurred. The estimated wavelengths were in fair to good agreement with those observed in the isentropes.

INTRODUCTION

The past decade has seen a very rapid growth in the number of commercial transports and general aviation aircraft that are designed for cruise flight in the lower levels of the stratosphere. The supersonic transport will cruise at even higher altitudes than those of today's transports. Because of the frequency with which clear air turbulence (CAT) is encountered in these regions, consideration of passenger safety and comfort has resulted in continued interest in the development of methods for the prediction and detection of CAT. CAT is also important because of its influence on the structure, stability and control, and operation of engines and inlets of the SST.

The principal objectives of the present program are (1) to gain increased understanding of the nature and causes of turbulent atmospheric phenomena, particularly clear air turbulence; (2) to develop improved criteria for predicting neutrally stable states in atmospheric flow systems, and (3) to compare the results of this research with available meteorological data and attempt correlations.

The results of fluid mechanics analyses and experiments conducted previously under this program are reported in Ref. 1. This previous work provided evidence that long-wavelength waves could destabilize initially stable shear layers which occur in the atmosphere. Since such long-wavelength waves may occur quite often in the atmosphere, the breakdown of these layers could account for an appreciable fraction of CAT which is encountered.

The study described in this report was an extension of the investigation reported in Ref. 1. The specific objectives were: (1) to conduct experiments to investigate further the effect of the shape of the velocity profile on the stability of straight, stratified shear flows; (2) to investigate experimentally the interaction of long-wavelength waves with stable shear layers; (3) to study further the possibility that long-wavelength waves can destabilize initially stable layers in the atmosphere; and (4) to make recommendations for approaches that might lead to improved prediction methods and for equipment and techniques that could be used for "in situ" measurements of CAT.

This report contains four main sections --- a discussion of the investigation of the stability of straight, stratified shear flows having "S-shaped" velocity profiles, a discussion of the investigation of the interaction of long-wavelength waves with straight, stratified, shear flows; a discussion of the application of the results obtained here and previous results to atmospheric shear flows; and a discussion of recommendations for "in situ" measurements and improved CAT prediction methods. Appendix I contains a description of equipment and procedures used in the fluid mechanics experiments. Appendix II contains the derivation of equations used to

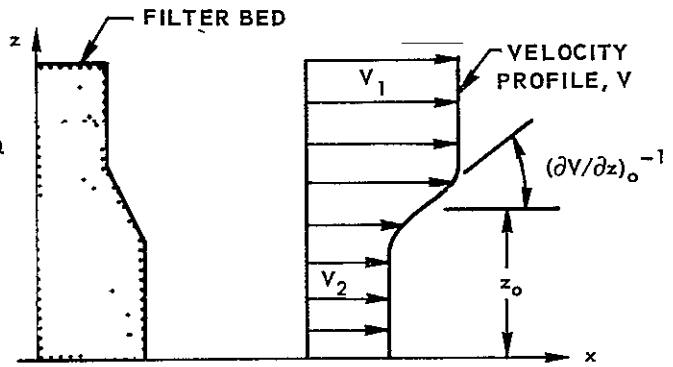
compare theoretical with experimental "S-shaped" velocity profiles. Appendix III contains the results of preliminary investigations of the effects of "three-dimensionality" --- i.e., cases where the transverse width of the shear layer is of the same order of magnitude as the wavelengths of the disturbances which occur --- on the stability of straight, stratified, shear flows.

STABILITY OF TWO-DIMENSIONAL, STRAIGHT, STRATIFIED
SHEAR FLOWS HAVING "S-SHAPED" VELOCITY PROFILES

The primary purpose of this part of the fluid mechanics program was to investigate the effects of the shape of the velocity profile on the stability of straight, stratified shear flows. First, experiments were conducted to obtain data on the stability of two-dimensional, straight, stratified shear flows having "S-shaped" velocity profiles, these data were also compared with theoretical stability criteria. The results for "S-shaped" flows were then compared with results from an earlier investigation of the stability of two-dimensional, straight, stratified shear flows having hyperbolic tangent velocity profiles. The end objective was to obtain results which could be applied to thin, initially stable shear flows occurring in the atmosphere. The program was directed toward three areas. (1) identifying the conditions under which such flows become unstable, (2) determining the characteristics of the flow during the initial phases of breakdown, and (3) evaluating existing theoretical stability criteria for subsequent use in studying atmospheric shear flows.

Review of Flows Having Hyperbolic Tangent Profiles

The stability of shear flows having hyperbolic tangent velocity profiles was investigated in detail in earlier work under this contract (Ref. 1). Flows having velocity profiles of this type were developed in the UARL Open Water Channel by shaping the foam material in the filter bed as shown in Sketch A (see Appendix I for a description of the water channel and the measurement techniques used). The stability of flows having such profiles was studied theoretically by Drazin (Ref. 2) and others. The hyperbolic tangent velocity profile which most closely approximates the profiles in the channel is given by



SKETCH A. FILTER BED AND VELOCITY PROFILE FOR HYPERBOLIC TANGENT VELOCITY PROFILE

$$v = v_0 + \frac{\Delta V}{2} \tanh \left(\frac{z - z_0}{d} \right) \quad (1)$$

In this equation, V is the local velocity at height z above the channel floor; $V_0 = (V_1 + V_2)/2$ is the velocity at the center of the shear layer at height z_0 , $\Delta V = (V_1 - V_2)$; and $d = (\Delta V)/2(\partial V/\partial z)_0$. The parameter d is a scale length and is approximately half the thickness of the shear layer. Drazin also used an exponential variation of density with height.

$$\rho/\rho_0 = e^{-\beta\left(\frac{z-z_0}{d}\right)} = e^{-\frac{Ri}{g} \frac{d}{d} \left(\frac{\partial V}{\partial z}\right)_0^2 \left(\frac{z-z_0}{d}\right)} \quad (2)$$

where Ri is the Richardson number and g is the gravitational constant. Since the change in density across the shear layer is small, a good approximation to Eq. (2) is

$$\rho/\rho_0 = 1 - \frac{Ri}{g} \frac{d}{d} \left(\frac{\partial V}{\partial z}\right)_0^2 \left(\frac{z-z_0}{d}\right) \quad (3)$$

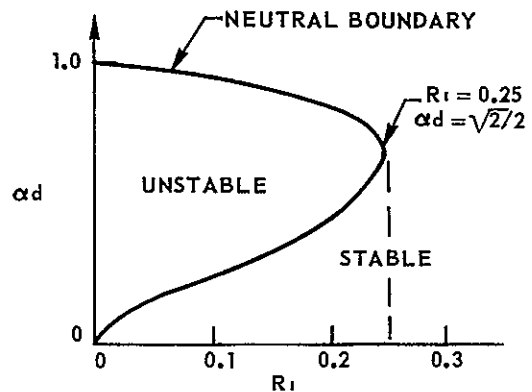
Drazin derives a criterion for stability in Ref. 2 by introducing a perturbation stream function

$$\psi' = \phi(z) e^{i\alpha(x-ct)} \quad (4)$$

into the equations governing the motion of the fluid. Here, α is the wavenumber, $\alpha = 2\pi/\lambda$, and c is the complex wave velocity, $c = c_r + i \cdot c_i$. The equations of motion then yield a single stability equation. Making use of the fact that the perturbations neither amplify nor decay when $c_i = 0$, Drazin solves for the following equation for neutral stability on the $\alpha d - Ri$ plane.

$$\alpha d = \sqrt{\frac{1}{2} \pm \sqrt{\frac{1}{4} - Ri}} \quad (5)$$

Sketch B shows this boundary which separates stable and unstable regions. The criterion indicates that the flow would be stable for disturbances of all dimensionless wavenumbers, αd , for $R_1 > 0.25$. For $R_1 < 0.25$, the flow would be unstable for dimensionless wavenumbers which lie inside the boundary.



SKETCH B. DRAZIN'S NEUTRAL STABILITY BOUNDARY FOR HYPERBOLIC TANGENT PROFILES

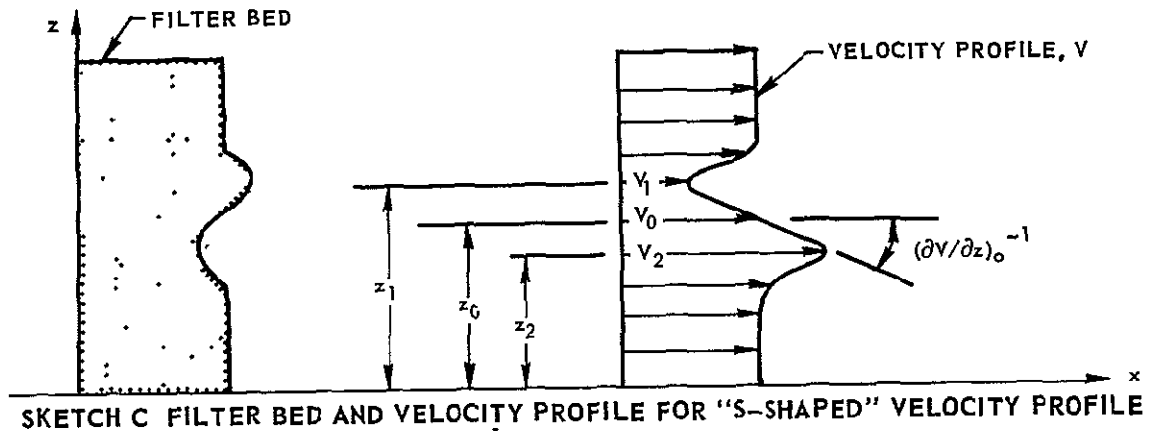
The results of water channel investigations of the stability of flows having hyperbolic tangent velocity profiles are summarized and compared with Drazin's theoretical criterion in Fig. 1. This plot shows the same data shown in Fig. 8 of Ref. 1. For each flow condition, the Richardson number was calculated using the slopes $(\partial V/\partial z)_0$ and $\partial T/\partial z$ from the measured profiles. The scale length, d , was calculated using the slope $(\partial V/\partial z)_0$ and the velocity difference ΔV from the velocity profile, ΔV was based on the maximum and minimum velocities in the vicinity of the edges of the shear layer. The wavenumber, $\alpha = 2\pi/\lambda$, of instabilities observed in the shear layer was calculated using wavelengths determined from photographs of dye traces. Thus, each flow condition at which waves were observed is identified by a point on the plot of αd vs R_1 .

The symbols in Fig. 1 denote different flow characteristics that were observed. The open circle symbol denotes conditions at which only waves were observed in the shear layer, that is, the waves extended the entire length of the channel without breaking down. The wavelengths of these waves ranged from about 3 to 6 in. The open circle symbols with flags indicate the nature of the disturbances observed --- for example, small-amplitude waves which persisted, waves which seemed to grow in amplitude to a certain point and then not grow further as they progressed downstream, and waves which appeared in the flow only intermittently. The half-solid symbols denote flow conditions in which the waves transitioned to vortices but did not transition to turbulence before reaching the downstream end of the channel. The full-solid symbols denote flow conditions at which the full sequence of events associated with complete shear-layer breakdown occurred --- waves, vortices, and turbulence. The crosses indicate conditions at which no waves of the type associated with instability occurred. At some conditions (indicated by (LW)), standing, long-wavelength (12 to 24 in.) waves occurred.

Examination of Fig. 1 indicates that most of the observations are in good agreement with Drazin's boundary. All cases in which full transition was observed fall in the unstable region. Six cases in which waves were observed fall in the stable region. The intermittent waves indicated at $Ri = 0.43$ and steady waves at $Ri = 0.38$ were unexpected, in subsequent tests at approximately the same conditions, no waves were observed. Four cases were observed which fall above the boundary but at $Ri < 0.25$. These four cases were, at the time of the tests, suspected to be attributable to differences between the experimental velocity profile and Drazin's hyperbolic tangent profile. This hypothesis was based on a theoretical study by Hazel (Ref. 3) which showed that instabilities associated with flows having "S-shaped" velocity profiles could have dimensionless wavenumbers greater than 1.0. This lack of agreement and proposed explanation, then, provided the motivation for the present experiments with "S-shaped" profiles.

Stability Criteria of Hazel for "S-Shaped" Velocity Profiles

"S-shaped" velocity profiles are developed in the UARL Open Water Channel by shaping the porous foam filter bed as shown in Sketch C.



The velocity profile used by Hazel in his theoretical study is

$$V = V_0 + \frac{\Delta V}{2} \operatorname{sech}^b \left(\frac{z - z_0}{d} \right) \tanh \left(\frac{z - z_0}{d} \right) \quad (6)$$

Here V is the local velocity at height z above the channel floor; $V_0 = (V_1 + V_2)/2$ is the velocity at the center of the shear layer at height z_0 ; b is an exponent that affects the shape of the "S", and $d = (\Delta V)/2(\partial V/\partial z)_0$. The parameter d is a scale length. The relationship of the velocity difference ΔV to $(V_1 - V_2)$ and b is (see derivation in Appendix II)

$$\Delta V = (b + 1) \frac{b+1}{2} \frac{1}{b} \frac{b}{2} (V_1 - V_2) \tag{7}$$

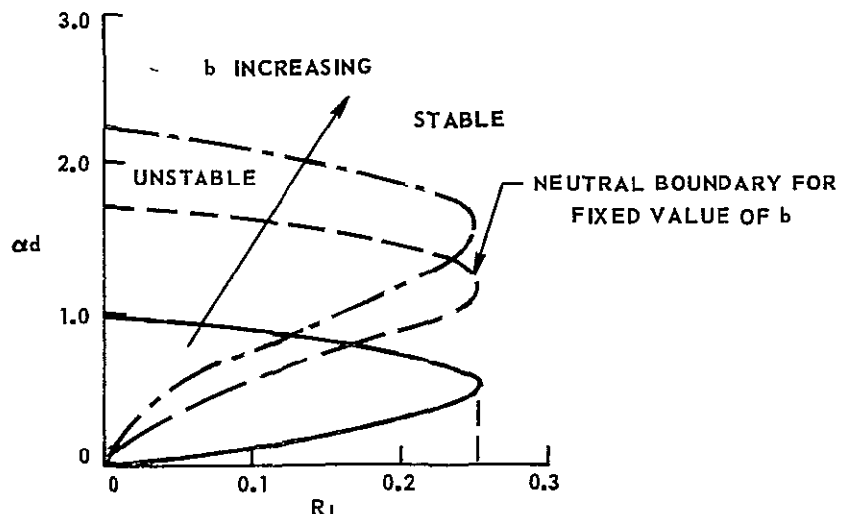
The theoretical density profile used by Hazel is

$$\rho = \rho_0 e^{-\frac{R_1 d (\partial V/\partial z)_0^2}{g} \tanh\left(\frac{z-z_0}{d}\right)} \tag{8}$$

Hazel derives criteria for stability in Ref. 3 for several velocity and density profiles. This is done by solving (using numerical techniques) a differential equation which is satisfied by one Fourier component of the velocity perturbation for a plane, two-dimensional, Boussinesq shear flow. The full perturbation velocity is given by

$$w(x,z,t) = \int_{-\infty}^{\infty} w(z) e^{i\alpha(x-ct)} d\alpha \tag{9}$$

Here, α is the wavenumber, $\alpha = 2\pi/\lambda$, and c is the complex wave velocity, $c = c_r + i \cdot c_i$. Using the fact that the perturbations neither amplify nor decay when $c_i = 0$, the locations of neutral stability curves were determined on the $\alpha d - R_1$ plane (see Sketch D). Like Drazin's criterion, these criteria indicate that the flow would be stable for disturbances of all dimensionless wavenumbers for $R_1 > 0.25$. For $R_1 < 0.25$, the



SKETCH D. HAZEL'S NEUTRAL STABILITY BOUNDARIES FOR "S-SHAPED" PROFILES

flow would be unstable for dimensionless wavenumbers which lie inside the boundaries. The locations of the neutral stability curves on the $\alpha d - Ri$ plane are dependent upon the value of the exponent b (see sketch).

Summary of Experiments with "S-Shaped" Velocity Profiles

The preceding theoretical considerations formed the basis for planning the experiments. The primary objective of the tests was to obtain data for "S-shaped" profiles so that the effects of the shape of the velocity profile on the stability of straight, stratified shear flows could be evaluated. Particular objectives were: (1) to determine if the initial disturbances in the shear layer have wave-like characteristics as in the case of flows having hyperbolic tangent velocity profiles and, if so, to obtain a method for estimating the wavelengths that occur, (2) to observe the stages of breakdown through which the initial disturbance transitions into turbulence, (3) to test the validity of Hazel's stability criteria, and (4) to provide further evidence that $Ri = 0.25$ should be used as the critical Richardson number in atmospheric analyses.

Characteristics of Breakdown of Flow

Figure 2 illustrates the stages observed as the flow in the shear layer breaks down. The breakdown characteristics were very similar to those for hyperbolic-tangent-type flows. There are four very distinct and repeatable stages which occur; dye traces illustrating the phenomenon are shown in the sketch in Fig. 2 and in the photographs. The photographs were taken through the lucite side wall (see Appendix I) with the flow from left to right. The scale appearing in the photographs was immersed in the flow close to the dye traces.

In Fig. 2(a), the flow appears undisturbed. Neither the dye traces nor the hydrogen bubble traces show visual evidence of any perturbation.

In Fig. 2(b), which is 28 in. further downstream, the center dye trace indicates the presence of a wave amplifying as it progresses downstream. The wave has a wavelength of about $\lambda = 5$ in. and an amplitude (half the distance from trough to crest) of about $a = 0.25$ in. at this point. By placing dye traces at several transverse locations across the channel, it was verified that the flow was approximately two-dimensional, i.e., the wave extended across the channel.

In Fig. 2(c), which is another 24 in. downstream, the waves have rolled up into vortices. The circulation of the vortices has the same sense as the vorticity introduced by the shear --- the shear is negative in this flow condition, and all of

the vortices rotated counterclockwise. These vortices grew slightly in size as they drifted downstream. Their downstream drift velocity was approximately V_0 , the velocity upstream at the center of the shear layer. The flow was also two-dimensional at this stage.

In Fig. 2(d), which is another 10 in. downstream --- 70 in. downstream of the filter bed --- the vortices have "burst" and the flow appears turbulent. The fluid motions were three-dimensional at this stage.

Velocity, Temperature, and Density Profiles

Velocity, temperature, and density profiles for three flow conditions are shown in Fig. 3. These data are for three different Richardson numbers and three different values of the exponent b used in Hazel's theoretical velocity profile $Ri = 0$ and $b = 0.8$ (Fig. 3(a)), $Ri = 0.014$ and $b = 0.3$ (Fig. 3(b)), and $Ri = 0.5$ and $b = 0.4$ (Fig. 3(c)). The velocity and temperature measurements were made within 2 to 10 in. downstream of the filter bed. The method for calculating the density profiles from the temperature profiles is given in Appendix I. The corresponding velocity and density profiles in Hazel's theory (Eqs. (6) and (8)) are shown by the dashed lines in Fig. 3.

These particular velocity profiles were selected because they illustrate typical differences which existed between velocity profiles in the water channel and the corresponding ideal "S" profiles of Hazel. Once a velocity profile had been measured, the value of the exponent b was derived so as to provide a reasonably good match between theoretical and experimental velocity profiles. The theoretical profile was chosen by matching to the data the following (see Appendix II and Sketch C): (1) the velocity difference, $V_1 - V_2$, (2) the vertical distance between V_1 and V_2 , $z_1 - z_2$, and (3) the mean velocity gradient, $(\partial V/\partial z)_0$, at z_0 . Agreement between the theoretical and experimental velocity profiles was best in the region of flow located between V_2 and V_1 .

The corresponding theoretical density profile was chosen by matching the density gradient and mean density of the experimental profile at the center of the shear region. Thus, the best agreement is obtained at the center of the shear layer. The theoretical and experimental profiles were most similar when the gradient was small.

Comparison of Experimental Results with Hazel's Theoretical Stability Criteria

Figure 4 is a summary of the results and a comparison with Hazel's theoretical criteria. The symbols in Fig. 4 denote different flow characteristics that were observed. The open circle symbols denote conditions at which small-amplitude waves were observed; that is, the waves extended the entire length of the channel or were

damped out before the end of the channel without making the transition to vortices. The wavelengths of these waves ranged from about $3/4$ to 6 in. The half-solid symbols denote conditions at which the waves transitioned to vortices but did not transition to turbulence before reaching the downstream end of the channel. Four or five waves were often observed upstream of the first discernible vortex. The full-solid symbols denote flow conditions at which the full sequence of events occurred --- waves, vortices, and turbulence. The crosses indicate conditions at which no waves of the type associated with instability occurred. At some conditions (indicated by (LW)), standing, long-wavelength (6 to 24 in.) waves occurred. These long-wavelength waves were investigated in some detail and are discussed later in this report. The values of the exponent b which provide the best match between the theoretical and experimental velocity profiles are given next to the symbols in Fig. 4.

Examination of Fig. 4 indicates that most of the experimental results are in agreement with Hazel's stability boundaries. For all cases in which instability was observed, the Richardson number was less than 0.25, and only one stable case was observed for which the Richardson number was less than 0.25 ($\alpha d = 0$, $R_1 = 0.2$). For all but one of the cases for which instability was observed, the dimensionless wavenumbers, αd , were greater than 1.2. This is in contrast to the results obtained for hyperbolic tangent velocity profiles (see Fig. 1) where the αd 's associated with instabilities were less than 1.2 for all but one case.

In matching theoretical to the experimental velocity profiles, it was found that, for most cases, values of b greater than 2 were required. Stability boundaries for $b > 1$ were not calculated by Hazel, the dashed boundary in Fig. 4 is an extrapolation of his results. Hazel's theory shows that as the value of b increases, the range of wavenumbers, αd , of instabilities which can occur also increases. The data appear to confirm this trend, although insufficient data were obtained to make detailed comparisons with Hazel's criteria for low values of b . Only two cases are not in agreement with Hazel's neutral stability boundaries. They are (1) $R_1 = 0$, $\alpha d = 2.4$, $b = 0.8$, and (2) $R_1 = 0$, $\alpha d = 2.07$, $b = 0.3$. However, these values of b are questionable since the agreement between the theoretical and experimental velocity and density profiles was comparatively poor for these cases.

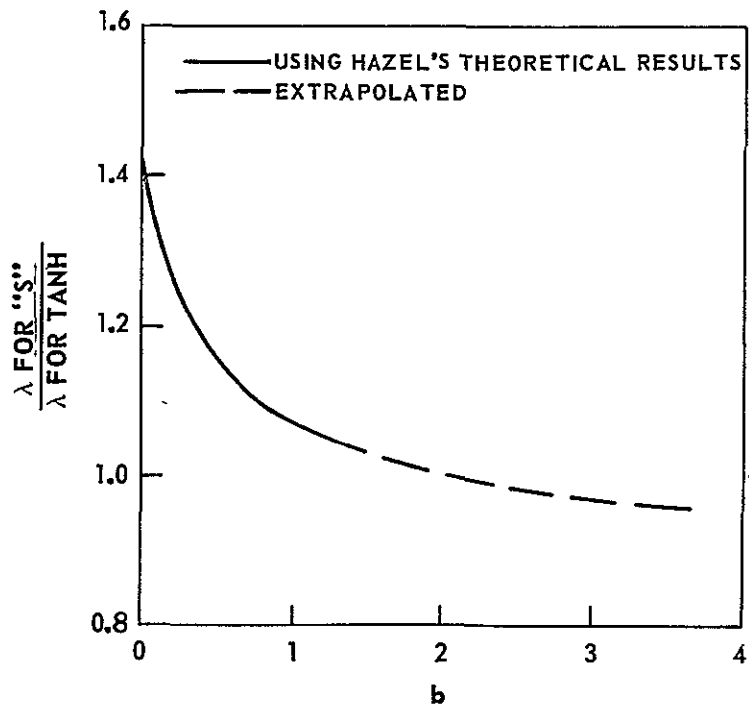
Concluding Remarks

The most important result of these experiments from the standpoint of the present program is that the data provide sufficient evidence to confirm the hypothesis that instabilities which occur in flows having "S" profiles generally have values of

αd considerably larger than those in flows having hyperbolic tangent profiles. As explained below, however, the actual wavelengths of instabilities at $Ri = 0.25$ are about the same due to compensating changes in d .

The theoretical criteria of Hazel differ from Drazin's criterion only in that one might expect to observe instabilities having larger dimensionless wavenumbers in unstable shear layers with "S" profiles. When b is greater than about 0.2, the value of dimensionless wavenumber at the critical Richardson number ($Ri = 0.25$) for Hazel's theory is greater than the corresponding values for Drazin's theory. Therefore, one might be inclined to expect shorter wavelengths for instabilities associated with "S" profiles than with hyperbolic tangent profiles. However, it can be shown that for an experimental velocity profile having a maximum velocity V_1 at z_1 , a minimum velocity V_2 at z_2 , and a velocity gradient $(\partial V/\partial z)_0$ at the center of the shear layer, the wavelength, λ , at $Ri = 0.25$ for the best fitting "S" profile is generally about the same as that for the tanh profile. This is because the value of d for the best fitting "S" profile is larger than that for the tanh profile. Thus, the increase in the critical value of αd is offset by an increase in d and, therefore, the wavelengths of instabilities in flows having "S" profiles are approximately the same as those for hyperbolic tangent profiles. This is illustrated in

Sketch E which shows, for instabilities associated with αd at $Ri = 0.25$, the theoretical variation of the ratio of λ for "S-shaped" profiles to λ for hyperbolic tangent profiles with the parameter b (b is related to $z_1 - z_2$, $V_1 - V_2$, and $(\partial V/\partial z)_0$ in Eq. (28) in Appendix II). For the range of b shown, and for b not near zero, this ratio is not greatly different from 1.0. Data from the water channel obtained near Richardson number of 0.25 tend to confirm this:



SKETCH E. THEORETICAL RATIO OF WAVELENGTHS FOR $Ri = 0.25$ FOR "S-SHAPED" AND HYPERBOLIC TANGENT PROFILES

<u>Profile</u>	<u>b</u>	<u>R₁</u>	<u>αd</u>	<u>d, in.</u>	<u>λ, in.</u>
"S-Shaped"	>2.0	0.17	1.8	1.5	5
"S-Shaped"	>2.0	0.16	1.9	1.6	5
Tanh	-	0.24	0.74	0.58	5
Tanh	-	0.16	0.84	0.52	4
Tanh	-	0.12	0.70	0.44	4

As a result, Drazin's value of $\lambda = (2\pi/\sqrt{2}) \cdot 2d$ (Fig. 1), where d is approximately equal to half the shear-layer thickness, would provide reasonably good estimates of the wavelengths that might occur in the atmosphere regardless of whether the profiles are "S" or tanh in shape.

The experiments and theories also provide further evidence that 0.25 should be used as the critical Richardson number, and that several distinct waves might be observed in the isentropes when instabilities occur in atmospheric shear layers.

INTERACTION OF LONG-WAVELENGTH WAVES WITH
TWO-DIMENSIONAL, STRAIGHT, STRATIFIED SHEAR FLOWS

The primary purpose of this part of the fluid mechanics program was to investigate, using the UARL Open Water Channel, the destabilization of initially stable shear flows by long-wavelength waves. Evidence that this phenomenon occurs in the atmosphere and may be the cause of an appreciable fraction of clear air turbulence that is encountered has been documented previously under this contract (Ref. 1). In Ref. 1, an analytical technique was developed to predict when long-wavelength waves, such as mountain lee waves, would destabilize initially stable shear layers in the atmosphere. In using the technique, $Ri = 0.25$ was used as the critical Richardson number for neutral stability. The increment in shear induced by the presence of long waves was estimated using an extension of a theory developed by Phillips (Ref. 4); properties of the atmosphere and the long-wavelength wave from rawinsondes and in-flight aircraft measurements were used as inputs to the calculation.

The objectives of the water channel experiments and analyses reported in this section were: (1) to investigate the conditions for wave-induced instability and the nature of the initial disturbances, (2) to obtain experimental verification of Phillip's theory for estimating the amplitude of long-wavelength waves and Haurwitz's theory (Ref. 5) for estimating their wavelengths, and (3) to study the validity of Phillips' theory for estimating shear induced by long-wavelength waves. Finally, it was desired to relate the results to atmospheric flows so that they could aid in analyses of CAT encounters.

Theoretical Criteria of Phillips and Haurwitz

In Ref. 4, Phillips derives an equation for the increment in shear induced by the presence of a wave traveling along the thermocline in a fluid. He introduces a perturbation velocity into the equations governing the motion of the flow and solves for the vertical velocity gradient. For the case studied, the mean shear was zero; the density changed abruptly across the thin thermocline (stable layer) and was uniform above and below the layer. The expression he obtained for the wave-induced shear is

$$\Delta(\partial v / \partial z) = (N_M^2 - n^2) \cdot \left(\frac{a}{V_0} \right) \quad (10)$$

where

$$N_M = \text{Brunt-Vaisälä Frequency} = \sqrt{-\frac{g}{\rho} \left(\frac{\partial \rho}{\partial z} \right)}$$

$$n = \text{Wave Frequency} = 2\pi V_0 / \lambda_{LW}$$

$$a = \text{Wave amplitude}$$

$$V_0 = \text{Wave velocity}$$

The Brunt-Vaisala frequency can be obtained from measured temperature profiles. For stationary waves, the wave velocity, V_0 , is equal to the mean velocity through the wave and can be determined from measured velocity profiles (temperature and velocity profiles are available for the atmosphere from radiosonde and rawinsonde data). For the case that the wavelength of the internal wave is large compared to the thickness of the thermocline, Phillips shows that $N_M \gg n$ (this condition generally applies to long-wavelength waves, such as mountain lee waves, in the atmosphere), and the wave amplitude is

$$a = \frac{2V_0}{N_M} \quad (11)$$

For conditions where $N_M \gg n$, the wave-induced shear becomes

$$\Delta(\partial V / \partial z) = 2N_M \quad (12)$$

For cases when N_M is not much greater than n (this was the case for the long-wavelength waves which were observed in the UARL Open Water Channel), Eq. (10) can be used to calculate the wave-induced shear provided that, in addition to N_M , the amplitude, wavelength, and mean velocity of the long-wavelength wave are known.

In Ref. 5, Haurwitz derives an expression for the wavelength of waves traveling on a discontinuity of density and velocity at a velocity equal to the mean flow velocity and in a direction opposite to the flow direction (thus the wave is stationary relative to the observer). The velocity and density gradients were considered to be zero on either side of the discontinuity. The expression obtained by Haurwitz is

$$\lambda_{LW} = \frac{2\pi}{g} \frac{\rho_2 V_2^2}{(\rho_2 - \rho_1)} \left(\left(\frac{V_1}{V_2} \right)^2 \frac{\rho_1}{\rho_2} + 1 \right) \quad (13)$$

where V_1 and ρ_1 are the velocity and density, respectively, of the light fluid which flows over the heavy fluid having a velocity and density V_2 and ρ_2 , respectively.

Using estimated values of wave-induced shear, it is possible to predict the effects of long-wavelength waves on local Richardson number in shear flows in water (this was done for atmospheric flows in Ref. 1). A schematic diagram of the flow condition is shown in Fig. 5(a). At the left are shown upstream velocity and temperature profiles with a stable shear layer having a thickness $2d$. Within this layer, the mean velocity is V_0 and the mean temperature is T_0 , the mean shear is $(\partial V/\partial z)_0$ (all mean values are at the center of the shear layer).

At the right in Fig. 5(a) is shown a portion of a long-wavelength wave having an amplitude (which might be 0.1 to 1.0 in.) and a wavelength λ_{LW} (which might be 6 to 30 in.). It is assumed in this analysis that the thickness of the shear layer, the mean temperature, and temperature gradient remain constant as the flow within the shear layer experiences the undulating motion.

The minimum local Richardson number in the flow is calculated with the wave-induced shear, $\Delta(\partial V/\partial z)$, added to the initial mean shear. An expression for the minimum Richardson number (which occurs locally at the crest in the example given, but would occur at a trough if the initial shear were negative) is

$$Ri_{MIN} = \frac{N_M^2}{(|(\partial V/\partial z)_0| + |\Delta(\partial V/\partial z)|)^2} \quad (14)$$

Using Phillips' expression for the wave-induced shear, this equation can be rewritten as

$$Ri_{MIN} = \frac{N_M^2}{(|(\partial V/\partial z)_0| + (N_M^2 - n^2)(a/V_0))^2} \quad (15)$$

From Eq. (15) it can be seen that small values of Ri_{MIN} are associated with large initial shears, $(\partial V/\partial z)_0$; with large wave amplitudes, a ; with small flow velocities, V_0 ; and with large wavelengths, λ_{LW} ($n = 2\pi V_0/\lambda_{LW}$). The effect of the

temperature gradient, $\partial T/\partial z$, on Ri_{MIN} cannot be seen directly from Eq. (15) but can be seen from the plot in Fig. 5(b). This figure is based on values of V_o (0.1 ft/sec), T_o (60 F), a (0.05 ft) and λ_{LW} (2.0 ft) which have been observed in the UARL Open Water Channel in one flow condition. Curves are shown for three values of initial shear $|(\partial V/\partial z)_o|$ (0.5, 1.0, and 2.0 sec^{-1}). The curves show that with increasing initial temperature gradient, Ri_{MIN} first increases to a maximum value, and then decreases. The minimum Richardson number is zero when $\partial T/\partial z = 0$ and ∞ , although the latter condition cannot be seen in Fig. 5(b). Since the flow is unstable for $Ri < 0.25$, weakly stabilized layers ($\partial T/\partial z$ near zero) as well as very strongly stabilized shear layers ($\partial T/\partial z$ large) could be destabilized in the presence of a long-wavelength wave. Temperature gradients greater than 300 deg F/ft could not be obtained in the water channel; hence, the effects of long-wavelength waves on strongly stabilized layers could not be studied. In the atmosphere, the strongly stabilized layers are most interesting since it is believed that breakdown of such layers causes the most severe turbulence. This will be discussed in a later section.

The dashed curves in Fig. 5(b) were obtained by assuming that $\lambda_{LW} = \infty$, so that $N_M^2 \rightarrow n^2$. This reduces Eq. (10) to

$$\Delta(\partial V/\partial z) = N_M^2 \left(\frac{a}{V_o} \right) \quad (16)$$

The solid curves in Fig. 5(b) were obtained by using the equation for finite wavelength waves, Eq. (10). A comparison of the dashed and solid curves shows (1) that for the flow and wave conditions of Fig. 5(b), use of the simple expression for wave shear, Eq. (16), in the calculation of Ri_{MIN} does not cause large errors in Ri_{MIN} , and (2) that these small errors in Ri_{MIN} which do occur decrease with increasing value of initial shear and are least for very small and very large initial temperature gradients.

Not entirely evident in Fig. 5(b) is the fact that for small values of initial shear, $|(\partial V/\partial z)_o|$, wave-induced instability is limited to quite a narrow range of initial temperature gradients. For instance, for $|(\partial V/\partial z)_o| = 0.5 \text{ sec}^{-1}$, the flow would be unstable for $\partial T/\partial z < 23 \text{ deg F/ft}$ even if the wave were not present and would be stable for $\partial T/\partial z > 30 \text{ deg F/ft}$ in the presence of the wave. For $|(\partial V/\partial z)_o| = 1.0 \text{ sec}^{-1}$, the range of $\partial T/\partial z$ for wave-induced instability is 94 to 140 deg F/ft. Assuming that 300 deg F/ft is the maximum temperature gradient which can be attained in the channel, the greatest range of $\partial T/\partial z$ for wave-induced instability is 180 to 300 deg F/ft for an initial velocity gradient $|(\partial V/\partial z)_o| = 1.39 \text{ sec}^{-1}$.

It would appear then that it should be relatively easy to develop the conditions necessary for wave-induced shear instabilities using the UARL Open Water Channel. The preceding initial velocity and temperature gradients and mean velocity are well within the channel capability, and long-wavelength waves having wavelengths and amplitudes on the order of 2 ft and 0.05 ft, respectively, have been observed many times. However, the parameters are all interdependent such that it is very difficult to obtain simultaneously all of the conditions under which instability would be wave-induced. In fact, only three cases occurred in which instability was suspected to be wave-induced and in these cases the instability that was observed was a slight undulation or wave superimposed on the stationary long-wavelength wave. This will be discussed in more detail in the next section.

Summary of Experimental Results

Objectives of Tests

Particular objectives of the tests discussed here were (1) to induce shear instability in the flow by long-wavelength waves, (2) investigate the effects of the long-wavelength waves on the local shear and Richardson number and to compare the measured wave-induced shears with wave shears predicted using Phillip's theory, and (3) to compare measured wave properties, such as amplitude and wavelength, with values predicted using the theories of Phillips and Haurwitz, respectively.

Example of Effect of Long-Wavelength Wave on Local Richardson Number

A long-wavelength wave typical of those studied in the UARL Open Water Channel is shown in Fig. 6 ($\lambda_{LW} = 15.5$ in. and $a = 0.8$ in.). The mean velocity measured at the center of the shear layer was $V_o = 0.04$ ft/sec and was almost constant through the wave crests and troughs shown in Figs. 6(a) through 6(d). Based on an average of the local flow conditions (measured at the center of the shear layer) at the crest at $x = 12$ in. and at the trough at $x = 19.5$ in., the initial shear, $(\partial V/\partial z)_o$ was 0.26 sec^{-1} , the initial Richardson number, R_{1o} , was 2.5, and the wave-induced shear, $\Delta(\partial V/\partial z)$, was 0.16 sec^{-1} . The data in Figs. 6(a) through 6(d) show that the shear, $\partial V/\partial z$, was greater at the crests than at the troughs. The data also show that the shear decreases with increasing downstream distance, a trend which was observed repeatedly in the long-wavelength wave experiments. The minimum Richardson number, R_{1MIN} , which was observed at the crest at $x = 12$ in., was 40 percent of the initial Richardson number ($R_1 = 1.0$, compared with $R_{1o} = 2.5$) based on the mean shear $(\partial V/\partial z)_o = 0.26 \text{ sec}^{-1}$. The Richardson number which was observed at the trough at $x = 19.5$ in., $R_1 = 14$, was over 500 percent of the initial Richardson number.

Typical Velocity, Temperature, and Density Profiles at Long-Wavelength Wave Crests and Troughs

Velocity, temperature, and density profiles obtained at crests and troughs of the wave shown in Fig. 6 are presented in Fig. 7.

The influence of the long-wavelength wave on the shape of the velocity profile is shown in Fig. 7(a). The velocity profile (solid line) at the first crest ($x = 12$ in.) is compared to the best fitting theoretical "S" profile (dashed line) for $b = 2$. This indicates that the profile is initially somewhat "S-shaped."

The influence of the long-wavelength wave on the temperature profile is shown in Fig. 7(b). It can be seen (most obvious at first crest and trough) that the thermocline, as would be expected, is slightly higher at the crests than at the troughs. These data also indicate that the temperature gradient changes in the fluid as it flows through the wave, however, these changes are relatively small compared to the changes in velocity gradient.

The density gradients in Fig. 7(c) were obtained from the temperature gradients in Fig. 7(b). Like the temperature profile, the density profile is not uniform and consists of two regions above and below the thermocline where the density is relatively constant. The changes in temperature gradient which occurred in the fluid as it flowed through the wave were reflected in the density gradient, however, as in the case of the temperature gradient, the changes were small relative to the changes in the velocity gradient.

Comparison of Measured with Predicted Amplitudes and Wavelengths of Long-Wavelength Waves

Measured values of long-wavelength wave amplitude are compared with values predicted using Phillips' theory (Ref. 4) in Fig. 8(a). The measured wave amplitudes, a_m , were determined from the displacement of streamlines which were photographed using a neutrally buoyant fluorescent dye (described in Ref. 1). The predicted values of amplitude, a_p , were obtained using Eq. (11), measured values of mean velocity, V_0 , and Brunt-Vaisala frequencies, N_M , calculated from measured temperature profiles. The data in Fig. 8(a) indicate that the measured amplitudes, a_m , were approximately one-third of the predicted amplitudes, a_p . This discrepancy might be explained in part by the fact that one of the conditions assumed in deriving Eq. (11), that $N_M/n \gg 1$, is not satisfied in the experiments. The numbers next to the data points in Fig. 8(a) denote corresponding values of $\eta = N_M/n$. The data indicate that in the water channel tests the condition $N_M/n \gg 1.0$ is far from being satisfied. In the atmosphere, except for very weakly stabilized layers, N_M is much greater than n and, therefore, Eq. (11) should more accurately predict the amplitude of long-wavelength waves.

Measured wavelengths of long-wavelength waves are compared with values predicted using Haurwitz's theory (Ref. 5) in Fig. 8(b). The measured wavelengths, $(\lambda_{LW})_m$, were determined by measuring the distance between crests and troughs of the long-wavelength waves from photographs of the dye traces. The predicted wavelengths, $(\lambda_{LW})_p$, were calculated using Eq. (13) with densities and velocities from measured temperature and velocity profiles, respectively. The data in Fig. 8(b) indicate fair agreement between measured and predicted wavelengths. The differences between measured and predicted values increase with increasing wavelength. Part of the reason for this can be seen by examining Eq. (13) (also shown in Fig. 8(b)). One way to increase wavelength, λ_{LW} , is to decrease the density difference, $\rho_2 - \rho_1$. However, this tends to make the predicted wavelengths more sensitive to errors in ρ_1 or ρ_2 . This may explain some of the differences in Fig. 8(b) since in this series of experiments it was easier to obtain changes in λ_{LW} by changing density gradient than velocity gradient. However, this still does not account for the general trend in which the measured wavelengths are generally less than predicted values. Subsequently, the method of Haurwitz (Ref. 5) was examined to determine the possible effect of having a finite depth in the water channel on the measured wavelengths. The influence on wavelength of having a free surface above the shear layer and a boundary below the shear layer (it was applied by Phillips (Ref. 4) to flows in oceans) was calculated. This method predicted a trend that did not account for the discrepancy in the data. That is, it predicted that wavelength should increase with decreasing depth while the wavelengths measured in the water channel were generally less than those predicted for infinite-depth flows.

Comparison Between Measured and Predicted Wave Shear in Long-Wavelength Waves

Measured values of wave-induced shear caused by long-wavelength waves are compared with values using Phillips' theory (Ref. 4) in Fig. 9. The measured wave shear, $|\Delta(\partial V/\partial z)|$, was determined by taking one-half the difference between the shears at the crest and trough of the long-wavelength wave. The predicted wave shears were calculated using Eq. (10) with measured values of wave amplitude, wavelength, and velocity. The Brunt-Vaisala frequency, N_M , was determined from measured temperature profiles. The results shown in Fig. 9 indicate that in most cases the agreement between measured and predicted values of wave shear was good. The results of these tests provide some experimental evidence that Eq. (10), which was used in Ref. 1 to predict wave-induced shear $\Delta(\partial V/\partial z)$ in the atmosphere, correctly predicts wave shear induced by long-wavelength waves.

Wave-Induced Shear Instability

Figure 10 is a plot of initial shear, $|\partial V/\partial z|_0$, versus the Brunt-Vaisala frequency, N_M . The boundaries define regions where wave-induced instability can occur. They were calculated using Eq. (15) with the condition $N_M \gg n$. The boundaries are loci of $Ri_{MIN} = 0.25$ for constant values of a/V_0 .

To the left of the boundary for $a/V_0 = 0$, the presence of a long-wavelength wave is not required for the flow to be unstable, and any instabilities observed in this region would not be wave-induced. In the region to the right of the boundary for $a/V_0 = 0$, the boundaries define the lower limit of a/V_0 required for wave-induced instability to occur. For example, a long-wavelength wave having $a/V_0 > 0.75$ would cause wave-induced instability to occur anywhere in the region between the boundary for $a/V_0 = 0$ and $a/V_0 = 0.75$; a long-wavelength wave having $a/V_0 < 0.5$ would not cause wave-induced instability anywhere in the region to the right of the boundary for $a/V_0 = 0.5$.

The open and solid symbols in Fig. 10 denote cases for which long-wavelength waves were and were not observed, respectively. For each flow condition for which a long-wavelength wave was present (the open symbols) (1) the Brunt-Vaisala frequency was determined from an average of the crest and trough temperature gradients (in these tests, measurements were made at the most upstream crest and trough for which measurements could be made), and (2) the absolute value of initial shear $|(\partial V/\partial z)_0|$ was determined from an average of the shears measured at the crest and trough. For cases in which long-wavelength waves were not observed (the solid symbols), the Brunt-Vaisala frequency and the absolute value of initial shear were obtained from the temperature gradient and velocity gradient, respectively, at the center of the shear layer (measurements were made at approximately the same distance downstream from the filter as the measurements that were made when waves were present). The numbers near the symbols denote values of a/V_0 . The letters near the symbols denote the type of instability that was observed --- W - wave, V - Vortex, T - Turbulence.

The solid symbols show that long-wavelength waves were not observed in the channel for values of Brunt-Vaisala frequency, N_M , less than about 0.3 sec^{-1} . Therefore, it was not possible to investigate wave-induced instability for values of N_M less than about 0.3 sec^{-1} .

Examination of Fig. 10 indicates that most of the observations are in agreement with the stability boundaries. Instability of some type was observed for all cases which are to the left of the boundary for $a/V_0 = 0$. This is expected since the flow is predicted to be unstable in this region even without the additional shear from a long-wavelength wave. Instability was observed for only three of the cases (marked with asterisks) which are to the right of the locus $a/V_0 = 0$. In these cases long-wavelength waves were present. The instability appeared as short-wavelength undulations on the long-wavelength waves and was suspected to be wave induced. Based on measured values of a/V_0 for the three cases for which wave-induced instability was suspected and the values of a/V_0 for the cases where wave-induced instability was not observed, the data agree with the stability boundaries. The value of Ri_{MIN} for the three cases involving instability was less than 0.25. For cases where instability was not observed, Ri_{MIN} was greater than 0.25. More cases in which wave-induced

instability occurred were not studied during these experiments because of the difficulty in establishing the required conditions in the channel. This was because of the fact that the required combinations of parameters, such as long-wavelength wave amplitude, wavelength, and flow density and velocity gradients, were difficult to obtain simultaneously because of their interdependence.

Concluding Remarks

These laboratory experiments tend to confirm the analytical methods that have been used to estimate wave-induced shear and to predict the onset of shear-layer instabilities in analyses of CAT encounters in the atmosphere. The most important results are shown in Figs. 9 and 10.

Figure 9 shows that the wave shear $|\Delta(\partial V/\partial z)|$ --- the change in shear that occurs when a thin shear layer flows through a long-wavelength wave --- can be reasonably well predicted using Eq. (10). The inputs needed for this calculation are the long-wave amplitude (a), the mean flow velocity (V_0), the Brunt-Väisälä frequency (N_M), and the long-wave frequency (n).

Figure 10 shows that the occurrence, or lack of occurrence, of wave-induced shear-layer instabilities in the water channel experiments could be predicted fairly consistently using Eq. (15). This equation incorporates Eq. (10) for estimating the wave shear. The criterion for instability that was used is that the shear layer will become unstable when the predicted minimum Richardson number is less than 0.25.

APPLICATION TO ATMOSPHERIC SHEAR FLOWS

In earlier work under the present contract, initial studies were conducted in which clear air turbulence was associated with the breakdown of shear layers in the atmosphere. Several cases were presented in Ref. 1 in which mountain waves were the cause of wave-induced instabilities in initially stable shear layers. As discussed in Ref. 1, these findings appear to be in agreement with evidence assembled by other investigators --- notably Woods (Ref. 6, a study of wave-induced instabilities in the ocean), Ludlam (Ref. 7, a study of billow cloud formation), Mitchell and Prophet (Ref. 8, an analysis of USAF Project HICAT flight data), Spillane (Ref. 9, an analysis of high-altitude CAT over the Australian desert region), and Hardy (Ref. 10, radar measurements that indicated wave-like motions in regions of CAT).

The purpose of the meteorological analyses of CAT encounters that are presented in this section of the report was to further test the hypothesis of wave-induced shear-layer instabilities in the atmosphere. Most of the cases studied involved mountain waves as the cause of the instability. Several cases of CAT caused by the wave-like flow over the top of thunderstorms were also analyzed.

Data for these analyses were obtained from Project HICAT reports (Ref. 11) and from the 1970 Lee Wave Observational Program. The author participated in the data acquisition phase of the 1970 Lee Wave Program at the National Center for Atmospheric Research in Boulder, Colorado for a three-week period during February 1970. While at NCAR, he worked under the direction of Dr. Douglas K. Lilly who kindly made all of the preliminary rawinsonde and aircraft in-flight data available for these analyses.

Review of the Fundamental Flow Phenomenon

A schematic diagram of the flow condition considered here is shown in Fig. 11(a). At the left are shown upstream wind and temperature profiles with a stable shear layer having a thickness $2d$. Within this layer, the mean wind is V_0 and the mean temperature is T_0 ; the shear is $(\partial V/\partial z)_0$ and the environmental lapse rate is $\partial T/\partial z$.

At the right in Fig. 11(a) is shown a portion of a long-wavelength wave having an amplitude a (which might be 2000 or 3000 ft), and a wavelength λ_{LW} (which might be 10 or 20 nm). It is assumed in this analysis that the thickness of the shear layer, the mean temperature and the lapse rate all remain constant as the flow within the shear layer experiences the undulating motion ($2d$, T_0 , and $\partial T/\partial z$ are constant). From Phillips (Ref. 4), the following equation for the increase in shear that occurs at the crest (see Fig. 11(a)) can be derived:

$$\Delta(\partial V/\partial z) = (N_M^2 - n^2) \left(\frac{a}{V_0} \right) \quad (17)$$

For flows in the atmosphere instead of the ocean,

$$\begin{aligned} N_M &= \text{Brunt-Vaisala frequency} = \sqrt{(g/T_0) \cdot [(\partial T/\partial z) - (\partial T/\partial z)_{ad}]} \\ n &= \text{wave frequency} = 2\pi V_0/\lambda_{LW} \\ (\partial T/\partial z)_{ad} &= \text{adiabatic lapse rate, } -2.98 \times 10^{-3} \text{ deg C/ft*} \end{aligned}$$

This increase in shear is added to the initial shear. An expression for the minimum Richardson number (which occurs locally at the crest in the example given, but would occur at the trough if the initial shear were negative) is

$$R_{1\text{MIN}} = \frac{N_M^2}{(|(\partial V/\partial z)_0| + |\Delta(\partial V/\partial z)|)^2} \quad (18)$$

Since $N_M^2 \gg n^2$ under all conditions of interest (this is only untrue for weakly stable lapse rates, i.e., when $\partial T/\partial z \approx (\partial T/\partial z)_{ad}$), the expression can be further simplified to

$$R_{1\text{MIN}} \approx \frac{N_M^2}{(|(\partial V/\partial z)_0| + N_M^2(a/V_0))^2} \quad (19)$$

From Eq. (19) it is evident that low values of $R_{1\text{MIN}}$ are associated with large initial shears, $(\partial V/\partial z)_0$, with large long-wave amplitudes, a , and with low winds, V_0 . The latter two parameters are not independent, however, since large amplitude waves do not usually occur under low-wind conditions. If very stable layers having low winds, V_0 , are only slightly disturbed by large amplitude waves generated in nearby stable layers having high winds, it is possible for the very stable layers to become unstable ($R_{1\text{MIN}} = 0.25$) even with zero initial shear, $(\partial V/\partial z)_0$. For instance, a stable layer having a lapse rate $\partial T/\partial z = 3 \times 10^{-3}$ deg C/ft, a temperature $T_0 = -60$ deg C, a wind velocity $V_0 = 15$ kts, and zero initial shear would be destabilized by a wave having an amplitude $a = 660$ ft. Although turbulence produced in such a layer might

*Note use of minus sign to denote temperature decreasing with increasing altitude.

not be severe because of the low wind velocity, aircraft flying through such regions could encounter sudden changes in ambient temperature which may affect engine operation.

The effect of the environmental lapse rate, $\partial T/\partial z$, on $R_{1\text{MIN}}$ is not evident from Eq. (19) but can be seen in Fig. 11(b). This figure is based on typical conditions under which long-wavelength waves such as mountain lee waves are observed in the lower stratosphere (see, for example, details of the lee-wave cases that are described later in this section of the report). Curves are shown for three shears --- small shears (1 and 2 kts/1000 ft) and a moderately large shear (12 kts/1000 ft). The curves show that the greater the initial stability from a convective standpoint (i.e., the greater $\partial T/\partial z$), the lower $R_{1\text{MIN}}$ will be. They also show that shear layers which have small values of initial shear are stable when the environmental lapse rate is near zero. Thus, it is primarily the most stable layers appearing in the temperature profile that are of interest. The curves also show that as the environmental lapse rate approaches the adiabatic lapse rate (-3 deg C/ft), all shear layers become unstable.

The stratosphere is the primary region in which wave-induced instabilities are important. In general, the environmental lapse rate is quite close to the adiabatic lapse rate below the tropopause and, therefore, layers having large shears do not occur in this region of the atmosphere without an accompanying increase in stability of the layer. Consequently, below the tropopause one should expect to see a correspondence between the temperature and velocity profile in regions where large shears occur. Above the tropopause the environmental lapse rate is appreciably greater than the adiabatic lapse rate and layers having large shears are stable (for instance, in the absence of long-wavelength waves, a shear of 25 kt/1000 ft is stable in air having a lapse rate $\partial T/\partial z = 0$ deg C/ft). Therefore, in regions above the tropopause it is not necessary that there be a correspondence between the temperature and velocity profiles.

Wavelengths of Instabilities that Might Occur

In Fig. 12, the ranges of unstable wavelengths (λ in mm) are shown as functions of the shear-layer thickness ($2d$ in ft) for local values of R_1 between 0.25 and 0. These ranges are based on Drazin's criterion for hyperbolic tangent velocity profiles. Considering first $R_1 = 0.25$ (Fig. 12(a)), only one wavelength is unstable at each value of $2d$ --- $\lambda = (2\pi/\sqrt{2}) \cdot 2d$. This is the wavelength corresponding to $\alpha d = \sqrt{2}/2$, the only point at which Drazin's boundary reaches as far out as $R_1 = 0.25$ (Fig 1). For smaller values of R_1 --- Figs. 12(b), (c), and (d) --- there are increasingly wider ranges of unstable wavelengths.

One can argue several different ways to reach the conclusion that, when an instability occurs, the wavelength will be given by the unique value of αd associated with $R_1 = 0.25$. This wavelength is often said to be "the most likely" or "the most unstable" wavelength based on its theoretical growth rate. However, another viewpoint is that if the Richardson number at the crest of the long-wavelength wave is less than 0.25, then the flow in the shear layer must have experienced $R_1 = 0.25$ on the way up to the crest. Since instability would occur at $R_1 = 0.25$, the wavelength that would be seen would therefore correspond to the αd for $R_1 = 0.25$ ($\lambda = (2\pi/\sqrt{2}) \cdot 2d$ in Drazin's theory).

It was pointed out previously that, for shear layers having roughly equivalent minimum and maximum velocities and mean shears, the wavelengths of instabilities at $R_1 = 0.25$ would be about the same for "S-shaped" as for hyperbolic tangent velocity profiles (even though the wavenumbers, αd , are different). Thus, the wavelength from Drazin's theory, $\lambda = (2\pi/\sqrt{2}) \cdot 2d$, should provide a reasonable estimate of the unstable wavelengths that can be expected. The analyses of the California and Colorado Lee Wave cases in Ref. 1 showed that wavelengths determined by this method were in reasonably good agreement with those observed in the atmosphere.

Analyses of CAT Associated with Mountain Lee Waves

Project HICAT

The objective of the HICAT program was to determine the statistical characteristics of high-altitude (45,000 to 70,000 ft) CAT so as to improve aircraft structural design criteria. In addition, meteorological forecasts and analyses were correlated with the CAT measurements to improve CAT forecast procedures. Results obtained during the program following March 1967 are presented in Ref. 11. In a number of tests in this phase of the program, high-altitude CAT was encountered and recorded in flights from various bases around the world. Analyses of some of these cases were made in the study reported herein to obtain further evidence that initially stable shear layers in the stratosphere can be destabilized as they flow through the undulations of long-wavelength waves which are caused by mountains. Results of the cases are presented in this section. Details of the cases are summarized in Table I.

Test 264, Run 16

Severe to moderate turbulence was encountered during flights at altitudes from 61,000 to 61,500 ft near Grand Junction, Colorado in this flight. The reconstructed

480 K isentrope* for this test is shown in Fig. 13. This isentrope was selected for analysis because its altitude was approximately the same as the flight altitude and the altitude of stable layers which were likely to be destabilized by the lee wave. In this case, the winds were from west to east (left to right in Fig. 13). Short-wavelength waves indicative of shear-layer instabilities and long-wavelength waves are apparent in the isentrope (the characteristics of these waves are summarized in Table I).

Wind and temperature profiles for this case are shown in Fig. 14. Wind and temperature profiles from Yucca Flats rawinsonde data are shown in Fig. 14(a). The wind profile from aircraft flight data, obtained near Grand Junction, is shown by the dashed line in the wind-profile plot. Profiles from Denver rawinsonde data are shown in Fig. 14(b). Rawinsonde data from Grand Junction, which would be the most appropriate for this case, were not available.

Two very stable layers are evident in the Yucca Flats temperature profile at altitudes near the 61,000-ft flight level. Layer 1 is approximately 680 ft thick; the Richardson number was calculated to be $Ri_0 = 77$ based on Yucca Flats wind and temperature data and $Ri_0 = 0.34$ based on the aircraft wind data and Yucca Flats temperature data (differences between rawinsonde and flight data are not usually this large). The expected wavelength from an instability in this layer is $\lambda_E(1) = (2\pi/\sqrt{2})680 = 3020$ ft, or 0.5 nmi. Based on the Yucca Flats wind profile, the shear is negative which would suggest that if an instability were to occur it would be near a trough of a lee wave instead of near a crest. Based on the aircraft wind profile, the shear is positive, suggesting that the location of the instability should be near a crest. Layer 2 is 1050 ft thick and the corresponding wavelength is $\lambda_E(2) = 0.8$ nmi. The Richardson number for this layer is $Ri_0 = 9.7$. The shear is negative so that instability would be expected near a trough of a lee wave.

A stable layer can be seen in the Denver temperature profile at an altitude of 60,000 ft. The layer is 870 ft thick and the corresponding wavelength is $\lambda_E(3) = 0.6$ nmi. The Richardson number for this layer, based on Denver wind and temperature profiles, is $Ri_0 = \infty$; based on aircraft wind data and Denver temperature profile, $Ri_0 = 8.4$. For this layer the shear was zero based on the Denver wind profile and a combination of positive and negative segments based on the aircraft wind data. Therefore, the instability could be expected in either the crest or the trough of the lee wave. These and other characteristics of the expected waves that will be discussed subsequently are summarized under "Test 264, Run 16" in Table I.

*From the rawinsonde data, the profile of potential temperature was determined. Aircraft measurements of temperature along the flight path were converted to potential temperature. It was assumed that the potential temperature profile was unchanged by the wave. Then, the height of any specific isentrope relative to the aircraft was determined from the profile and the potential temperature at the aircraft. Actual aircraft altitude was then used to locate the isentrope relative to sea level.

Since all of the previous values of Ri_o are greater than 0.25, additional wave-induced shear is required to destabilize the flow. If it is assumed that the rawinsonde data are representative of undisturbed conditions upstream or downstream of the mountain wave, then the minimum Richardson number of a given layer that would be expected to occur in the crest or trough of a wave is given in Eq. (19). This assumes that the shear determined from the wind profile, $(\partial V/\partial z)_o$, is changed by an amount $\Delta(\partial V/\partial z)$ determined from Eq. (17) using the observed long-wavelength characteristics from Fig. 13 and the characteristics of the individual layers from Fig. 14. Thus, for these calculations the following were used with the appropriate dimensional units:

<u>Layer</u>	<u>λ_{LW}, nm</u>	<u>a, ft</u>	<u>T_o, deg C</u>	<u>$\partial T/\partial z$, deg C/1000 ft</u>	<u>Source of Wind Data</u>	<u>V_o, kts</u>	<u>$(\partial V/\partial z)_o$, kts/1000 ft</u>
1	8-10	1000	-60.5	1.9	Rawinsonde	12	1.8
2	8-10	1000	-57.0	6.8	Rawinsonde	34	7.3
3	8-10	1000	-60.5	7.1	Rawinsonde	18	0
1	8-10	1000	-60.5	1.9	Flight	16	28
3	8-10	1000	-60.5	7.1	Flight	12	8

The results of these calculations are shown in Table I under " Ri_{MIN} --- based on $\Delta(\partial V/\partial z)$." It will be noted that the wave shear decreased the Richardson number appreciably. In layer 1, based on rawinsonde wind data, Ri decreased from 77 to 0.47; based on winds from flight data, Ri decreased from 0.34 to 0.11. In layer 2, Ri decreased from 9.7 to 1. In layer 3, based on rawinsonde wind data, Ri decreased from ∞ to 0.61; based on winds from aircraft data, Ri decreased from 8.4 to 0.38. Strict application of the criterion $Ri_{MIN} = 0.25$ for instability leads one to conclude that, based on rawinsonde wind data, instability would not occur and, hence, small waves would be unlikely. However, the calculated values for two of the layers (layers 1 and 3) are not much larger than the critical value. An increase in the amplitude of the lee wave --- about 50 percent --- above that estimated from Fig. 13 would result in $Ri = 0.25$, in which case waves would be expected. Calculations of Ri based on winds obtained from aircraft data indicate that layer 1 would be unstable and waves would be expected to occur.

To obtain the minimum value of Ri_{MIN} that can reasonably be derived from a given set of temperature and velocity profiles, $2\Delta(\partial V/\partial z)$ can be used in Eq. (19) instead of $\Delta(\partial V/\partial z)$. The reason for this is that, at least in theory, the difference in shear between a crest and a trough is $2\Delta(\partial V/\partial z)$. In the unlikely circumstance that the rawinsonde was not taken upstream in undisturbed air but instead passed upward through a trough (in the case of positive $(\partial V/\partial z)_o$), then the change in shear

would be $2\Delta(\partial V/\partial z)$. It is fairly certain that the rawinsondes in some of these cases were not in undisturbed air, although there is no evidence that they were taken precisely through troughs or crests.

The values of $R_{1,MIN}$ based on $2\Delta(\partial V/\partial z)$ are also shown in Table I. For layers 1 and 3, the values of $R_{1,MIN}$ were less than 0.25 (based on wind profiles from either rawinsonde or aircraft flight data). Thus, under the specified conditions, both layers 1 and 3 would be classified as unstable, and short wavelength waves would be expected.

The principal results of this analysis can be seen upon examination of Table I and Fig. 13. The calculations indicate that at least one wavelength should appear ($\lambda_E(1) = 0.5$ nmi) and that a second might appear ($\lambda_E(3) = 0.6$ nmi). The isentropes in Fig. 13 show several sets of small waves having wavelengths, λ_O , of about 0.2 to 2.0, 0.1 to 0.2, 0.2 to 1.0, and 0.2 to 0.7 nmi.* Some of these wavelengths are quite close to the expected values. It was not possible to determine, from the isentropes in Fig. 13, the location of the instabilities with respect to crests or troughs of the lee wave. The locations of moderate to severe turbulence were approximately the same as those of the short-wavelength waves which were observed.

Test 267, Runs 8, 9, and 28

In this case, in which mountain waves were suspected to be involved, severe to moderate turbulence was encountered during flights at altitudes of approximately 51,000 and 55,500 ft near Albuquerque, New Mexico. The reconstructed 404 K isentropes for Runs 8 and 9 are shown in Figs. 15(a) and (b), respectively. The reconstructed 422.5 K isentrope for Run 28 is shown in Fig. 15(c).

The 404 K and 422.5 K isentropes were selected for analysis because of their proximity to stable layers at altitudes corresponding to the flight altitudes. Short-wavelength waves indicative of instability in the layers are apparent in the isentropes; however, the long-wavelength mountain waves could not be identified in the isentropes due to the short time span of the available data.

*The wavelength, λ_O , was determined from measurement along the flight path of the wavelength of short waves which were observed in the isentropes and the angle between flight path and the wind direction. It was assumed that the axis of these waves was perpendicular to the direction of the wind. The observed wavelength, λ_O , was equal to the wavelength measured along the flight path multiplied by the cosine of the angle between the direction of flight path and wind.

Wind and temperature profiles for these runs are shown in Fig. 16. The wind profile shown in Fig. 16(a) was obtained from aircraft flight data, and the temperature profile shown in Fig. 16(b) was obtained from rawinsonde data from Albuquerque. Stable layers are evident in the temperature profile. The 404 K isentrope passes through the lower stable layer (layer 1) which is near the 50,500 ft flight level. The 422.5 K isentrope passes through the upper combined layer (layers 2 and 3) which is near the 55,500 ft flight level. The thickness of layer 1 was 750 ft and the expected wavelength for instability of this layer is $\lambda_{E(1)} = 0.6$ nmi. The thicknesses of layers 2 and 3 were 900 ft and 150 ft, respectively, so that the expected wavelengths for instability of these layers would be $\lambda_{E(2)} = 0.7$ nmi and $\lambda_{E(3)} = 0.1$ nmi, respectively. Layers 2 and 3 might also be treated as a combined layer with an expected wavelength $\lambda_{E(2-3)} = 0.8$ nmi.

For this case the amplitude and wavelength of the lee waves (if present) could not be determined from the isentropes. As a result, neither the destabilizing effect of lee waves nor the location of the short-wavelength waves relative to crests or troughs could be estimated.

The results from this case can be seen in Table I and Fig. 15. Calculations of the initial Richardson number, Ri_0 , for layer 1 showed that the large shear shown in the wind profile would be enough to cause instability in this layer ($Ri_0 = 0.18$). Short-wavelength waves are apparent in the 404 K isentrope of Figs. 15(a) and (b) (λ_0 is equal to the measured wavelength multiplied by the cosine of the angle between the aircraft heading and wind direction), layer 1 was unstable. The observed wavelengths $\lambda_0 = 0.3$ to 0.6 nmi are in good agreement with the expected wavelength, $\lambda_{E(1)} = 0.6$ nmi. Calculations of the initial Richardson numbers for stable layers 2 and 3 (based on an extrapolated value of wind shear) indicated that these layers would be stable in the absence of a long-wavelength wave. Short-wavelength waves are apparent in the 422.5 K isentrope (shown in Fig. 15(c)), indicating that instabilities are present in layers 2 or 3, or in the combined layer 2 and 3. The observed wavelengths, $\lambda_0 = 0.8$ to 1.5 nmi, are in good agreement with the expected wavelengths for layer 2 and combined layer 2 and 3.

Test 282, Run 2

In Test 282, Run 2, turbulence was encountered in flights made between Denver and Grand Junction, Colorado. Flights were made at several levels. Very little turbulence was reported at 52,000 ft; light to moderate was reported east of Denver at 57,000 ft, moderate to severe was reported at 62,000 ft (Run 2), and light turbulence was reported at 64,000 ft. The reconstructed 440 K isentrope is shown in Fig. 17. This isentrope was selected because it was at approximately the same altitude as a stable layer near the flight altitude. Both long and short-wavelength waves are apparent in the isentrope

Wind and temperature profiles obtained from Granby, Colorado rawinsonde data for this case are shown in Figs. 18(a) and (b), respectively. Several stable layers are evident in the temperature profiles. The two layers of most interest are layers 1 and 2 which were located at mean altitudes of 58,300 and 53,125 ft, respectively. Layer 1 was closest to the flight level of Run 2. If these layers were destabilized by a lee wave, the expected wavelength for both layers would be $\lambda_{E(1)} = \lambda_{E(2)} = 1.5$ nm. The shear is negative for both layers, so that the instability would be expected near the trough of a long-wavelength wave.

The principal results of the analysis of this case can be seen in Fig. 17 and Table I. The stability of layers 1 and 2 were investigated using the characteristics of the individual layers (Fig. 18), the characteristics of the long-wavelength wave determined from the isentrope (Fig. 17) and the analysis discussed previously. The calculations showed that for layers 1 and 2, respectively, (1) initial Richardson numbers were $Ri_0 = 5.7$ and 17.3 , (2) minimum Richardson numbers --- based on $\Delta(\partial V/\partial z)$ --- were $Ri_{MIN} = 0.78$ and 1.51 and (3) minimum Richardson numbers --- based on $2\Delta(\partial V/\partial z)$ --- were $Ri_{MIN} = 0.29$ and 1.05 . Strict application of the criterion $Ri_{MIN} < 0.25$ for instability leads one to conclude that an instability would not occur and, hence, small waves would be unlikely. However, based on $2\Delta(\partial V/\partial z)$, Ri_{MIN} for layer 1 is only slightly greater than critical. An increase in the lee wave amplitude to approximately 2000 ft or an increase in initial shear by approximately 200 percent would make the Ri_{MIN} , based on $\Delta(\partial V/\partial z)$, less than 0.25 for layer 1. Aircraft flight data obtained at altitudes slightly above that of stable layer 1 indicated that wind shears were present which were approximately six times greater than those shown in the Granby wind profile. The wavelengths of the small waves which were observed in the isentrope shown in Fig. 17, $\lambda_0 = 0.2$ to 1.0 nm, are in fair agreement with the expected wavelength $\lambda_{E(1)} = 1.5$ nm. The observed location of the waves in the trough of the lee wave is as expected since the shear in the Granby wind profile is negative. The short-wavelength waves were apparent in the isentrope for the same portion of the flight path over which the moderate to severe turbulence was encountered.

Before leaving this case it should be mentioned that the "sawtooth" shape of the Granby temperature profile is similar to those which can result from horizontal motion of the radiosonde through crests and troughs of lee waves during its vertical ascent (e.g., see Ref. 8). Assuming a balloon ascent rate of 500 ft/min (Ref. 12) and using the differences in altitude between minimum temperatures in the temperature profile, the time it takes the balloon to travel between crests is calculated to be approximately 12 minutes. Assuming that the balloon travels horizontally at velocity of 40 kts (approximately equal to the wind velocity), the wavelength of the lee wave is calculated (the product of the balloon velocity and time between crests) to be approximately $\lambda_{LW} = 8$ nm. This agrees with the $\lambda_{LW} \approx 8$ to 10 nm observed in the

isentropes in Fig. 17. Although there is no other evidence that the radiosonde in fact passed through a wave (the Granby launch site is at $x = 55$ nmi in Fig. 17), this particular temperature profile (Fig. 18(b)) is open to question.

1970 Colorado Lee Wave Observational Program

The 1970 Colorado Lee Wave Observational Program was a cooperative meteorological field experiment involving participants from universities, Government agencies, and private organizations. The program was first initiated in 1965 when efforts were made to investigate lee waves in the region of the Front Range of the Rocky Mountains near Boulder, Colorado. In February 1968, a more complete measurement network (including research-instrumented aircraft) was established and a second observational period was undertaken (the analysis of a case which involved CAT and lee waves from this program was reported in Ref. 1). A third observational program was undertaken in 1970. Two of the primary scientific objectives of the 1970 program, which was directed by Dr. D. K. Lilly of NCAR, were (1) to measure the detailed statistical properties of lee flows that contribute to changes in the large-scale atmospheric structure and (2) to determine conditions under which CAT is generated by instabilities associated with standing lee waves. Preliminary data were analyzed for three of the cases which were obtained during the February portion of the 1970 program. The results of analyses of these cases are presented in this section.

Four aircraft participated in the flights for these three cases. The four participating aircraft and the approximate ranges of flight altitudes flown are: (1) Air Force RB-57F - 45,000 to 63,000 ft, (2) ESSA B-57A - 35,000 to 45,000 ft; (3) NCAR Sabreliner - 25,000 to 35,000 ft; and (4) NCAR Buffalo - 15,000 to 25,000 ft. The ESSA B-57A flight data were not yet available at the time of this writing. Isentropes were calculated for flights only where appreciable lee wave and turbulence activity were reported.

Case of February 13, 1970

The isentropes for this case are shown in Fig. 19. The wind was from the west (left to right in Fig. 19) and parallel to the direction of the flights. The flights were flown over the Kremmling and Denver vortices between Kremmling and a point approximately 45 nmi east of Denver. Long-wavelength waves are evident in all of the isentropes, however, the wave patterns appear to be quite irregular. The lee waves in the isentropes have wavelengths which range from approximately 10 to 20 nmi and amplitudes (half the height from crest to trough) up to about 1000 ft. Two rawinsondes were used in this analysis. One was launched at Grand Junction (Figs. 20(a) and (b)) which is upstream and approximately 125 nmi west-southwest from Kremmling. The second was launched at Denver (Figs. 20(c) and (d)) which is downstream approximately 80 nmi east-southeast from Kremmling. A rawinsonde launched at Kremmling during this case failed.

Two and four stable layers were identified in the Grand Junction and Denver profiles, respectively (see Fig. 20). The wavelengths that would be expected to occur are shown in Figs. 20(b) and (d). Layers which were subsequently found to be stable when $2\Delta(\partial V/\partial z)$ was used in computing $R_{1\text{MIN}}$ are denoted by an asterisk.

The characteristics of the expected and observed waves are summarized in Table I under "Colorado Case - Feb. 13, 1970." The layers have been grouped according to their altitudes. The first two layers (layers 1 and 3) have mean altitudes of 60,150 and 61,250 ft ($\theta = 448$ and 458 K) and are associated with the upper 435 and 450 K isentropes in Fig. 19. The next two layers (layers 4 and 5) have mean altitudes of 55,700 and 48,750 ft ($\theta = 422$ and 386 K) and are associated with middle 392 and 405 K isentropes in Fig. 19. The last two layers (layers 2 and 6) have mean altitudes of 36,825 and 35,575 ft ($\theta = 333$ and 330 K) and are associated with the lower 330 K isentrope in Fig. 19.

The principal results of this analysis can be seen upon examination of Table I and Fig. 19. Consider the upper group of isentropes first. The calculations indicate that of all of the stable layers, layers 1 and 3 are the least stable; however, based on $R_{1\text{MIN}} < 0.25$ for instability, these layers should remain stable. Small waves having wavelengths $\lambda_0 = 2$ to 4 nm were observed in the isentropes associated with the upper stable layers. The observed wavelengths were in good agreement with expected wavelengths $\lambda_{E(1)} = 3.8$ and $\lambda_{E(2)} = 3.0$. A wave amplitude of approximately 2500 ft (approximately 2.5 times the observed amplitude), would be required to destabilize the upper layers. This is a little more than one-half of the total change in altitude of the 435 K isentrope. The location of moderate turbulence which was encountered at 59,000 ft corresponded to the location of the small waves that were observed.

The small waves in the isentropes appear to start in the troughs of the lee waves and to extend downstream through crests and troughs. As indicated in Table I, the initial shear based on the wind profile upwind of the mountains at Grand Junction was negative so that small waves would be expected in the troughs. Based on positive shear in the Denver profile, small waves would be expected at the crests.

It is also interesting to examine the middle and lower isentropes in Fig. 19 in view of the predictions for stable layers (layers 2, 4, 5, and 6) associated with these isentropes. All four layers were predicted to remain stable even based on $R_{1\text{MIN}}$ computed using $2\Delta(\partial V/\partial z)$. No small waves were observed in the isentropes in this region (Fig. 19). However, the occurrence of moderate turbulence was reported by the pilot of the AF RB-57F at approximately 50,000 ft and 37 nm east of Denver.

Case of February 17, 1970

The isentropes are shown in Fig. 21. The wind was from west to east (left to right in Fig. 21) and parallel to the direction of the flights. The flight path was the same as for the previous case (Kremmling to Denver). Long-wavelength waves are evident in all of the isentropes and there appears to be some pattern to the wave structure. The lee waves in the isentropes had wavelengths up to approximately $\lambda_{LW} = 30$ nm and amplitudes up to approximately $a = 1800$ ft. It can be seen in Fig. 21 that two of the isentropes at low altitudes overlap (see for instance the 311.1 and 314.2 K isentropes). This situation was noted infrequently in previous cases (see, for example, Fig. 15 of Ref. 1). This overlap could be the result of changes in the wave pattern between flights over a given point or from errors in temperature measurements (when the environmental lapse rate is near the adiabatic lapse rate small errors in measured temperature can result in large altitude errors when plotting the isentropes).

Rawinsonde data from Grand Junction (Figs. 22(a) and (b)), Kremmling (Figs. 22(c) and (d)), and Denver (Figs. 22(e) and (f)) were used in the analysis of this case. However, the data for the upper level winds from the Kremmling rawinsonde were missing. A total of twelve stable layers were identified in the temperature profiles and were investigated. Two were from the Grand Junction temperature profile, two from the Kremmling profile, and eight from the Denver profile. The wavelengths that would be expected to occur are shown in Figs. 22(b), (d), and (f). Layers which were subsequently found to be stable when $2\Delta(\partial V/\partial z)$ was used in computing R_{1MIN} are denoted by an asterisk.

The characteristics of the expected and observed waves are summarized in Table I under "Colorado Case - February 17, 1970." The layers have been grouped according to their altitudes. The first group (layers 1, 5, and 6) had mean altitudes between 62,175 and 66,775 ft ($\theta = 449$ to 496 K) and are associated with the uppermost 450 K isentrope in Fig. 22. The second group (layers 7, 8, and 9) had mean altitudes between 60,125 and 61,525 ft ($\theta = 424$ to 445 K) and are associated with the 390, 410, and 450 K isentropes. The third group (layers 2, 3, 4, 10, 11, and 12) had mean altitudes between 26,050 and 51,625 ft ($\theta = 322$ to 373 K) and are associated with the lower 322.1 and 368 K isentropes.

The principal results of this analysis can be seen upon examination of Table I and Fig. 21. First, consider the upper group of isentropes ($\theta = 390$ to 450 K and $h = 53,000$ to 61,000 ft). Examination of Table I shows that the layers having mean altitudes between 62,175 and 66,775 (layers 1, 5, and 6) were predicted to remain stable ($R_{1MIN} > 0.25$ --- based on $2\Delta(\partial V/\partial z)$). In Fig. 21 it can be seen that there are no short waves in the 450 K isentrope at approximately 61,000 ft although light turbulence was encountered. The flight at 64,000 ft was reported to be smooth --- no turbulence. The next layers (layers 7, 8, and 9) have mean altitudes between

60,125 and 61,525 ft. The calculations indicate that, for these layers, at least two wavelengths should occur ($\lambda_E(7) = 0.6$ nm and $\lambda_E(9) = 2.3$ nm) and one might occur ($\lambda_E(8) = 0.3$ nm --- this layer requires only an increase in $\Delta(\partial V/\partial z)$ of 6 percent for $Ri_{MIN} < 0.25$). The 410 and 390 K isentropes in Fig. 21 which were obtained from flights at 53,000 and 57,000 ft have small waves with wavelengths $\lambda_o = 1.0$ to 2.5 nm which are in fair agreement with the expected wavelengths. The small waves in the isentropes appear in the troughs of the long-wavelength waves. As indicated in Table I, the shear was negative for the two layers for which instability should occur and, therefore, the small waves would be expected in the troughs.

Stability ($Ri_{MIN} < 0.25$ --- based on $2\Delta(\partial V/\partial z)$) was predicted for the layers (layers 2, 3, 4, 10, 11, and 12) having mean altitudes between 26,050 and 51,625 ft. The stability predictions for layers 4 and 12 (mean altitudes 26,050 and 33,700) were based on lee-wave amplitudes estimated from the isentropes above and below this level. In Fig. 21 it can be seen that there are no small waves in the isentropes associated with these layers; however, the occurrence of very light to light turbulence was reported throughout the altitude range associated with these isentropes (such turbulence might be caused as slightly stable layers having small shears are destabilized by the lee waves --- see Fig. 11). Between the altitudes of 27,000 and 36,000 ft the pilot of the NCAR Sabreliner reported lee wave activity, but no turbulence.

Case of February 18, 1970

The isentropes are shown in Fig. 23. The wind was from west to east (left to right in Fig. 23) and parallel to the direction of the flights. The flights were on a line between the Kremmling and Akron vortices and from Kremmling to a point on the line approximately 125 nm east of Kremmling. This point was approximately 50 nm east-northeast of Denver.

A pattern of lee waves can be seen in the isentropes of Fig. 23. The waves had wavelengths from $\lambda_{LW} = 6$ to 20 nm and amplitudes up to $a = 1350$ ft. Rawinsonde data from Grand Junction (Figs. 24(a) and (b)), Kremmling (Figs. 24(c) and (d) --- upper level data missing) and Denver (Figs. 24(e) and (f)) were used in the analysis of this case. However, in this case the 1200 GMT (approximately 2 hours before the first flight) rawinsonde data for Grand Junction and Denver were incomplete (upper level data missing) and, therefore, the 2400 GMT (approximately 10 hours after the first flight) rawinsondes had to be used. A total of 31 stable layers which were identified in the temperature profiles from the three rawinsondes were investigated; eleven from the Grand Junction temperature profile, eight from the Kremmling profile, and twelve from the Denver profile. The wavelengths that would be expected if the

flow becomes destabilized are shown in Figs 24(b), (d), and (f). Layers which were subsequently found to be stable when $2\Delta(\partial V/\partial z)$ was used in computing Ri_{MIN} are denoted by an asterisk.

The characteristics of the expected and observed waves are summarized in Table I under "Colorado Case - February 18, 1970." The layers have been grouped according to their altitudes. The first group (layers 1, 2, 3, 4, 20, 21, and 22) had mean altitudes between 65,075 and 81,360. The second group (layers 5, 6, 7, 12, 23, 24, 25, 26, and 27) had mean altitudes between 32,325 and 63,895 ft and are associated with the 352 and 470 K isentropes. The third group (layers 8, 9, 10, 14, 15, 28, 29, and 30) had mean altitudes between 25,875 and 28,445 ft and are associated with the 324 and 333 K isentropes. The fourth group (layers 13, 16, and 17) had mean altitudes between 24,125 and 25,200 ft and are associated with the 310 K isentrope. The fifth group (layers 11, 18, 19, and 31) have mean altitudes between 19,550 and 23,255 ft and are associated with the 302 K isentrope.

The principal results of this analysis can be seen upon examination of Table I and Fig. 23. The results shown in Table I for the uppermost group of stable layers (layers 1, 2, 3, 4, 20, 21, and 22) were included to show that such layers can be present at altitudes as high as 80,000 ft and may be destabilized by lee waves having relatively small amplitudes ($a = 1000$ ft was used here, based on the waves apparent in the 470 K isentrope).

Table I shows that the layers in the second group (layers 5, 6, 7, 12, 23, 24, 25, 26, and 27; $\theta = 346$ to 440 K) are expected to be stable. In Fig. 23 it can be seen that there are no small waves in the 352 and 470 K isentropes. However, isentropes were not plotted in the altitude region between these two isentropes and it is not known whether or not small waves were present in this region. Inspection of data recorded on the RB-57F indicated that wave activity was small for this region except at 63,500 ft for which the 470 K isentrope is shown. Light turbulence was detected at 49,000, 57,000, 61,000, and 63,500 ft; moderate turbulence was detected at 61,000 ft.

Table I shows that the layers in the third group (layers 8, 9, 10, 14, 15, 28, 29, and 30; $\theta = 317$ to 328 K) are predicted to remain stable (even for Ri_{MIN} based on $2\Delta(\partial V/\partial z)$) These layers are associated with the 324 and 333 K isentropes. In Fig. 23 it can be seen that there are no small waves in the 333 K isentrope, however, small waves --- $\lambda_0 = 1.5$ to 2.5 mm --- can be seen in the 324 K isentrope. The expected wavelengths for these layers were $\lambda_E = 0.2$ to 1.8 mm. Turbulence was not reported for the flights associated with these isentropes.

Table I shows that the layers in the fourth group (layers 13, 16, and 17; $\theta = 309$ to 316 K) are also predicted to remain stable (even for Ri_{MIN} based on $2\Delta(\partial V/\partial z)$). These layers are associated with the 310 K isentrope. In Fig. 23 it can be seen that there are no small waves in this isentrope, although light turbulence was reported at three locations along the flight path.

Next consider the last group ($\theta = 293$ to 303 K) of layers (layers 11, 18, 19, and 31) which are associated with the 302 K isentrope. Calculations show that at least two wavelengths should occur $\lambda_E(11) = 0.5$ nm and $\lambda_E(31) = 0.6$ nm. The 302 K isentrope in Fig. 23 indicates the presence of small waves with wavelengths, $\lambda_0 = 0.5$ to 2.5 nm which are in fair agreement with the expected wavelengths. The small waves apparent in the isentrope just to the east of Kremmling appear to be just downstream of a crest in the lee wave. This is the expected location for small waves associated with both layers 11 and 31. The small waves which occur further to the east appear downstream of a large crest throughout a region of the isentrope which appears to be free of lee-wave activity.

Analyses of CAT Over Thunderstorms

It is suspected that the mechanism of wave-induced shear-layer instability is not restricted to mountain waves but can occur anywhere in the atmosphere where long-wavelength waves occur. To investigate the possibility that the blocking effect of thunderstorms could cause such waves, three Project HICAT cases in which turbulence was encountered in clear air over thunderstorms were analyzed using techniques described previously.

Project HICAT

Test 198, Runs 9, 12, and 13

In Test 198, long-wavelength waves were suspected to be caused as flow in the stratosphere was forced up and over a line of thunderstorms near Oklahoma City. Severe to moderate turbulence was encountered during flights over the storms at approximately 51,000 ft. The reconstructed 410 K isentrope is shown for Runs 9, 12, and 15 in Fig. 25. This isentrope was selected because of its proximity to stable layers having mean altitudes near 51,000 ft. Short-wavelength waves indicative of instability in the layers are apparent in the isentropes. However, the characteristics of any long-wavelength waves which might have been present could not be determined from these isentropes (the component of flight path distance perpendicular to the assumed wave axis direction was only about 4 nm). The locations of the thunderstorms are shown in Fig. 25. This information was determined from data supplied by Mr. P. Boone of the U. S. Air Force Flight Dynamics Laboratory at Dayton, Ohio.

Wind and temperature profiles are shown in Fig. 26. The wind profile shown in Fig. 26(a) was obtained from flight data and the temperature profile shown in Fig. 26(b) was obtained from Amarillo rawinsonde data. The rawinsonde data from Oklahoma City (nearest to the area covered by the flights) were missing. Two stable layers can be seen in the temperature profile; the corresponding expected wavelengths are $\lambda_E(1) = \lambda_E(2) = 1.0$ nmi. The expected wavelength based on the combined layers is $\lambda_E(3) = 2.0$ nmi.

For this case, the amplitude of the long-wavelength waves could not be deduced from the isentropes. Hence, the usual analysis to determine the stability of these layers and to locate the small waves relative to long-wave crests or troughs could not be made.

The results which were obtained can be seen in Table I and Fig. 25. The wavelengths of the short-wavelength waves ($\lambda_0 = 0.4$ to 1.6) which are apparent in the isentropes are about the same as the expected wavelengths (1.0 to 2.0 nmi). The waves were apparent for most of the flight paths for the three runs. The moderate and severe turbulence occurred in patches. There appeared to be correlation of the location of the turbulence with the location of the thunderstorms.

Test 202, Run 8

In Test 202 moderate to severe turbulence was encountered during a flight at approximately 58,000 ft over thunderstorms located about 70 nmi north of Little Rock, Arkansas. It was suspected that long-wavelength waves were produced as the flow in the stratosphere was forced up and over the thunderstorms and that these waves destabilized stable layers near the flight level. The isentrope is shown in Fig. 27. Wind was from west to east (left to right in Fig. 27) and approximately 22 deg to the direction of the flights. Long-wavelength waves are evident in the isentrope and appear to have wavelengths and amplitudes up to 16 nmi and 1300 ft, respectively.

The wind profile was obtained from flight data and is shown in Fig. 27(a). The temperature profile was obtained from rawinsonde data from Oklahoma City which was up-wind of the thunderstorms.

Two stable layers were identified in the temperature profile at mean altitudes of 61,100 and 57,250 ft. The wavelengths that were expected to occur were $\lambda_E(1) = 1.3$ nmi and $\lambda_E(2) = 1.5$ nmi. Examination of Table I shows that both layers would be expected to be unstable for $R_{1,MIN}$ based on $\Delta(\partial V/\partial z)$. Most of the short-wavelength waves which are apparent in the isentrope in Fig. 27(c) had wavelengths between 0.4 and 2.0 nmi, with one as long as 4 nmi. These are in fair agreement with the expected wavelengths $\lambda_E(1) = 1.3$ and $\lambda_E(2) = 1.5$ nmi.

The small waves appear to be located in the crests of the long waves. As indicated in Table I, the shear for the upper and lower layers is positive and negative, respectively, indicating that the small waves could be expected to be found in crests and troughs of the long waves. As can be seen in Fig. 27, the location of some of the reported turbulence corresponds to the location of small waves.

Test 233, Run 3

In Test 233, light to moderate turbulence was encountered in flights at approximately 54,000 ft over thunderstorms located approximately 150 nmi south of Panama above the Pacific Ocean. It was suspected that flow forced up and over these storms caused the destabilization of stable layers located approximately at the flight levels. The reconstructed 396 K isentrope is shown in Fig. 28. The flight direction was approximately 13 deg to the wind. Short-wavelength waves indicative of instability at this flight level are only slightly apparent. Because of the shortness of the flight record it was not possible to determine the characteristics of any long-wavelength waves which might have been present.

Wind and temperature profiles are also shown in Fig. 28. The wind profile, shown in Fig. 28(a), was determined from flight data. The temperature profile, shown in Fig. 28(b), was determined from rawinsonde data from Howard Air Force Base, Panama. Two stable layers can be seen in the temperature profile and the expected wavelengths were $\lambda_{E(1)} = 1.2$ nmi and $\lambda_{E(2)} = 1.0$ nmi. The expected wavelength based on the combined layers was $\lambda_{E(3)} = 2.9$ nmi.

It was not possible to predict the stability of these layers or to locate the small waves relative to crests or troughs because long-wavelength waves could not be identified on the short record. Other results which were obtained can be seen in Table I and Fig. 28. The wavelengths, $\lambda_0 = 1.6$ to 3.7 nmi, of the short-wavelength waves which were observed in the isentrope shown in Fig. 28(c) are in good agreement with the expected wavelengths $\lambda_E = 1.0$ to 2.9 nmi. The turbulence and short-wavelength waves occurred throughout this segment of the flight path.

Concluding Remarks

The preceding results provide further evidence that very stable layers in the atmosphere can be destabilized by increases in shear caused by long-wavelength waves such as mountain lee waves. The results also provide some evidence that long-wavelength waves occur in stratospheric flow as it is forced up and over thunderstorms and that stable layers in the stratosphere can be destabilized by these waves. The results provided additional confirmation that stability criteria such as that of

Drazin can be used to predict the onset of instability and the approximate wavelengths that occur. A few of the cases also provide sufficient detail to support the method for predicting whether the instability will occur first in a crest or trough of the long-wavelength wave.

It is suspected that the disturbances produced by mountains and thunderstorms are not the only cause of the long-wavelength waves which occur in the atmosphere. These waves may also occur in the vicinity of fronts, at the tropopause, etc. Therefore, this phenomenon (destabilization of stable layers by long-wavelength waves) could be responsible for an appreciable fraction of clear air turbulence encounters.

RECOMMENDATIONS FOR "IN SITU" MEASUREMENTS OF
CAT ENCOUNTERS AND IMPROVED METHODS FOR PREDICTING CAT

Analyses reported herein and in Ref. 1 of data obtained during CAT encounters have shown that CAT may result from the breakdown of initially stable layers resulting from shear induced by long-wavelength waves. In general, the in-flight data which were used for these analyses were not obtained for the specific purpose of verifying this breakdown phenomenon. In some cases, the main purpose for compiling the data was to provide spectral information needed for the design of aircraft structures. In the 1970 Lee Wave Observational Program, the measurements were directed toward determining possible relationships between CAT and mountain lee waves, although this program has provided by far the best information available to date, a complete evaluation of the breakdown phenomenon could not be made with these data because of limitations in the number and detail of the measurements that could be made within the scope of the program. Some recommendations for "in situ" measurements which would help meet this objective were submitted by UARL during a planning session for the 1970 Lee Wave Observational Program. These and other recommendations are included here along with limited recommendations for approaches that might lead to improved CAT prediction methods.

While detailed and accurate atmospheric measurements may be difficult to obtain, the ultimate objective should be to obtain data that will allow a complete evaluation of (1) the structure of long-wavelength waves and the change in properties of the flow through the waves, and (2) the extent of the turbulence in the genesis region. These measurements are discussed below. Flight measurements and other studies should be undertaken to determine conditions under which these long waves occur to confirm their expected properties, and to evaluate wave forecasting methods for different parts of the U. S. where waves frequently occur.

"In Situ" Measurements

On the basis of present knowledge of this flow phenomenon associated with CAT, there appear to be two situations for which further detailed in-flight measurements should be made. CAT caused by mountain lee waves and CAT over thunderstorms. The equipment and procedures that should be used in obtaining these measurements are essentially the same for both situations.

Primary Criteria

In conducting these measurements there are several primary criteria that, in the author's opinion, must be met for an adequate program on wave-induced shear instabilities*:

- (1) The location must be chosen such that there is a high probability that the CAT situation will occur frequently during the program. This is the case for the Lee Wave Observational Programs based at the National Center for Atmospheric Research in Boulder, Colorado during February and March. It would also be true for an investigation of CAT over thunderstorms if the program were based at the National Severe Storms Laboratory at Norman, Oklahoma, or at the NASA facility at Wallops Island, Virginia, during the summer months.
- (2) Adequately instrumented aircraft must be available (see subsequent discussion on instrumentation). If possible, more than one aircraft should be in the area probing the CAT patch. These aircraft must be capable of extended operation in turbulence (i.e., when CAT is encountered, the flight must be continued through the turbulent region). Some of the better aircraft available in the U. S. for this purpose are: the USAF HICAT U-2 (Ref. 11); several RB-57F aircraft operated by the USAF 58th Weather Reconnaissance Squadron based at Kirtland AFB, Albuquerque, N. M.**; the ESSA B-57A based at the ESSA Research Flight Facility, Miami; and the NCAR Sabreliner, based in Boulder. The NASA-Langley B-57B, which is presently operating from Edwards AFB, would also be suitable if additional instrumentation were installed.
- (3) Special upstream rawinsondes must be available. In general, this will require that temporary launching sites be established to supplement rawinsondes obtained from Weather Bureau stations at the standard launching times.

*This discussion is restricted to equipment and procedures, there are, of course, other important considerations such as funding, adequate research manpower, coordination with FAA air traffic control centers, etc.

**Special instrumentation packages for these aircraft have been assembled by the National Aeronautical Establishment in Canada and by the USAF Cambridge Research Laboratories.

- (4) Accurate plotting of the flight position and altitude and an air-ground communications link are necessary. This allows observers on the ground to assess the progress of the flight and direct the flight path relative to the CAT location, the expected locations of forecast wave peaks and troughs, radar information on locations of thunderstorm cells, etc.
- (5) A "quick-look" data reduction and dissemination capability is necessary for day-to-day evaluation of results and for program planning purposes.

Special Instrumentation Required

The following are special instrumentation requirements for investigating the flow characteristics under consideration here:

- (1) An inertial navigation system is needed to continuously and accurately record position information and to provide a cockpit readout of position. The groundspeed derived from the inertial system and the airspeed measurements will also allow local winds to be determined to supplement rawinsonde data. There are less desirable alternatives, such as use of DME (VHF distance measuring equipment) and control of the flight path using ground based radar, but these would not provide sufficient accuracy for investigating small patches of CAT.
- (2) Instrumentation is needed to continuously record pressure altitude, ambient temperature, true airspeed, and heading. The ambient temperature probe need not have particularly high frequency response; the frequencies of interest for studying the flow phenomenon are considerably less than one cycle per sec.
- (3) An instrument is needed which would process pressure altitude and ambient temperature measurements and provide the flight crew with an instantaneous cockpit readout of potential temperature. This would allow the crew to select their flight level so as to probe a particular air mass (for example, a stable shear layer) as it undergoes large-scale vertical and horizontal motions.

These are the primary instrumentation requirements. Most research aircraft are equipped with accelerometers, attitude and direction gyros, and wind vanes. Information from these devices is useful for deriving power spectral distributions of the turbulence. Power spectra are important from the aircraft structural design standpoint, they are also of importance in flights to study the different phases of the atmospheric shear-layer breakdown phenomenon (i.e., the wave-instability phase, the vortex phase, and the turbulence phase).

The NASA-Langley B-57B will be equipped with a device for marking turbulence patches with smoke. If this technique proves to be effective, it would be useful for the type of in-flight research considered here.

Measurements to be Obtained

Wave Measurements

The wave measurements (or measurements of the undulating flow, in the case of the flow over thunderstorms) should have sufficient detail to allow evaluating of changes in stability of the flow due to changes in local shear as the flow proceeds through the wave. This information is needed to verify the hypothesis that the flow breaks down when the Richardson number decreases to less than 0.25 locally. The amplitude of the wave should also be measured to evaluate the method discussed herein for predicting the wave-induced shear. These measurements might be made and the data reduced in the following manner:

- (1) From rawinsonde or aircraft sounding data, locate and identify by local potential temperature the stable layers upwind of the suspected or observed long-wavelength waves. These waves may be occurring as a result of disturbances to the mean flow caused by mountains, thunderstorms or other terrain or meteorological conditions that may be effectively blocking the flow. Data from several stations located transverse to the wind should be examined since the extent of the stable layer relative to the extent of the turbulence is of interest.
- (2) Conduct flights at constant altitude at several closely spaced altitudes within the stable layer and continuously measure wind and temperature. Then, at the crests and troughs obtain wind and temperature profiles by crossplotting the data. From these measurements it should be possible to determine the wave-induced shear, $\Delta(\partial V/\partial z)$, the minimum Richardson number R_{iMIN} , and the wave amplitude, a .
- (3) Fly through several wavelengths of the wave to determine whether or not the layer has become unstable.

Turbulence Measurements

Results of the turbulence measurements should show the location of the genesis region with respect to the long-wavelength crests and troughs, whether or not the instability is more wavelike in the genesis region than in the turbulent region, and the extent of the turbulence relative to the extent of the stable layer. These measurements might be made and the data reduced in the following manner:

- (1) Find the genesis region with respect to the wave structure by having the aircraft fly upstream in the wave, noting the location at which the turbulence ceases. Compare this location with the location of crests and troughs as determined from wave measurements.
- (2) Make spectral measurements of the turbulence to determine if discrete frequencies or wavelengths are apparent in the spectra in the genesis region. Compare these wavelengths with wavelengths predicted on the basis of the thickness of the layer and Drazin's criterion (see previous discussion).
- (3) Make flights both transverse and parallel to the wind direction to determine the extent of the turbulence in these directions, and compare the extent of the turbulence with the extent of the stable layer as determined from rawinsonde or aircraft sounding data. If the thicknesses are about the same, it would provide additional evidence that it is the stable layers that are breaking down and causing CAT. Also, it would be of interest to determine how the turbulent region develops --- does the thickness of the layer increase, remain constant or decrease? Prediction techniques would be improved if, in addition to predicting the onset of the CAT instability, information about vertical and horizontal extent of the turbulence could also be predicted.

Improved CAT Prediction Methods

In general, most CAT prediction techniques are based on synoptic features which are present and on a comparison of the values of one or more atmospheric parameters (such as horizontal wind shear, vertical wind shear, horizontal temperature gradient, streamline curvature, etc.) with empirically determined critical values. In most cases, there is no physical model for the breakdown mechanism. An example of such a prediction technique is given in Ref. 13. The technique is based on horizontal and vertical temperature gradients (determined from rawinsondes along the flight route) and is quite simple to use.

It is recommended that consideration be given to evaluation of a prediction procedure based on the mechanism of wave-induced instability of initially stable shear layers. This procedure would be comprised of three distinct operations contained in a single computer program: (1) the rawinsonde from a given station would be processed to predict the long-wave amplitude necessary to destabilize each shear layer appearing in the profiles; (2) the rawinsonde would be used with wave forecasting techniques and/or statistical data to determine the probability that waves

would occur during the forecast period and what their amplitudes might be, and (3) the results from (1) and (2) would be combined to estimate the probability that wave-induced instabilities, and hence CAT, would occur during the forecast period, and to identify the altitudes and locations at which they would occur.

This procedure is outlined below along with some of the reasoning involved. Additional information would be required, particularly on wave forecasting, before such a procedure could be thoroughly evaluated.

Calculation of Required Long-Wave Amplitudes

This portion of the procedure would be relatively straight-forward. Equation (17) can be re-written to yield the minimum long-wave amplitude necessary to destabilize ($Ri_{MIN} = 0.25$) a shear layer:

$$a = \frac{2N_M - |(\partial V/\partial z)_0|}{N_M^2 - n^2} \cdot V_0 \quad (20)$$

The rawinsonde data would be processed by the program to identify shear layers (using the temperature profile) and, for each layer, to calculate the mean flow parameters V_0 , $(\partial V/\partial z)_0$, N_M , and n . In calculating n , a long-wave wavelength of $\lambda_{LW} = 15$ nm could be used since waves of about this wavelength occur frequently, moreover, n is small, so that large percentage changes in n have little effect on the computed amplitude, a . Using the mean flow parameters, the required amplitude for instability would be calculated for each shear layer. The following table (based on the Denver rawinsonde for 2200 GMT on February 13, 1968, see Table I of Ref. 1) illustrates the results of this calculation:

Layer	Mean Altitude, ft	Amplitude, a, Req'd. for $Ri_{MIN} = 0.25$, ft
7	67,195	2690
8	59,232	4980
9	62,021	3480
10	57,715	5780
11	43,475	5700
12	37,967	10,120

Thus, layer 7 would require a mountain lee wave amplitude (or a height increase in flowing over a thunderstorm, etc.) of 2690 ft for instability. Layer 12 would require an amplitude of 10,120 ft.

Long-Wave Amplitude Forecast

At this point, the characteristics of waves in the local zone of the forecast must be considered. The U. S. has eighteen designated mountain wave zones (Ref. 14) --- ranging from Zone 1 - Cascades and Coastal Ranges (Washington and Oregon) to Zone 18 - Adirondacks and White Mountains. For forecasting CAT induced by mountain lee waves, good techniques for forecasting the occurrence and approximate amplitudes of waves would be required. These techniques are usually empirical --- they rely on such parameters as average lapse rate, wind direction and strength at mountain-top level, positive vorticity advection, etc. Where the techniques have been used extensively, they have been developed to confidence levels of 80 to 90 percent --- forecasters can fairly consistently predict whether waves will occur and whether they will be strong or weak. If this CAT prediction technique were to prove successful in one or two zones, it would be necessary to probe mountain waves and establish wave forecasting techniques for other zones of interest.

Screening and CAT Forecast

The particular example given in the preceding table is in Zone 12 - Continental Divide, northern Colorado. Wave forecasting techniques for this zone are especially well developed due mostly to activities at NCAR and the ESSA Research Laboratories in Boulder. The computer routine for this zone would probably disregard layers having values of required amplitude greater than 3,000 or 4,000 ft; even though strong waves can occur in this zone, the amplitudes of the waves would rarely, if ever, exceed these amounts. Thus, the initial screening would eliminate all but layers 7 and 9 from consideration.

The final CAT forecast would depend upon the local wave forecast. If, in this example, it was likely that strong waves would occur during the forecast period, then the forecast would probably be "possibility of CAT at approximately 67,000 ft and 62,000 ft in vicinity of eastern slope of Colorado Rockies." If it was unlikely that waves would occur, or if they would be weak, a "no CAT" forecast would be issued.

Concluding Remarks

It is suggested that an evaluation of the proposed prediction technique be undertaken, concentrating first on a well-documented lee-wave zone such as in the vicinity of Boulder. If the technique is successful, it could then be extended to

other zones and could be expanded to forecast wave-induced convective instabilities as well (although the latter are not usually associated with CAT*). The possibility of forecasting wave-induced shear instabilities in the stratosphere using simple models of fronts and thunderstorms could also be investigated if the initial evaluation proves successful.

*Widespread ascent of air can lead to formation of convective instability in shallow layers of air. This instability is dependent upon the air in the lower part of the layer becoming saturated as it is lifted while the air in the upper part is still not saturated. This leads to convective cloud patterns ("mackerel" skies).

REFERENCES

1. Clark, J. W., R. C. Stoeffler, and P. G. Vogt: Research on Instabilities in Atmospheric Flow Systems Associated with Clear Air Turbulence. NASA Contractor Report CR-1604, prepared under Contract NASW-1582, June 1970; also United Aircraft Research Laboratories Report H910563-9, June 1969.*
2. Drazin, P. G.: The Stability of a Shear Layer in an Unbounded Heterogeneous Inviscid Fluid. Journal of Fluid Mechanics, Vol. 4, 1958, pp. 214-224.
3. Hazel, P.: Instabilities of Stratified Shear Flow. Paper submitted for publication in Journal of Fluid Mechanics, 1968.
4. Phillips, O. M.: The Dynamics of the Upper Ocean. Cambridge University Press, 1966.
5. Haurwitz, B.: Dynamic Meteorology. McGraw-Hill Book Company, Inc., New York, 1941.
6. Woods, J. D.: Wave-Induced Shear Instability in the Summer Thermocline. Journal of Fluid Mechanics, Vol. 32, 1968, pp. 791-800.
7. Ludlam, F. H.: Characteristics of Billow Clouds and Their Relation to Clear Air Turbulence. Quarterly Journal of the Royal Meteorological Society, Vol. 93, 1967, pp. 419-435.
8. Mitchell, F. A. and D. T. Prophet: Meteorological Analysis of Clear Air Turbulence and Its Detection. Boeing Scientific Research Laboratories Report DL-82-0740, Seattle, Washington, August 1968.
9. Spillane, K. T.: Clear Air Turbulence and Supersonic Transport. Nature, Vol. 214, No. 5085, April 15, 1967, pp. 237-239.
10. Hardy, K. R.: Radar Echoes from the Clear Air. Paper prepared for NATO Advanced Study Institute on the Structure of the Lower Atmosphere and Electromagnetic Wave Propagation, Aberystwyth, Wales, September 2-15, 1967.

*Also summarized in Clark, J. W.: Laboratory Investigations of Atmospheric Shear Flows Using an Open Water Channel. Paper presented at AGARD-NATO Specialists' Meeting on "The Aerodynamics of Atmospheric Shear Flows," Munich, Germany September 15-17, 1969. AGARD Conference Proceedings No. 48, February 1970.

REFERENCES (Continued)

11. Crooks, W. M., F. M. Hoblit, F. A. Mitchell, et al.: Project HICAT --- High Altitude Clear Air Turbulence Measurements and Meteorological Correlations. Air Force Flight Dynamics Laboratory Report AFFDL-TR-68-127, Vol. I and Vol. II, prepared by Lockheed California Company, November 1968.
12. Danielson, E. F. and R. T. Duquet: A Comparison of FPS-16 and GMD-1 Measurements and Methods for Processing Wind Data. Journal of Applied Meteorology, Vol. 6, No. 5, 1967, pp. 824-836.
13. Ashburn, E. V., D. E. Waco, and F. A. Mitchell: Development of High Altitude Clear Air Turbulence Models. Air Force Flight Dynamics Laboratory Report AFFDL-TR-69-79, prepared by Lockheed California Company, November 1969.
14. Anon.: CAT Time. Accident Prevention Bulletin 69-1, Flight Safety Foundation, Inc., Arlington, Va., January 1969.
15. Baumeister, T., ed.: Marks' Mechanical Engineers' Handbook. Sixth Edition, McGraw-Hill Book Company, Inc., New York, 1958.
16. Hama, F. R.: Streaklines in a Perturbed Shear Flow. The Physics of Fluids, Vol. 5, No. 6, June 1962, pp. 644-650.

LIST OF SYMBOLS

a	Amplitude of wave (half the height from trough to peak), ft or in.
b	Exponent in theoretical velocity profile (Eq. (6)), dimensionless
c	Complex wave velocity, $c = c_r + i c_i$, ft/sec
c_i	Imaginary part of complex wave velocity, ft/sec
c_r	Real part of complex wave velocity, ft/sec
d	Shear-layer scale length parameter for describing velocity profiles, $d = (\Delta V/2)/(\partial V/\partial z)_0$, ft
g	Gravitational constant, 32.2 ft/sec ²
i	Unit imaginary number, $\sqrt{-1}$, dimensionless
l	Unit length, ft
n	Wave frequency, $2\pi V_0/\lambda_{LW}$, sec ⁻¹
N_M	Brunt-Vaisala frequency, $N_M = \sqrt{(g/T_0) \cdot [(\partial T/\partial z) - (\partial T/\partial z)_{ad}]}$ in the atmosphere and $\sqrt{(-g/\rho)(\partial \rho/\partial z)}$ in the water channel, sec ⁻¹
r	Radial coordinate measured from center of curvature of water channel, ft or in
Re	Reynolds number, $Re = Vl/\nu$, dimensionless
Ri	Richardson number, $Ri = (g/T_0) [(\partial T/\partial z) - (\partial T/\partial z)_{ad}] / (\partial V/\partial z)^2$ in the atmosphere and $(-g/\rho) (\partial \rho/\partial z) / (\partial V/\partial z)^2$ in the water channel, dimensionless
Ri_0	Initial or upstream Richardson number, dimensionless
Ri_{MIN}	Minimum Richardson number caused by influence of long-wavelength wave, dimensionless
s	Coordinate along centerline of curved water channel, ft or in.
t	Time, sec
T	Temperature, deg C, K, or F

LIST OF SYMBOLS (Continued)

T_0	Temperature at center of shear layer, deg C, K, or F
V	Velocity, ft/sec or kts
V_0	Velocity at center of shear layer or velocity of long-wavelength wave, ft/sec or kts
V_1, V_2	Velocities in upper and lower streams bounding shear layer, respectively, for hyperbolic profiles, or minimum and maximum velocities in shear layers with "S-shaped" profiles, ft/sec
w	Perturbation velocity (Eq. (9)), ft/sec
x	Downstream coordinates in water channel (Fig. 30), ft or in.; also distance along flight path, nmi
y	Transverse coordinate in water channel (Fig. 30), ft or in.
z	Vertical coordinate in water channel (Fig. 30), ft or in.; also pressure altitude, ft
z_0	Vertical coordinate of center of shear layer in water channel, ft or in.
z_1, z_2	Vertical distance to V_1 and V_2 , respectively, in.
α	Wavenumber of small-amplitude waves associated with instabilities in shear layers, $\alpha = 2\pi / \lambda$, ft ⁻¹
β	Parameter in density profile equation (Eq. (2)), $\beta = R_1 \cdot d \cdot (\partial V / \partial z)_0^2 / g$, dimensionless
ΔV	Velocity difference parameter for describing velocity profiles' (Eqs. (1), (6), and (7)), ft/sec
$\Delta(\partial V / \partial z)$	Change in shear caused by influence of long-wavelength wave, sec ⁻¹
$(\partial T / \partial z)_{ad}$	Adiabatic lapse rate, $(\partial T / \partial z)_{ad} = -2.98 \times 10^{-3}$ deg C/ft
$(\partial T / \partial z)_0$	Initial upstream temperature gradient, deg F/ft
$(\partial V / \partial z)_0$	Initial or upstream shear, sec ⁻¹ or kts/1000 ft

LIST OF SYMBOLS (Continued)

η	Ratio of Brunt-Vaisala frequency to wave frequency, $\eta = N_M/n$, dimensionless
θ	Potential temperature, deg K
λ	Wavelength of small-amplitude waves associated with instabilities in shear layers, ft or in.
$\lambda_E()$	Wavelength of instability estimated to occur in atmospheric shear layer (number in brackets identifies layer), ft or mm
λ_{LW}	Wavelength of lee wave or long-wavelength wave in water channel, in., ft, or mm
λ_o	Wavelength of instability observed in atmospheric shear layer, ft or mm
ν	Kinematic viscosity, ft ² /sec
ρ	Density of water or air, slugs/ft ³
ρ_o	Density of water or air at center of shear layer, slugs/ft ³
ρ_1, ρ_2	Densities in upper and lower streams bounding shear layer, respectively, slugs/ft ³
$\phi(z)$	Perturbation amplitude function in shear-layer stability analysis, ft ² /sec
ψ'	Perturbation stream function in shear-layer stability analysis, ft ² /sec

Subscripts

m	Measured value
p	predicted value

APPENDIX I - DESCRIPTION OF EQUIPMENT AND PROCEDURES

UARL Open Water Channel

Figure 29 is a photograph of the UARL Open Water Channel and Fig. 30 is a sketch indicating its major features. This facility provides a 2-ft-wide by 6-in.-deep by 10-ft-long, non-recirculating, open channel flow. The lucite side walls extend about 2 in. above the surface of the water. They are held firmly in place by weights and the joints where the walls meet the glass-topped table which forms the channel floor are sealed. The walls can be adjusted from the straight-channel position (shown by the solid lines in Fig. 30) to any desired curved-channel position (shown by the dashed lines) with the minimum centerline radius of curvature being about 6 ft. The flow is illuminated from beneath the glass floor using fluorescent lights (visible in Fig. 29).

Shaped filter beds made from a porous foam material* are used to introduce desired vertical and transverse velocity profiles at the upstream end of the channel (Fig. 30). A filter bed shaped to provide a "three-dimensional" velocity profile is shown in Fig. 31 and is described in more detail in Appendix III. The foam material is bonded to porous stainless steel supporting structures which are bolted to the cover of the plenum. Several different adjustable sluices, including some that are porous, are used at the downstream end of the channel. They provide usable mean channel velocities up to about 1.0 ft/sec.

Hot-water nozzles in the plenum are used to introduce vertical and transverse temperature gradients and, hence, density stratification. Figure 30 shows schematically the nozzles used to create vertical gradients; twelve such nozzles are actually located in the plenum. Six similar nozzles (not shown) are installed with their axes vertical to create transverse temperature gradients. A filter consisting of screens and a 3-in.-thick layer of pebbles is used downstream of the hot-water nozzles to smooth the temperature profiles.

With the channel walls straight, the origin of the coordinate system used to described points in the flow is at the juncture of the tapered filter bed, the floor of the channel, and the side wall nearest the observer (see Fig. 30); x is measured in the downstream (streamwise) direction, y is measured transversely from the wall, and z is measured vertically from the floor of the channel. With the channel walls

*Scott Industrial Foam, a product of the Scott Paper Company, Foam Division, 1500 East Second Street, Chester, Pennsylvania.

curved, positions in the flow are described by z , by the local radius r measured from the center of curvature of the channel, and by the running coordinate s measured from the filter bed along the centerline of the channel in the downstream direction.

The central region of the channel away from the floor and side-wall boundary layers and away from the free surface is the region of primary interest. The gradients attainable in this central region vary with the local temperature of the water and with the shear-layer thickness. The approximate ranges of velocities, temperatures, and gradients in tests reported herein were:

Local Velocities:	$0.02 < V < 0.5$ ft/sec
Velocity Gradients:	$-3.5 < \partial V / \partial z < + 3.5$ sec ⁻¹
Local Temperatures:	$40 < T < 100$ F
Temperature Gradients:	$0 < \partial T / \partial z < 300$ deg F/ft

Use was made of the curves in Fig. 32 (derived from tabulated data in Ref. 15) for calculating the Richardson numbers* for these flow conditions. The range of Richardson number was from 0 to near infinity (for $\partial V / \partial z$ approaching 0).

The Reynolds numbers per unit length in the channel vary over wide ranges due to the wide ranges of both velocity and temperature. In the present investigation, the minimum value was $Re/\ell = 1200$ per ft for $V = 0.02$ ft/sec and $T = 40$ F; the maximum was $Re/\ell = 67,800$ per ft for $V = 0.5$ ft/sec and $T = 100$ F.

The floor of the channel slopes downward slightly toward the sluice. Thus, some provision is made for the effect on the flow of floor boundary layer growth. Nevertheless, care must be taken to assure that observations are not influenced by this boundary layer, particularly at low channel speeds.

Instrumentation and Test Procedures

Dye Tracing

Neutrally buoyant fluorescent dye** is used to obtain qualitative information about the nature of the flow. It is an effective method for identifying the presence of internal waves, vortices, and turbulence; it can also be used to determine the

* $Ri = (-g/\rho)(\partial\rho/\partial z)/(\partial V/\partial z)^2 = (-g/\rho)(\partial\rho/\partial T)(\partial T/\partial z)/(\partial V/\partial z)^2$; using the measured T , ρ and $\partial\rho/\partial T$ were determined from Fig. 32.

**Uranine concentrate powder in water; concentrate available from Sagamore Color & Chemical Co., 82 Braintree Street, Alston Sta., Boston, Mass.

wavelengths of internal waves. The dye is injected through 0.020-in.-ID stainless steel hypo tubes located immediately upstream of the tapered filter bed. The dye streamers trace out streamlines in steady flows and streaklines in unsteady flows. In the latter case, caution must be used in their interpretation (see discussion in Ref. 16).

Bubble Tracing

Measurements of the velocity profiles are made using the hydrogen bubble wire technique. A voltage is applied to a 0.001-in.-dia platinum wire extending from the channel floor through the surface of the water. Hydrogen bubbles are generated by electrolysis. The voltage may be pulsed at 10, 5, 2, or 1.0 cps to generate chains of bubbles which drift downstream with the flow. The local velocity can be determined by photographing the chains, determining the distance between chains from the photographs and dividing by the time between chains. At low speeds, only the chains closest to the wire are used to prevent errors due to rising of the bubbles. The voltage can also be applied continuously to create a sheet of bubbles for flow visualization.

Thermometry

All of the temperature measurements reported herein were made using a standard submersible mercury-filled thermometer.

APPENDIX II - METHOD FOR FITTING HAZEL'S THEORETICAL VELOCITY PROFILE
TO DATA FOR "S-SHAPED" VELOCITY PROFILES

This appendix describes the method which was used to fit the theoretical velocity profile of Hazel (Ref. 3) to the "S-shaped" velocity profiles obtained experimentally in the UARL Open Water Channel. The theoretical profile was given previously in Eq. (6) as

$$V = V_0 + \left(\frac{\Delta V}{2}\right) \operatorname{sech}^b\left(\frac{z-z_0}{d}\right) \tanh\left(\frac{z-z_0}{d}\right) \quad (21)$$

where the mean velocity, $V_0 = (V_1 + V_2)/2$, is shown in Sketch C on page 12. The minimum and maximum velocities of the profile, V_1 and V_2 , respectively, are also shown. Fitting Eq. (21) to a measured profile involves determining the constants b , ΔV , and d . In the following development this will be done by matching the velocities V_1 and V_2 at z_1 and z_2 , the shears at z_1 and z_2 (which are zero), and the mean shear, $(\partial V/\partial z)_0$, at z_0 of the measured profile to the theoretical profile of Eq. (21).

The shear can be obtained by differentiating Eq. (21) with respect to the vertical coordinate z :

$$\partial V/\partial z = \left(\frac{\partial V}{\partial z}\right)_0 \left\{ \left[(b+1) \operatorname{sech}^2\left(\frac{z-z_0}{d}\right) \right] - b \right\} \operatorname{sech}^b\left(\frac{z-z_0}{d}\right) \quad (22)$$

In this equation, the following substitution was made:

$$(\partial V/\partial z)_0 = \frac{\Delta V}{2d} \quad (23)$$

At z_1 the shear is zero, so Eq. (22) yields

$$\operatorname{sech}(z_1-z_0/d) = \sqrt{\frac{b}{b+1}} \quad (24)$$

Substituting Eq. (24) into Eq. (21) provides an expression for V_1 :

$$V_1 = V_0 + \left(\frac{\Delta V}{2}\right) b^{\frac{b}{2}} (b+1)^{\frac{-b+1}{2}} \quad (25)$$

Replacing V_0 with $(V_1 + V_2)/2$ in Eq. (25), yields an equation for ΔV as a function of b , V_1 , and V_2 :

$$\Delta V = (V_1 - V_2) b^{\frac{-b}{2}} (b+1)^{\frac{b+1}{2}} \quad (26)$$

Now, substituting ΔV from Eq. (23), $(z_1 - z_0)/d$ from Eq. (24) and $V_0 = (V_1 + V_2)/2$ into Eq. (25) results in

$$\left[(z_1 - z_0)/(V_1 - V_2)\right] (\partial V/\partial z)_0 = \frac{1}{2} \left(\operatorname{arccosh}\left(\frac{b+1}{b}\right)^{\frac{1}{2}}\right) b^{\frac{-b}{2}} (b+1)^{\frac{b+1}{2}} \quad (27)$$

Using a similar development but with the condition that the shear is also zero at z_2 yields an expression that is similar to Eq. (27) except that z_1 is replaced by z_2 and the right side of the equation is negative. Combining this result with Eq. (27) produces

$$\left[(z_1 - z_2)/(V_1 - V_2)\right] (\partial V/\partial z)_0 = \left(\operatorname{arccosh}\left(\frac{b+1}{b}\right)^{\frac{1}{2}}\right) b^{\frac{-b}{2}} (b+1)^{\frac{b+1}{2}} \quad (28)$$

The left side of Eq. (28) can be determined entirely from properties of the measured profile. The right side is only a function of b . Therefore, the value of b for a given profile can be obtained by plotting b versus the right side of Eq. (28) and entering the plot at the value given by the left side of Eq. (28). After obtaining b for the profile, ΔV can be obtained from Eq. (26) and, finally, d can be obtained from Eq. (23). Thus, all of the parameters needed in Eq. (21) to describe the velocity V as a function of z have been determined.

APPENDIX III - PRELIMINARY STUDIES OF THE STABILITY OF
"THREE-DIMENSIONAL", STRAIGHT, STRATIFIED SHEAR FLOWS

The primary purpose of this part of the fluid mechanics program was to perform a preliminary investigation of the effects of "three-dimensionality" on the stability of straight stratified shear flows. Such effects might be important in the atmosphere where two-dimensional flows are disturbed locally, as in flows influenced by a single mountain or the blocking effect of a single thunderstorm cell.* It is planned to study this phenomenon in more detail at a later date.

Summary of Experiments with "Three-Dimensional" Velocity Profiles

The results obtained from previous studies of the stability of two-dimensional flows having hyperbolic tangent profiles and "S-shaped" profiles formed the basis for planning the experiments. The primary objective of the tests was to determine the effects of "three-dimensionality" on the stability of straight, stratified, shear flows. Particular objectives were (1) to determine if the initial disturbances were wavelike as were those for two-dimensional hyperbolic and "S-shaped" velocity profiles, (2) to determine methods for predicting their wavelength if the initial disturbances are wavelike, (3) to observe the stages of breakdown, and (4) to determine the critical value of the Richardson number for stability.

Filter Bed Used to Develop "Three-Dimensional" Velocity Profiles

A photograph of the shaped filter bed typical of those used to develop velocity profiles in these tests is shown in Fig. 31. The filter provided no velocity gradient (i.e., the same velocity at all heights above the channel floor) across the span of the channel except in the center 1/3 of the channel span where a hyperbolic tangent vertical velocity gradient was provided. The spanwise distance allowed for transition from hyperbolic tangent velocity gradient to zero velocity gradient was large enough so that horizontal velocity gradients were very small compared to the vertical gradients. It was estimated (using data from Ref. 1) that the distance required for a disturbance produced by the horizontal gradients to grow to observable size was greater than the channel length. Observance of dye streamers in the transition region verified that no disturbance of the flow by the horizontal velocity gradients was discernable.

*It is questionable whether the results of these preliminary studies are applicable to atmospheric flows since the transverse widths of the shear layers were about equal to the wavelengths of the disturbances; such narrow shear layers might not occur in the atmosphere.

Summary of Experimental Results

Velocity, Temperature, and Density Profiles

Velocity, temperature, and density profiles for typical flow conditions are shown in Fig. 33. These data are for three different values of Richardson number: $Ri = 0$ (Fig. 33(a)), $Ri = 0.07$ (Fig. 33(b)), and $Ri = 0.14$ (Fig. 33(c)). The velocity and temperature measurements were made within 2 in. downstream from the filter bed on the channel centerline. It was found that neither a hyperbolic tangent nor an "S-shaped" profile was particularly representative of the experimental velocity profiles (this can be corrected in future experiments). The temperature and density gradients shown in Fig. 33(b) and (c) indicate that the temperature and density vary approximately linearly through the thermocline which separates the two regions of the flow having approximately uniform temperatures.

Characteristics of the Breakdown of the Flow

Figure 34 illustrates the stages observed as the flow in the shear layer breaks down. The four distinct and repeatable stages which occur are similar to those observed in tests of two-dimensional flows having hyperbolic tangent and "S-shaped" velocity profiles; dye traces illustrating the phenomenon are shown in the sketch and in photographs. The photographs were taken through the lucite sidewall (Fig. 30); the flow is from left to right. The scale appearing in the photographs was immersed in the flow close to the dye traces.

In Fig. 34(a), the flow appears undisturbed. Neither the dye traces nor the hydrogen bubble traces show visual evidence of any perturbation.

In Fig. 34(b), which is 7.5 in. further downstream, the center dye trace indicates the presence of a wave amplifying as it progresses downstream. The wave has a wavelength of about $\lambda = 3.0$ in. and an amplitude (half the distance from trough to peak) of about 0.1 in. at this point. By placing dye probes at several transverse locations it was verified that the wave was only in the central portion of the channel and that the disturbance had transverse components.

In Fig. 34(c), which is another 10.5 in. downstream, the waves have rolled up into vortices. The circulation of the vortices has the same sense as the vorticity introduced by the shear --- the shear is negative in this flow condition, and all the vortices rotated counterclockwise. These vortices grew slightly in size as they drifted downstream. Their downstream drift velocity was found to be approximately V_0 , the velocity upstream at the center of the shear layer. The flow was also determined to be three-dimensional at this stage.

In Fig. 34(d), which is another 41 in. downstream --- 62 in. downstream of the filter bed --- the vortices have "burst" and the flow appears turbulent.

Comparison of Results with Drazin's Stability Criterion

A summary of the results obtained in these tests is shown in Fig. 35. It was not possible to find a theoretical criterion for the flow conditions studied in these tests and therefore the results were compared (Fig. 35) with Drazin's criterion which was developed for two-dimensional flows having hyperbolic tangent velocity profiles. For each flow condition, the Richardson number was calculated using the velocity gradient, $(\partial V/\partial z)_0$, and temperature gradient, $\partial T/\partial z$, at the center of the shear layer from the profiles measured on the channel centerline. The scale length $d = \Delta V/2 (\partial V/\partial z)_0$ was calculated using the velocity gradient, $(\partial V/\partial z)_0$, and the velocity difference ΔV from the velocity profile; ΔV was based on maximum and minimum velocities in the vicinity of the edges of the shear layer (Fig. 33). The wavenumber, $\alpha = 2\pi/\lambda$, was calculated using wavelengths determined from photographs of the dye traces. Thus, each flow condition at which waves were observed is identified by a point on the plot of αd versus Ri .

The symbols in Fig. 35 denote different flow characteristics that were observed. The open circles denote conditions at which waves were observed; that is, waves appeared and then were damped out without making the transition to vortices. The wavelengths of these waves was between 1 and 5 in. The flags on the symbols indicate cases for which the waves were intermittent or the wave amplitude was small. The half-solid symbol denotes conditions at which waves transitioned to vortices; that is, vortices occurred and then were damped out without making the transition to turbulence. The full-solid symbol denotes flow conditions at which the full sequence of events occurred --- waves, vortices, and turbulence. The crosses indicate conditions at which no waves of the type associated with instability occurred. At some conditions (indicated by (LW)), standing long-wavelength (10 to 24 in.) waves occurred. These long-wavelength waves were investigated in some detail for two-dimensional flows and were discussed in detail previously in this report.

Examination of Fig. 35 indicates that, except for two cases, the dimensionless wavenumbers for cases where instability was observed are in agreement with Drazin's stability criteria for two-dimensional flows having hyperbolic tangent velocity profiles. In two cases for which instability was observed the dimensionless wavenumbers were greater than 1.0. This is not unexpected since the velocity profiles were somewhat "S-shaped". Theoretical studies by Hazel (Ref. 3) and experimental studies discussed previously in this report indicate that the dimensionless wavenumber, αd , can be greater than 1.0 for "S-shaped" velocity profiles. However, the data also indicate that the critical value of Richardson number for neutrally stable flow may be somewhat less than the two-dimensional value of 0.25. In several instances stable flows were observed for which the Richardson number was between 0.08 and 0.20. There was some overlap in the data; in one instance stable flow was observed for Ri as small as 0.058, however, in three instances instability was observed for Ri as large as 0.06 to 0.075. For the unstable cases, damped vortices were observed in one case, small-amplitude waves in a second, and small-amplitude intermittent waves in the third. Further tests are needed before this apparent inconsistency in the results is understood.

TABLE I

CHARACTERISTICS OF EXPECTED AND OBSERVED SHORT-WAVELENGTH WAVES
ASSOCIATED WITH CAT IN LEE WAVES AND OVER THUNDERSTORMS

EXPECTED WAVELENGTH, $\lambda_E = (2\pi/\sqrt{z}) 2d$

Case	EXPECTED WAVES							OBSERVED WAVES					Data Shown on Figures				
	Stable Layer and Rawinsonde Station***	Mean Altitude, ft	θ deg K	Thickness, 2d - ft	$\lambda_E(\)$, mi	Expected Location in Long Waves	R^2_{10}	Based on $\Delta(\partial V/\partial z)$		Based on $2\Delta(\partial V/\partial z)$		Short Waves Observed?		λ_o , mi	Location in Long Waves	Amplitude of Long Waves a - ft	
								R^2_{MIN}	Short Waves Likely? ($R^2_{MIN} < 0.25$)	R^2_{MIN}	Short Waves Likely? ($R^2_{MIN} < 0.25$)						
LEE WAVES - HICAT																	
TEST 264, RUN 16	1-UCC	63,370	470	680	0.5	trough	.77	0.47	no	0.13	yes	yes	0.1-1.0	crests and troughs	1,000	13 and 14	
	UCC*	63,370	470	680	0.5	crest	0.34	0.11	yes	0.05	yes				1,000		
	2-UCC	57,989	446	1,050	0.8	trough	9.7	1.02	no	0.37	no				1,000		
	3-DEN	60,067	461	870	0.6	-	∞	0.61	no	0.15	yes				1,000		
	DEN*	60,067	461	870	0.6	trough	8.4	0.38	no	0.12	yes	1,000					
TEST 267, RUN 8 RUN 9 RUN 28	1-ABQ*	52,625	405	750	0.6	trough	0.18	NA	NA	NA	NA	yes	0.4-0.6		1,000	15 and 16	
	1-ABQ*	52,625	405	750	0.6	trough	0.18					yes	0.3-0.5		1,000		
	2-ABQ*	56,350	425	900	0.7	crest	162					yes	0.8-1.5		1,000		
	3-ABQ*	56,875	434	150	0.1	crest	1900								1,000		
TEST 282, RUN 2	1-GBY	58,300	433	2,100	1.5	trough	5.7	0.78	no	0.29	no	yes	0.2-1.0	trough	1,000	17 and 18	
	2-GBY	53,125	410	2,250	1.5	trough	17.3	1.51	no	1.05	no				1,000		
LEE WAVES-COLORADO																	
February 13, 1970	1	1-GJT	60,150	448	5,200	3.8	trough	222	1.7	no	0.47	no	yes	2.0-4.0	crest and trough	1,000	19 and 20
		3-DEN	61,250	458	2,750	2.0	crest	840	1.44	no	0.38	no				1,000	
	2	4-DEN	55,700	422	1,200	0.9	crest	2,000	3.9	no	1.0	no	no	1,000			
		5-DEN	48,750	386	4,300	3.2	trough	10.4	6	no	3.5	no	500				
	3	2-GJT	36,825	333	4,150	3.0	crest	194	35	no	13	no	no	500			
		6-DEN	35,575	330	1,550	1.1	crest	63	19	no	8.9	no	500				
February 17, 1970	1	1-GJT	62,400	449	2,800	2.0	trough	218	0.98	no	0.26	no	no			800	21 and 22
		5-DEN	66,775	496	850	0.6	-	4,000	-	no	-	no				1,500	
		6-DEN	62,175	456	1,850	1.4	trough	4,167	1.59	no	0.40	no				800	
	2	7-DEN	60,825	434	850	0.6	trough	6,540	0.10	yes	0.02	yes	yes	800			
		8-DEN	60,125	424	450	0.3	crest	330	0.27	no	0.07	yes	yes	800			
		9-DEN	61,525	445	3,150	2.3	trough	4,500	0.15	yes	0.04	yes	yes	800			
	3	2-GJT	49,200	383	2,000	1.5	trough	1.2	0.69	no	0.44	no	no	800			
		3-RLG	51,200	373	3,700	2.7	trough	1.3	0.70	no	0.44	no	no	1,500			
		4-RLG	26,050	322	500	0.3	crest	8.2	2.68	no	1.31	no	no	1,500			
		10-DEN	51,625	386	750	0.6	trough	2.5	1.12	no	0.62	no	no	1,500			
		11-DEN	50,375	377	1,750	1.3	trough	4.64	1.45	no	0.68	no	no	1,500			
		12-DEN	33,700	336	800	0.6	crest	7.7	2.93	no	1.53	no	no	1,800**			

* Temperatures from rawinsonde at indicated station and winds from aircraft data

** a is assumed amplitude based on nearest isentrope

*** Rawinsonde Stations UCC-Yucca Flats, DEN-Denver, ABQ-Albuquerque, GBY-Granby, GJT-Grand Junction, RLG-Kremmling, AMA-Amarillo, OKC-Oklahoma City, and MEHO-Howard Air Force Base (Panama)

(Continued)

TABLE I
-CONTINUED-

Case	EXPECTED WAVES											OBSERVED WAVES				Data Shown on Figures
	Stable Layer and Rawinsonde Station***	Mean Altitude, ft	θ deg K	Thickness, 2d - ft	λ_R (), nmi	Expected Location in Long Waves	R_{10}	Based on $\Delta(\partial V/\partial z)$ Short Waves Likely? ($R_{1MIN} < 0.25$)		Based on $2\Delta(\partial V/\partial z)$ Short Waves Likely? ($R_{1MIN} < 0.25$)		Short Waves Observed?	λ_o , nmi	Location in Long Waves	Amplitude of Long Waves a - ft	
LEE WAVES-COLORADO CONTINUED																
February 18, 1970	1	1-GJT	81,360	621	5,220	3.8	crest	1,488	0.19	yes	0.05	yes	no data			1,000**
		2-GJT	70,465	538	6,530	4.8	trough	57	0.42	no	0.11	yes				1,000**
		3-GJT	65,075	484	4,250	3.1	trough	70	1.0	no	0.29	no				1,000**
		4-GJT	63,340	514	10,780	7.9	trough	46	0.9	no	0.26	no				1,000**
		20-DEN	67,925	517	1,350	1.0	trough	197	0.61	no	0.16	yes				1,000**
		21-DEN	66,910	505	680	0.5	trough	49	0.55	no	0.15	yes				1,000**
		22-DEN	67,585	513	2,030	1.5	trough	85	0.68	no	0.19	yes				1,000**
	2	5-GJT	57,700	440	1,800	1.3	trough	47	1.2	no	0.51	no	1,000**			
		6-GJT	48,615	384	2,170	1.6	crest	5,800	42	no	11.5	no	1,000**			
		7-GJT	32,325	346	350	0.3	crest	21.5	4.1	no	1.7	no	1,050			
		12-RLG	44,935	365	730	0.5	trough	70	1.39	no	0.94	no	1,000			
		23-DEN	63,895	477	1,230	0.9	trough	23	0.85	no	0.26	no	1,000			
		24-DEN	56,565	426	1,990	1.5	trough	14	3.3	no	1.43	no	1,000			
		25-DEN	51,740	397	1,340	1.0	trough	9.3	4.0	no	2.22	no	1,000			
		26-DEN	45,820	379	2,480	1.8	trough	8.9	4.7	no	2.88	no	1,000			
		27-DEN	40,165	369	330	0.2	trough	8.6	5.2	no	3.46	no	1,000			
		8-GJT	27,470	327	1,060	0.8	crest	14	5.4	no	2.8	no	1,050			
	3	9-GJT	26,615	317	650	0.5	crest	3.6	1.7	no	0.96	no	1,050			
		10-GJT	27,145	321	1,710	1.2	crest	6.7	2.9	no	1.6	no	1,050			
		14-RLG	26,700	328	1,400	1.0	crest	2.0	1.44	no	1.12	no	1,050			
		15-RLG	25,875	320	250	0.2	crest	2.4	2.33	no	1.37	no	1,050			
		28-DEN	28,445	329	1,310	1.0	crest	1.3	0.99	no	0.79	no	1,050			
		29-DEN	27,245	320	1,090	0.8	crest	2.3	1.41	no	0.95	no	1,050			
		30-DEN	27,900	323	2,400	1.8	crest	1.7	1.23	no	0.92	no	1,050			
		13-RLG	24,775	315	5,250	3.8	crest	1.8	1.28	no	0.98	no	1,050			
		16-RLG	25,200	316	1,100	0.8	crest	0.6	0.52	no	0.45	no	1,050			
		17-RLG	24,125	309	1,050	0.8	crest	0.5	0.42	no	0.34	no	1,050			
	4	11-GJT	23,255	299	690	0.5	crest	0.04	0.03	yes	0.03	yes	1,350			
		18-RLG	22,875	303	1,450	1.1	crest	1.5	0.95	no	0.66	no	1,350			
		19-RLG	19,550	293	900	0.7	crest	4.9	1.36	no	0.62	no	1,350			
		31-DEN	22,410	299	780	0.6	crest	0.35	0.23	yes	0.16	yes	1,350			
5	8-GJT	27,470	327	1,060	0.8	crest	14	5.4	no	2.8	no	1,050				
	9-GJT	26,615	317	650	0.5	crest	3.6	1.7	no	0.96	no	1,050				
	10-GJT	27,145	321	1,710	1.2	crest	6.7	2.9	no	1.6	no	1,050				
TEST 198, RUN 9	1-AMA*	55,600	418	1,400	1.0	trough	9.5	NA	NA	NA	NA	yes	0.6-0.9 1.0-1.6 0.4-0.6		1,050	
	RUN 12	2-AMA*	54,000	401	1,450	1.0	trough	4.5								
	RUN 13	3-AMA*	54,600	406	2,850	2.0	trough	7.0								
TEST 202, RUN 8	1-OKC*	61,100	450	1,800	1.3	crest	2.5	0.19	yes	0.07	yes	yes	{ 0.4-4.0	{ crest	1,300	
	2-OKC*	57,250	418	2,100	1.5	trough	1.73	0.22	yes	0.08	yes					1,300
TEST 233, RUN 3	1-MBHC*	54,850	396.5	1,700	1.2	crest	0.27	NA	NA	NA	NA	yes	{ 1.6-3.7			
	2-MBHC*	52,250	376	1,300	1.0	trough	5.2									
	3-MBHC*	53,700	377	4,000	2.9	trough	5.5									

* Temperatures from rawinsonde at indicated station and winds from aircraft data

** a is assumed amplitude based on nearest isentrope

*** Rawinsonde Stations UCC-Yucca Flats, DEN-Denver, ABQ-Albuquerque, GBY-Granby, GJT-Grand Junction, RLG-Kremmling, AMA-Amarillo, OKC-Oklahoma City, and MBHC-Howard Air Force Base (Panama)

COMPARISON OF WATER CHANNEL RESULTS FOR HYPERBOLIC TANGENT VELOCITY PROFILES WITH DRAZIN'S CRITERION FOR STABILITY

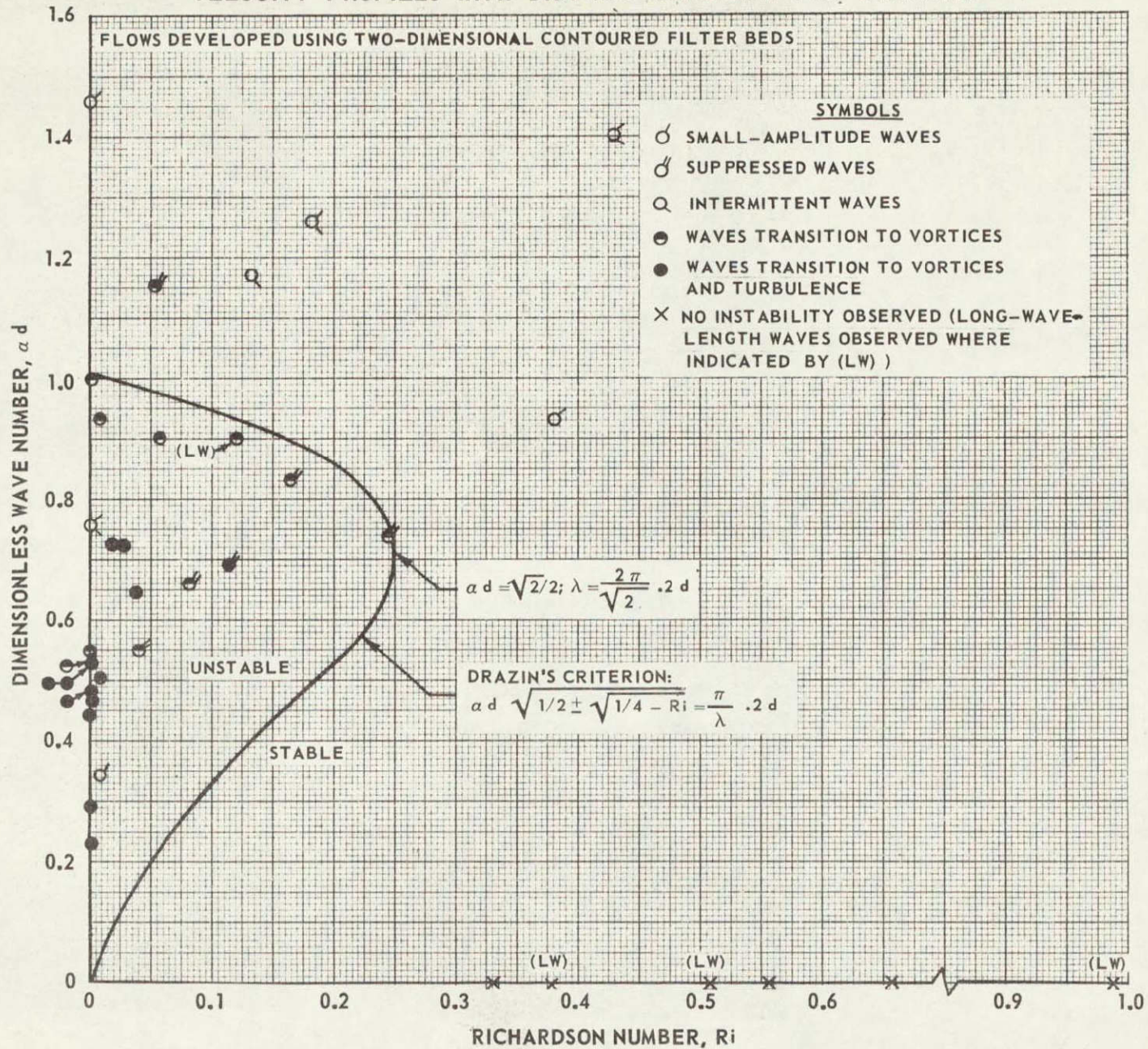
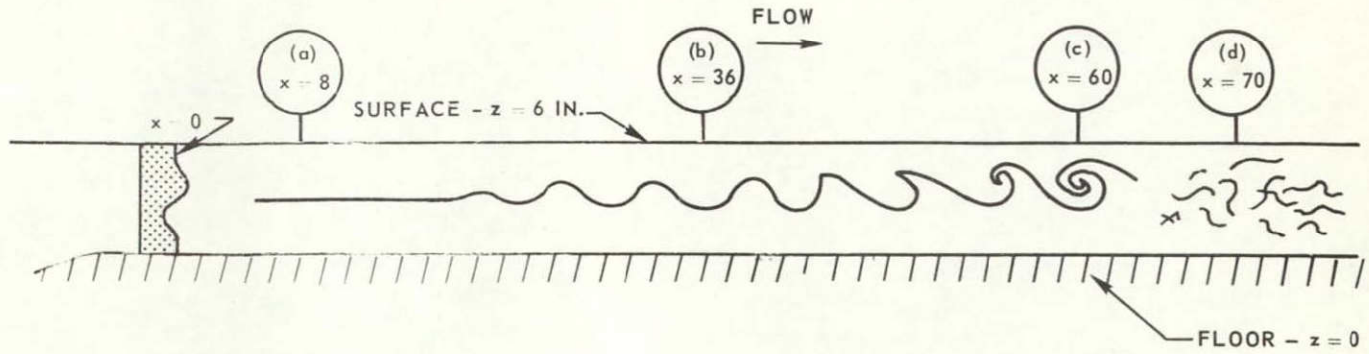


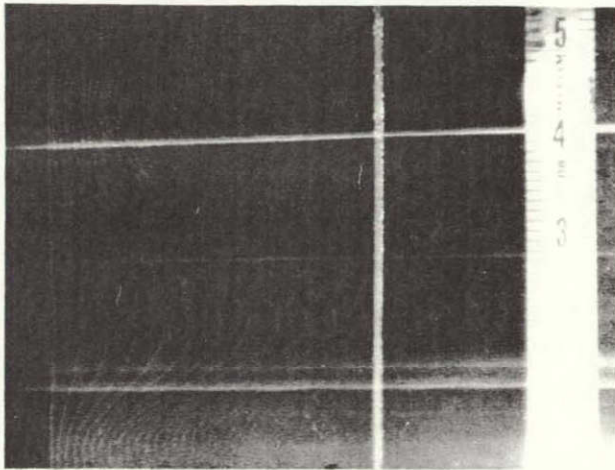
FIG. 1

TYPICAL STAGES OF BREAKDOWN OF FLOW IN SHEAR LAYERS HAVING
 "S-SHAPED" VELOCITY PROFILES

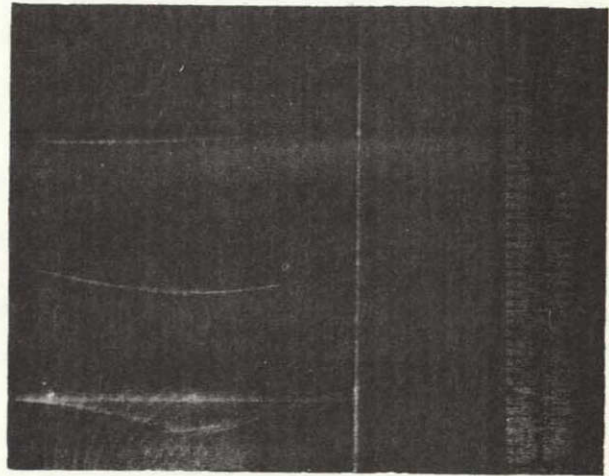
$V_0 = 0.07 \text{ FT/SEC}$ $(\partial V/\partial z)_0 = -0.80 \text{ SEC}^{-1}$ $(\partial T/\partial z)_0 = 0$



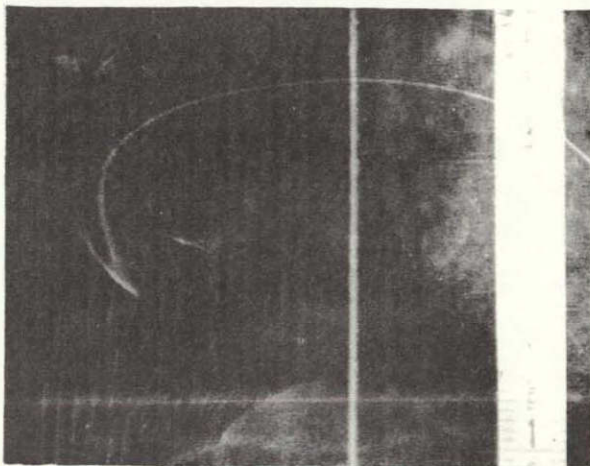
(a) x = 8 IN. - UNDISTURBED



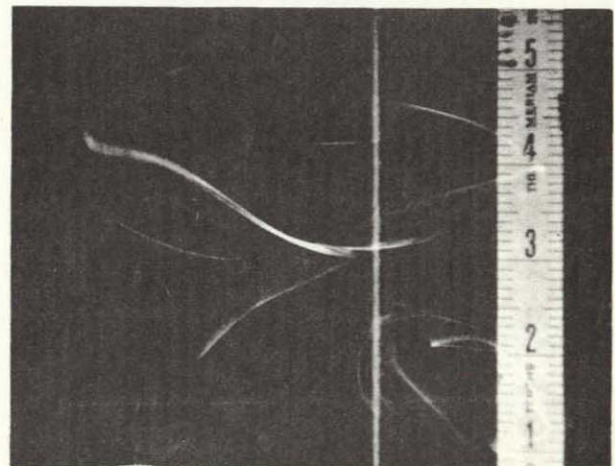
(b) x = 36 IN. - WAVES



(c) x = 60 IN. - VORTICES

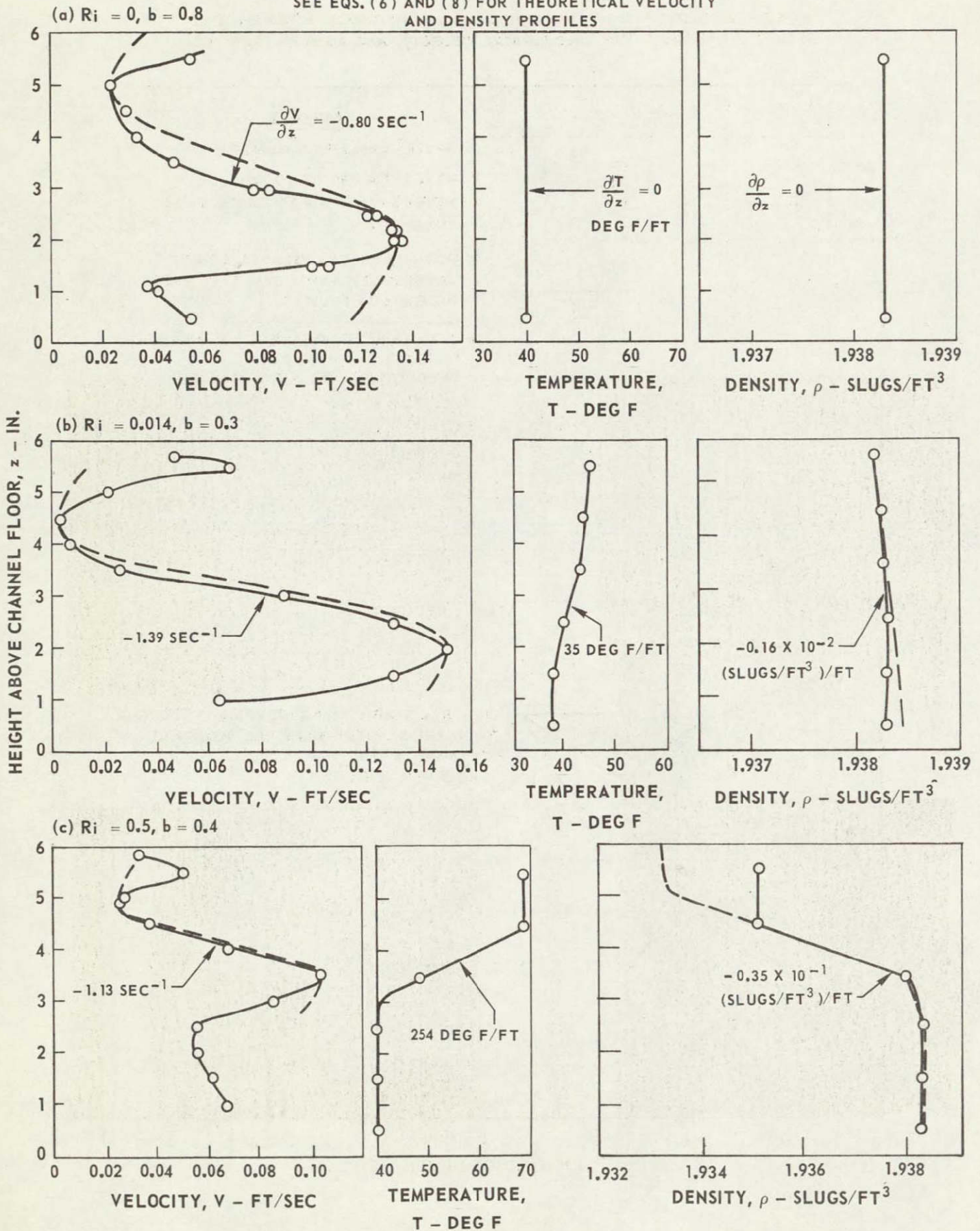


(d) x = 70 IN. - TURBULENCE



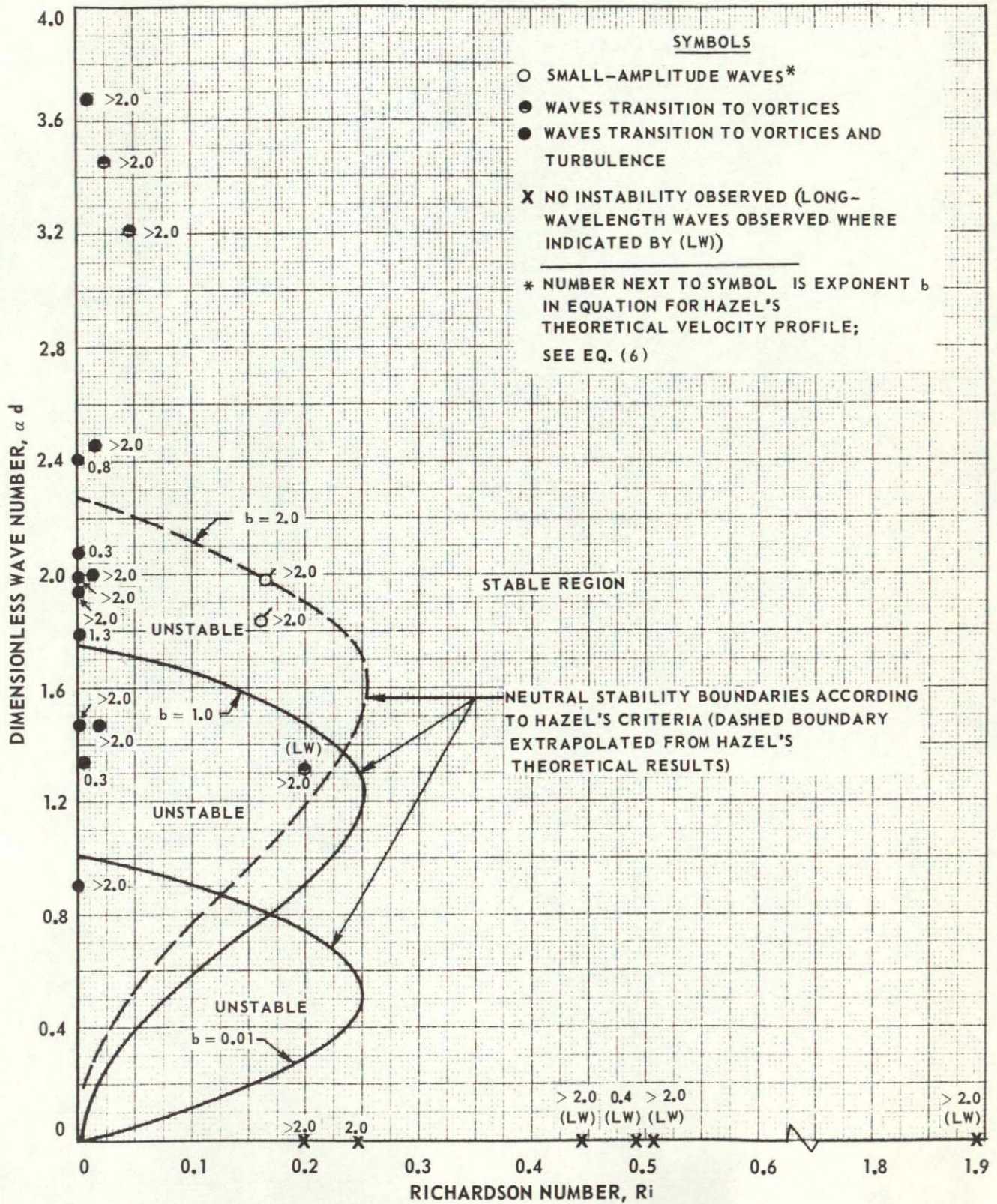
TYPICAL "S" VELOCITY, TEMPERATURE AND DENSITY PROFILES FOR SHEAR-FLOW EXPERIMENTS IN WATER CHANNEL

— CORRESPONDING PROFILE IN HAZEL'S THEORY
 SEE EQS. (6) AND (8) FOR THEORETICAL VELOCITY AND DENSITY PROFILES



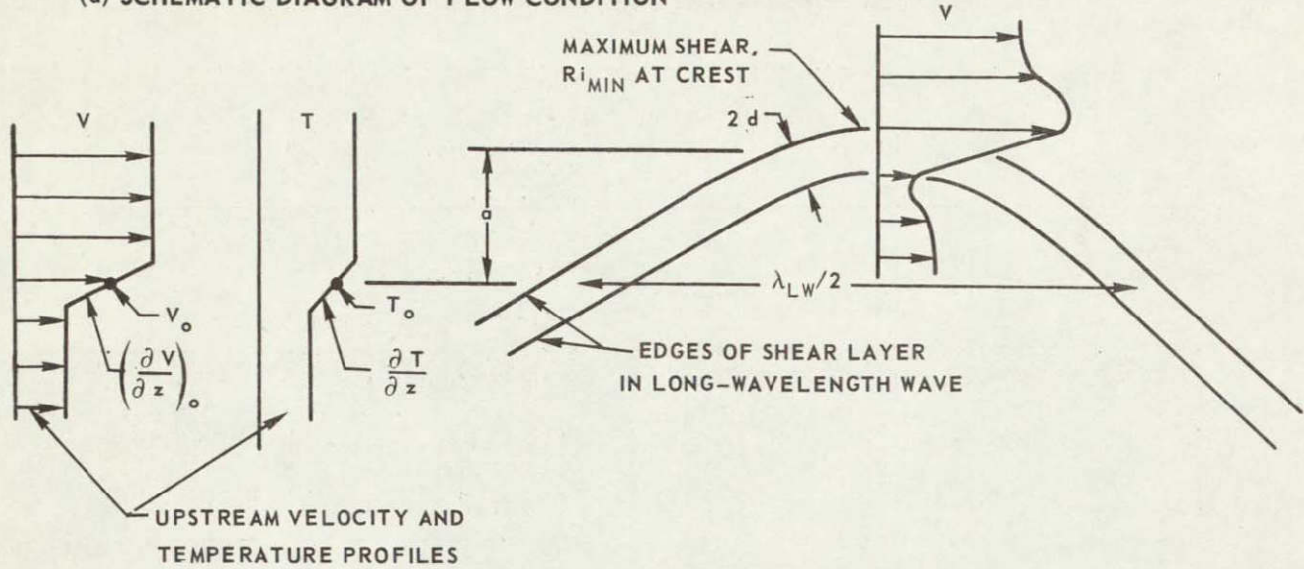
COMPARISON OF WATER CHANNEL RESULTS FOR "S-SHAPED" VELOCITY PROFILES WITH HAZEL'S CRITERIA FOR STABILITY

FLOW DEVELOPED USING TWO-DIMENSIONAL CONTOURED FILTER BEDS
 SEE EQS. (6) AND (8) FOR THEORETICAL VELOCITY AND DENSITY PROFILES

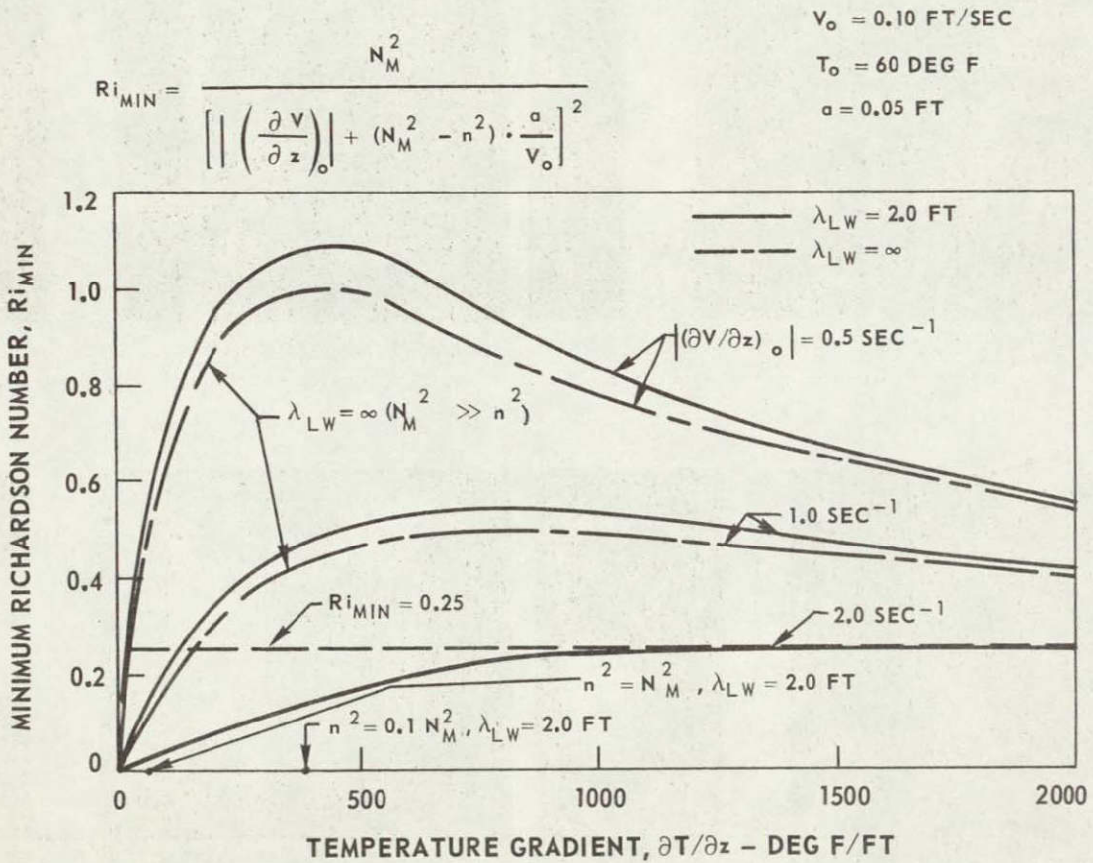


EFFECT OF A LONG-WAVELENGTH WAVE ON THE MINIMUM RICHARDSON NUMBER IN A SHEAR FLOW

(a) SCHEMATIC DIAGRAM OF FLOW CONDITION



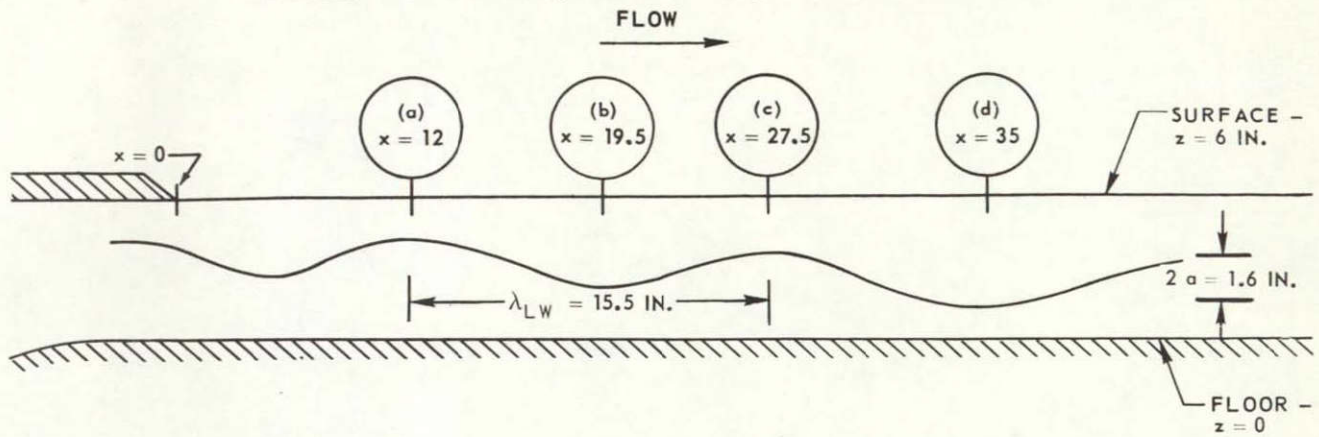
(b) EFFECT OF TEMPERATURE GRADIENT AND INITIAL SHEAR ON Ri_{MIN} IN WATER



WATER CHANNEL RESULTS SHOWING EFFECT OF A LONG-WAVELENGTH WAVE ON THE LOCAL RICHARDSON NUMBER IN A SHEAR FLOW

$V_o = 0.04 \text{ FT/SEC}$ $Ri_o = 2.5$ $(\partial V/\partial z)_o = 0.26 \text{ SEC}^{-1}$

SEE FIG. 7 FOR VELOCITY, TEMPERATURE, AND DENSITY PROFILES

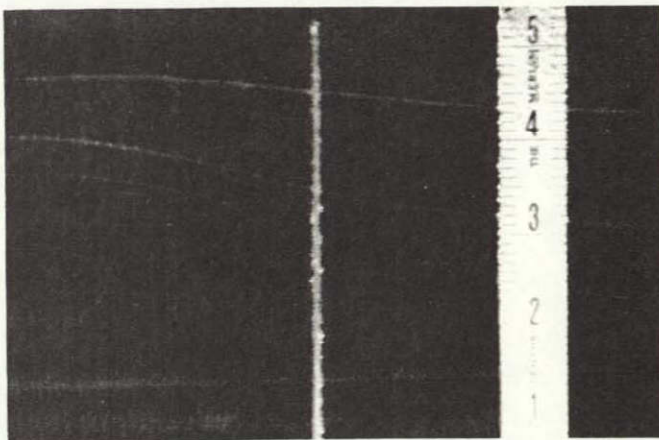


(a) x = 12 IN. - CREST

$\partial V/\partial z = 0.42 \text{ SEC}^{-1}$, $\partial T/\partial z = 90 \text{ DEG F/FT}$, $Ri = 1$

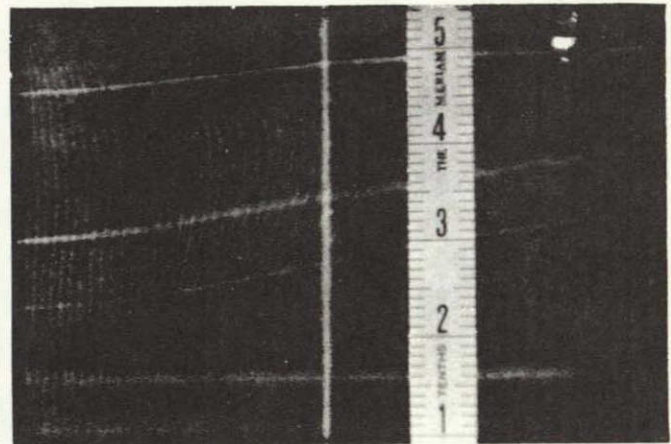
(b) x = 19.5 IN. - TROUGH

$\partial V/\partial z = 0.11 \text{ SEC}^{-1}$, $\partial T/\partial z = 105 \text{ DEG F/FT}$, $Ri = 14$



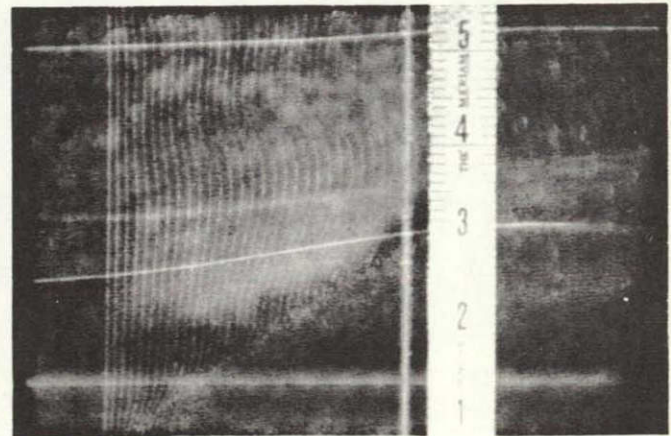
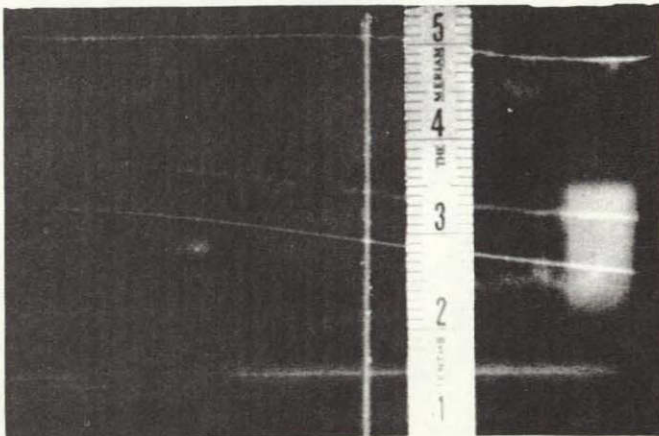
(c) x = 27.5 IN. - CREST

$\partial V/\partial z = 0.24 \text{ SEC}^{-1}$, $\partial T/\partial z = 97.5 \text{ DEG F/FT}$, $Ri = 3$



(d) x = 35 IN. - TROUGH

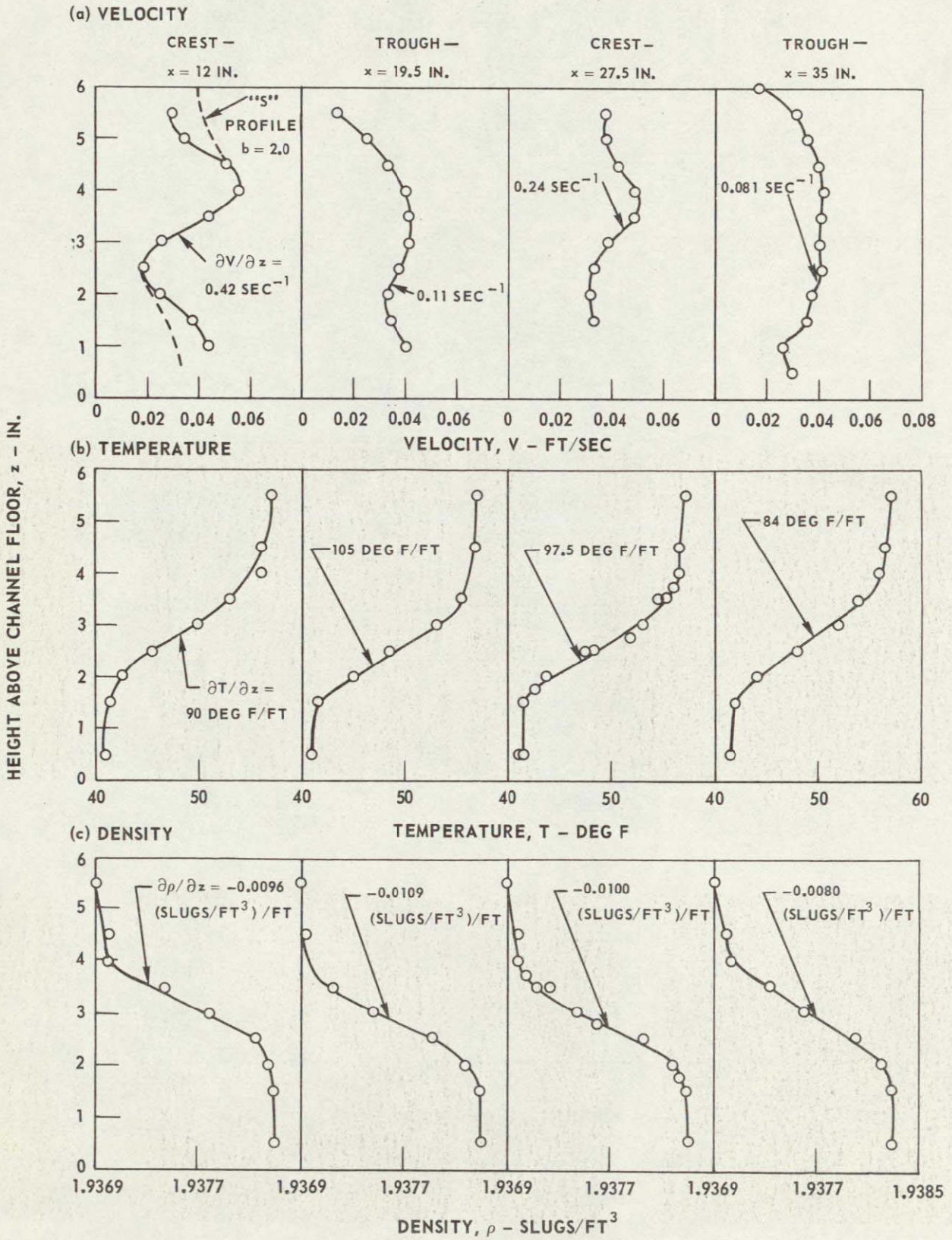
$\partial V/\partial z = 0.08 \text{ SEC}^{-1}$, $\partial T/\partial z = 84 \text{ DEG F/FT}$, $Ri = 27$



TYPICAL VELOCITY, TEMPERATURE AND DENSITY PROFILES FOR FLOW IN A LONG-WAVELENGTH WAVE

SEE FIG. 6 FOR PHOTOGRAPHS OF FLOW

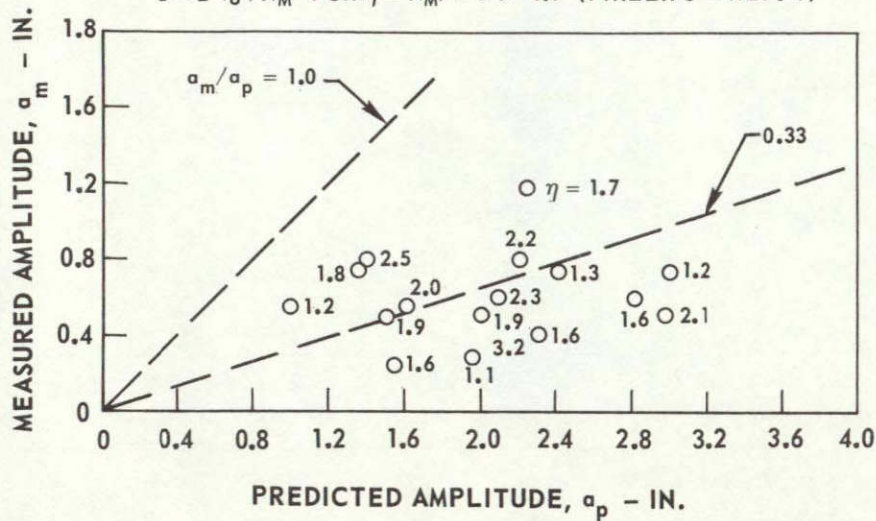
$V_0 = 0.04 \text{ FT/SEC}$, $(\partial V/\partial z)_0 = 0.26 \text{ SEC}^{-1}$, $\lambda_{LW} = 15.5 \text{ IN.}$, $\alpha = 0.8 \text{ IN.}$



COMPARISON BETWEEN MEASURED AND PREDICTED VALUES OF
AMPLITUDE AND WAVELENGTH OF LONG-WAVELENGTH WAVES
DATA FROM UARL OPEN WATER CHANNEL

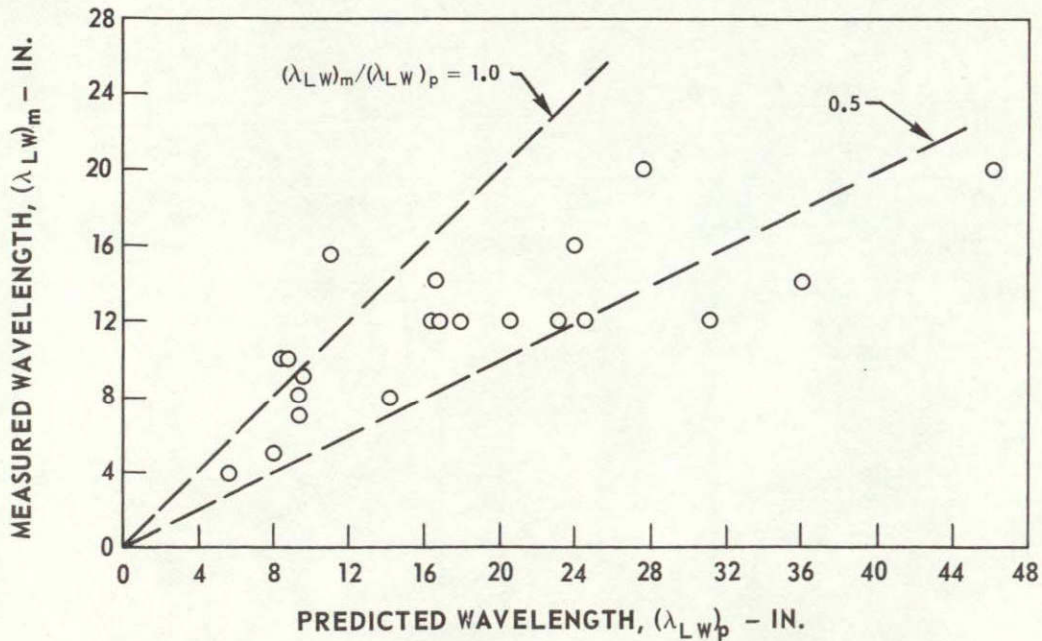
(a) AMPLITUDE

$$a = 2 V_o / N_M \text{ FOR } \eta = N_M / n \gg 1.0 \text{ (PHILLIPS - REF. 4)}$$



(b) WAVELENGTH

$$\lambda_{LW} = \frac{2\pi}{g} \frac{\rho_2 v_2^2}{(\rho_2 - \rho_1)} \left[\left(\frac{v_1}{v_2} \right)^2 \frac{\rho_1}{\rho_2} + 1 \right] \text{ (HAURWITZ - REF. 5)}$$



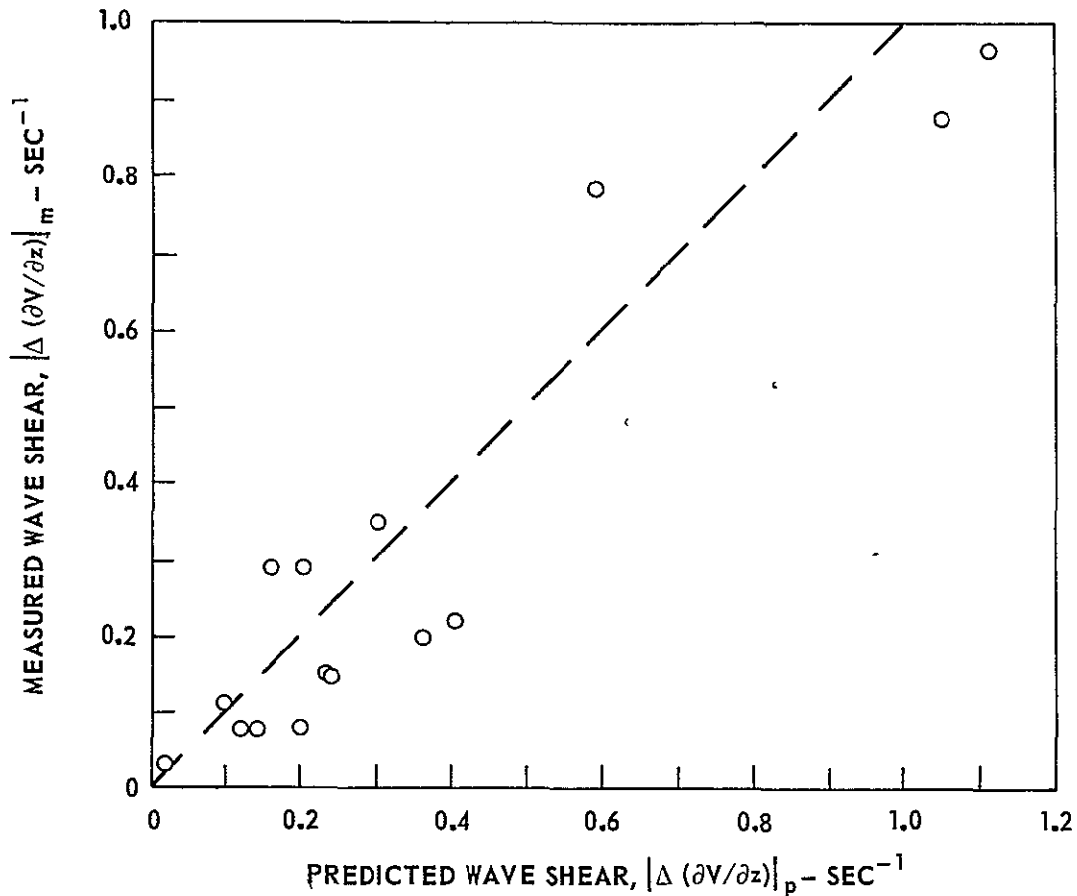
COMPARISON BETWEEN MEASURED AND PREDICTED VALUES OF WAVE SHEAR IN A LONG-WAVELENGTH WAVE

SHEAR PREDICTED USING PHILLIPS' THEORY (REF. 4)

$$\left| \Delta (\partial V / \partial z) \right| = (a / V_0) (N_M^2 - n^2)$$

MEASURED WAVE SHEAR GENERALLY BASED ON FIRST HALF WAVELENGTH
OF LONG-WAVELENGTH WAVE

DATA FROM UARL OPEN WATER CHANNEL



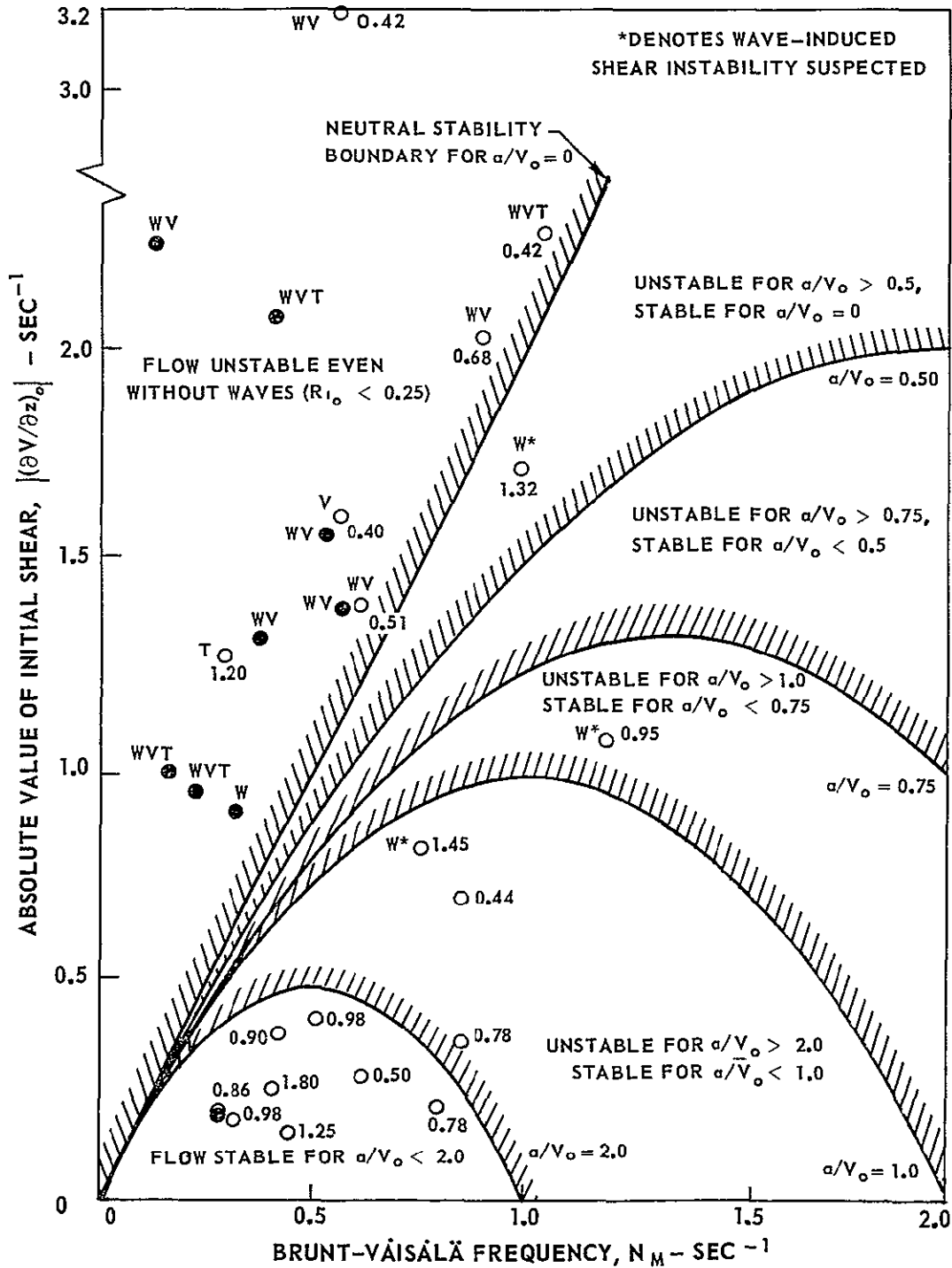
EFFECT OF WAVE AMPLITUDE RATIO ON STABILITY BOUNDARIES FOR SHEAR FLOWS IN LONG-WAVELENGTH WAVES

DATA FROM UARL OPEN WATER CHANNEL

SYMBOL	LONG-WAVELENGTH WAVE OBSERVED?
○ α/V_0	YES
● α/V_0	NO

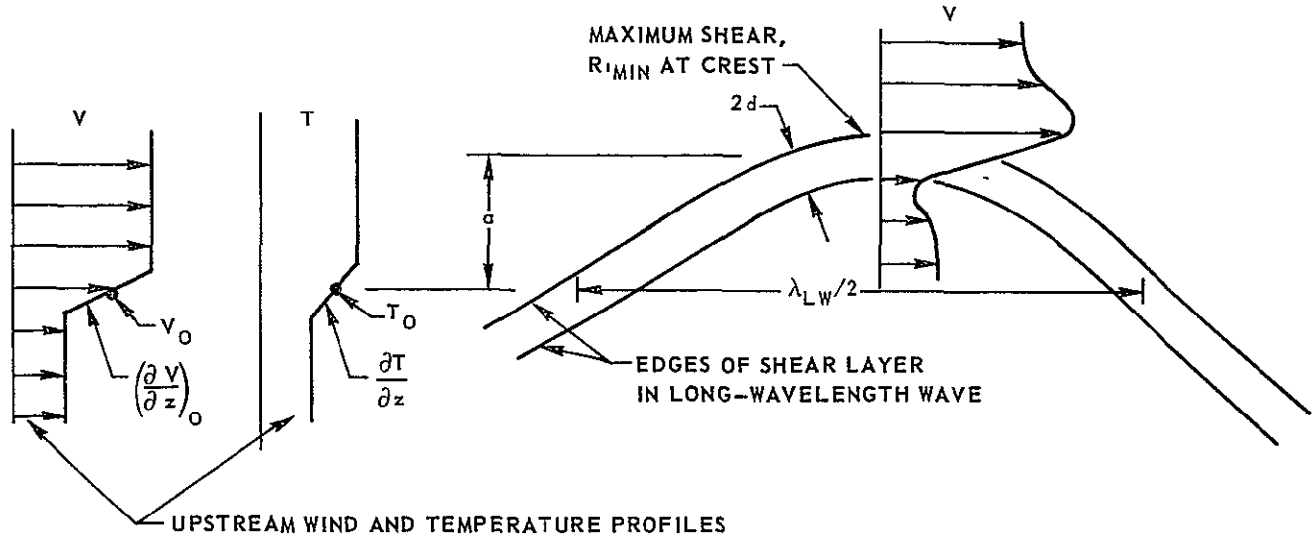
LET-TER	INSTABILITY OBSERVED
W	WAVES
V	VORTICES
T	TURBULENCE

$$\Delta \left(\frac{\partial V}{\partial z} \right) = N_M^2 \left(\frac{a}{V_0} \right)$$

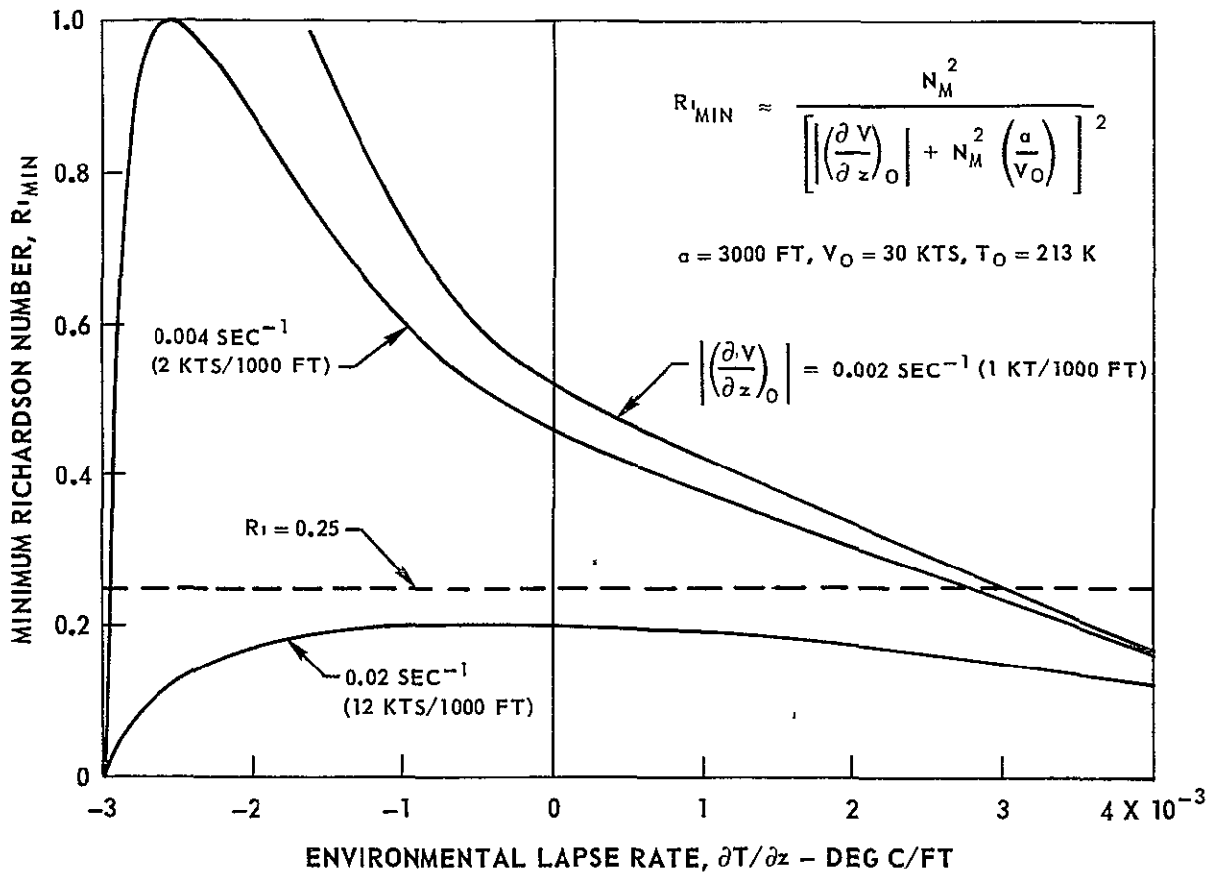


EFFECTS OF LONG-WAVELENGTH WAVES ON STABILITY OF ATMOSPHERIC SHEAR LAYERS

(a) SCHEMATIC DIAGRAM OF FLOW CONDITION

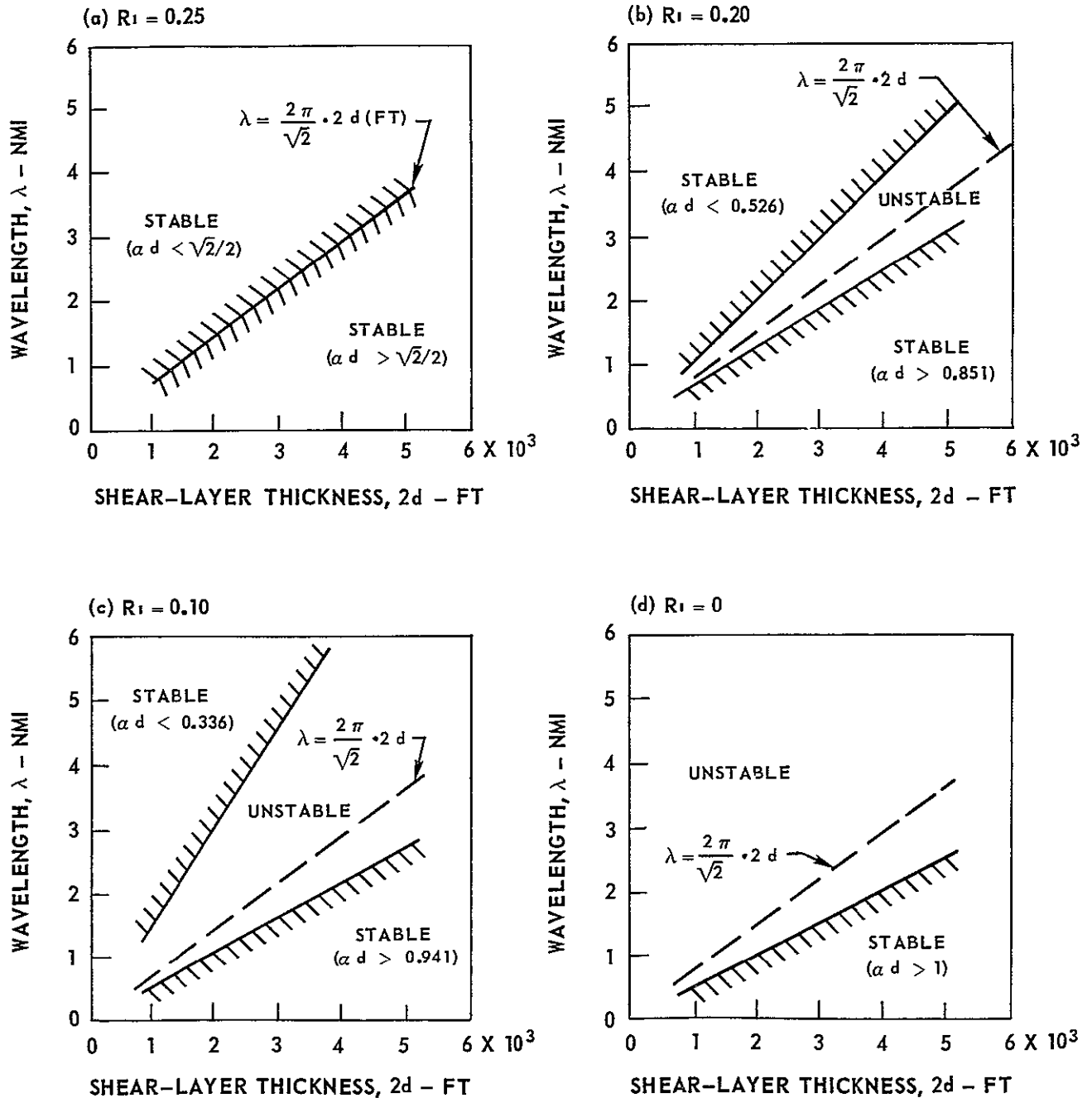


(b) EFFECT OF LAPSE RATE AND SHEAR ON R'_{MIN} FOR TYPICAL WAVE CONDITIONS




PREDICTION OF UNSTABLE WAVELENGTHS IN ATMOSPHERIC SHEAR LAYERS USING DRAZIN'S CRITERION

$$\text{UNSTABLE RANGE} \cdot \sqrt{1/2 - \sqrt{1/4 - R_i}} < \alpha d = \frac{\pi}{\lambda} \cdot 2d < \sqrt{1/2 + \sqrt{1/4 - R_i}}$$



ISENTROPE FOR PROJECT HICAT TEST 264, RUN 16

CAT ASSOCIATED WITH LEE WAVES
2323 GMT NOVEMBER 30, 1967
AIRCRAFT HEADING APPROXIMATELY 20-70 DEG TO WIND
— ISENTROPE FLIGHT PATH  TURBULENCE REPORTED
SEE FIG. 14 FOR WIND AND TEMPERATURE PROFILES

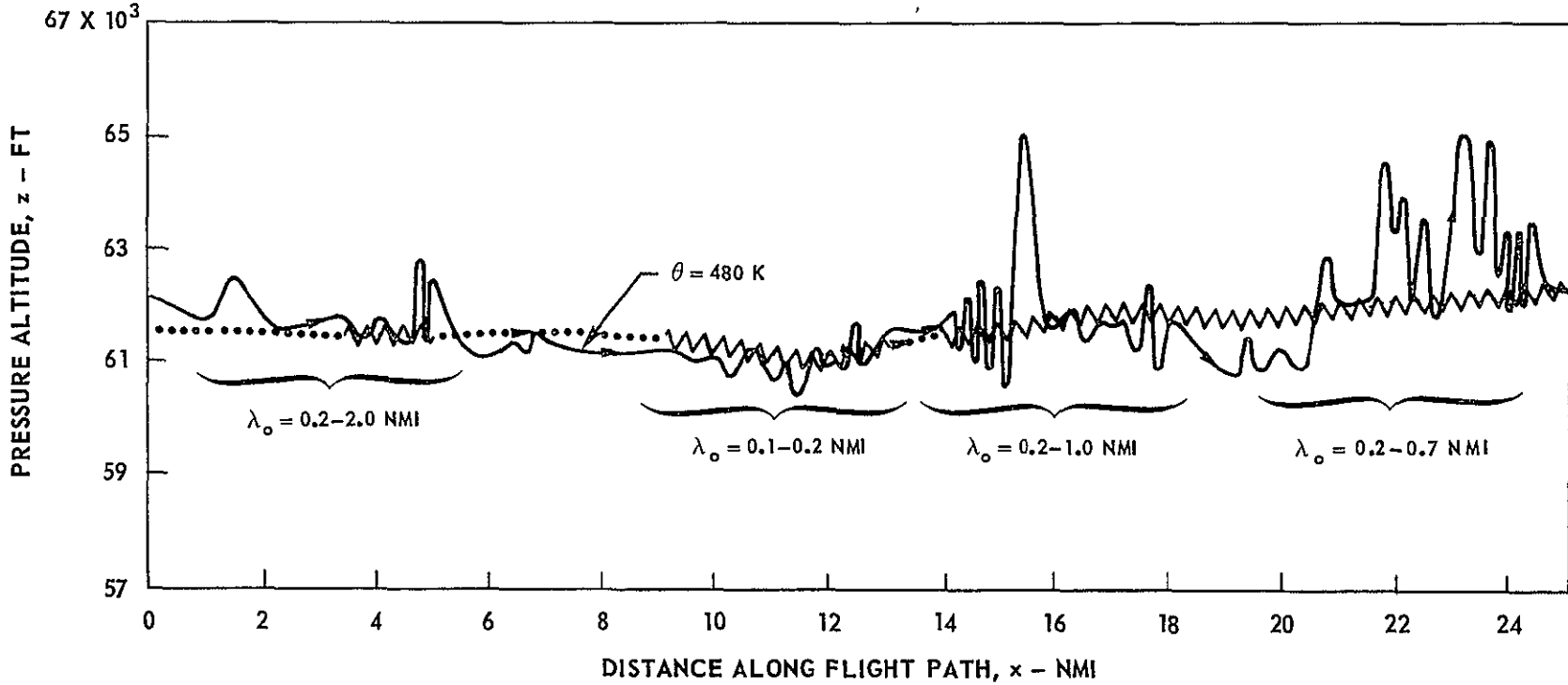


FIG. 13

WIND AND TEMPERATURE PROFILES FOR PROJECT HICAT TEST 264, RUN 16

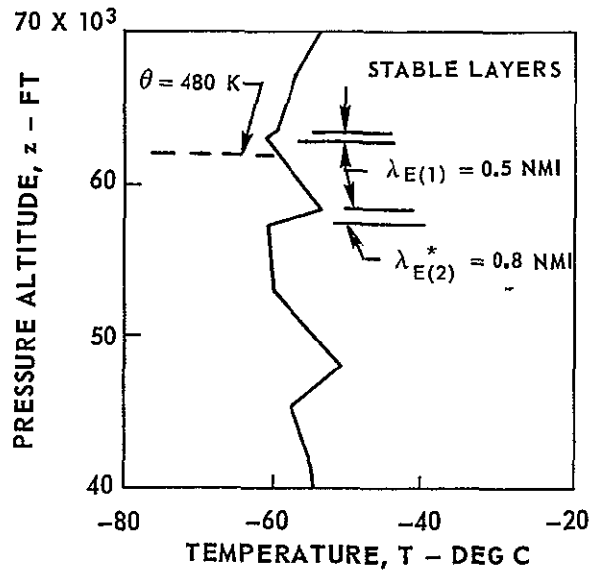
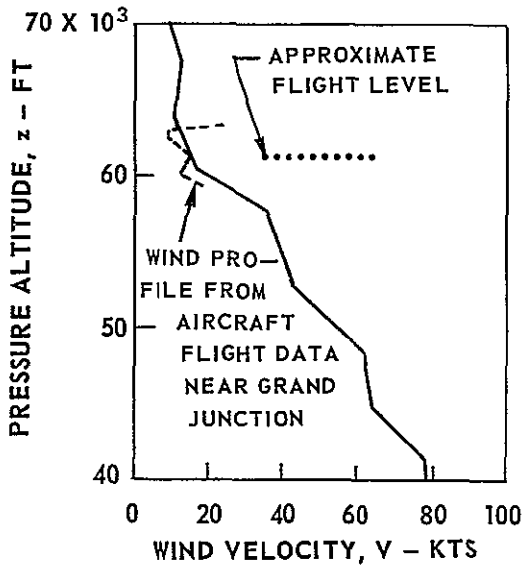
0000 GMT, DECEMBER 1, 1967
 PROFILES FROM RAWINSONDE DATA

$$\lambda_E = (2\pi/\sqrt{2}) \cdot 2d$$

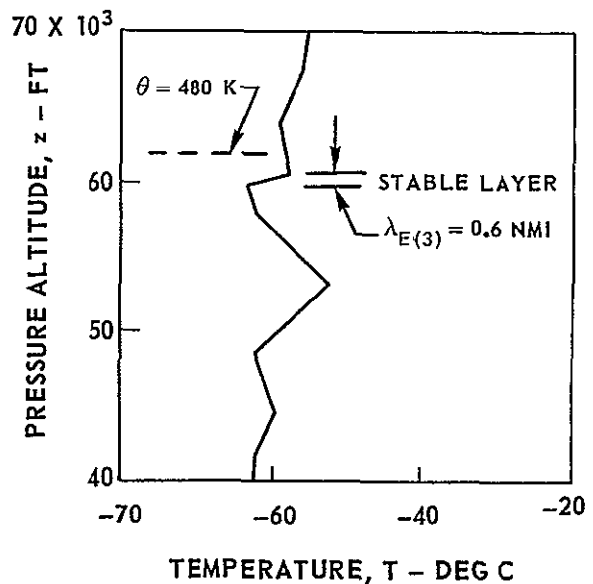
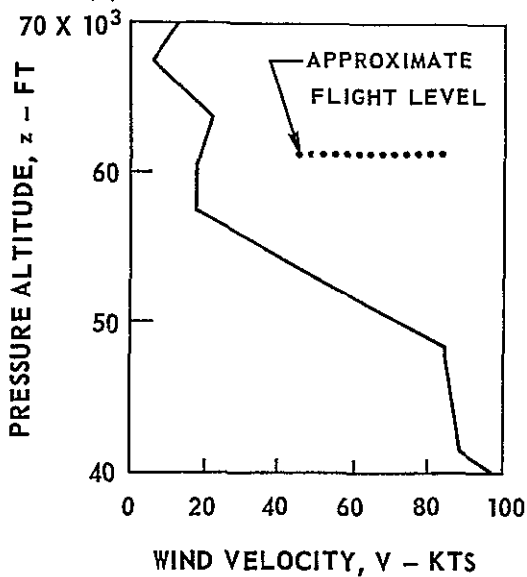
λ_E^* DENOTES WAVES UNLIKELY TO OCCUR

SEE TABLE I FOR ADDITIONAL DETAILS

(a) YUCCA FLATS



(b) DENVER



ISENTROPES FOR PROJECT HICAT TEST 267, RUNS 8, 9, AND 28

CAT ASSOCIATED WITH LEE WAVES

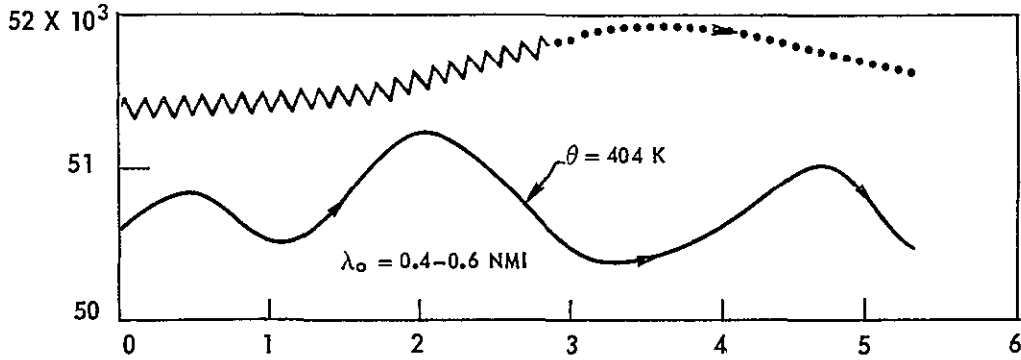
DECEMBER 1, 1967

— ISENTROPE ••• FLIGHT PATH ∇ TURBULENCE REPORTED

SEE FIG. 16 FOR WIND AND TEMPERATURE PROFILES

(a) RUN 8 (0328 GMT)

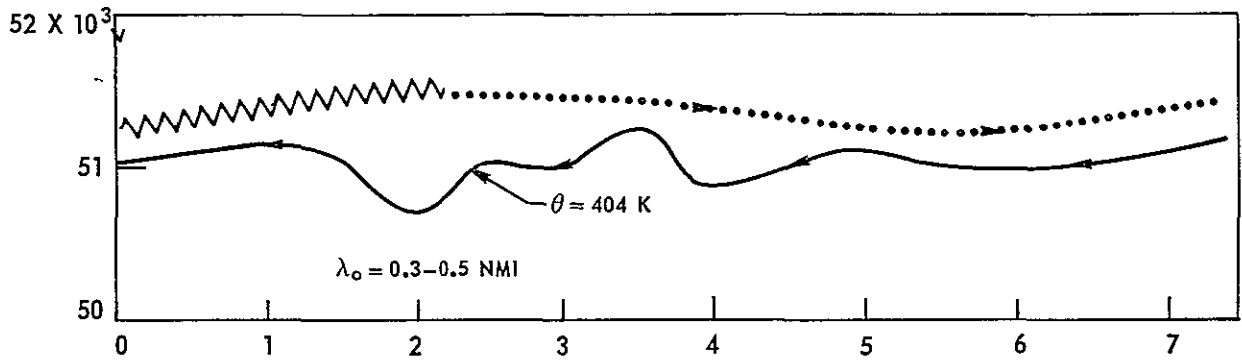
AIRCRAFT HEADING APPROXIMATELY 75 DEG TO WIND



(b) RUN 9 (0333 GMT)

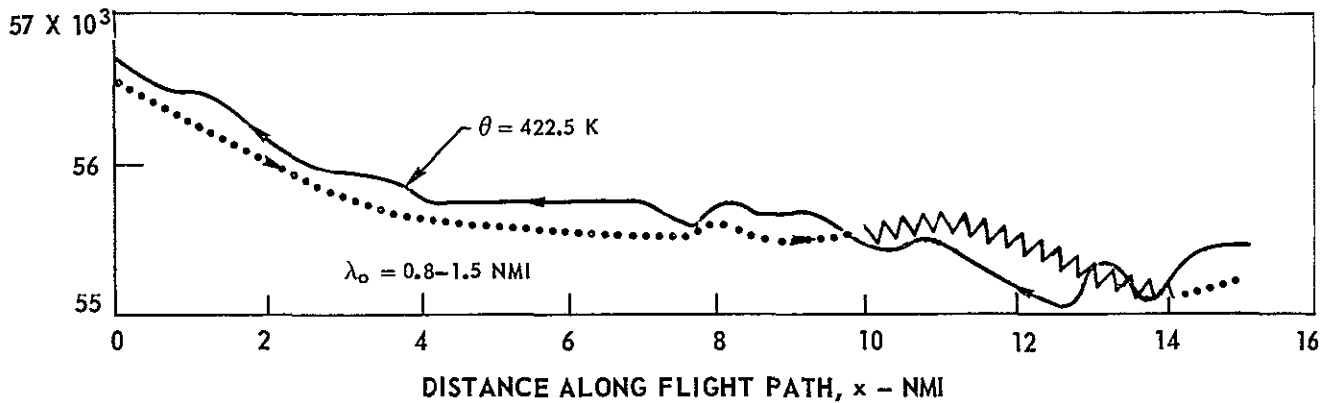
AIRCRAFT HEADING APPROXIMATELY 105 DEG TO WIND

PRESSURE ALTITUDE, z - FT



(c) RUN 28 (0453 GMT)

AIRCRAFT HEADING APPROXIMATELY 135 DEG TO WIND



WIND AND TEMPERATURE PROFILES FOR PROJECT HICAT TEST 267, RUNS 8, 9, AND 28

DECEMBER 1, 1967

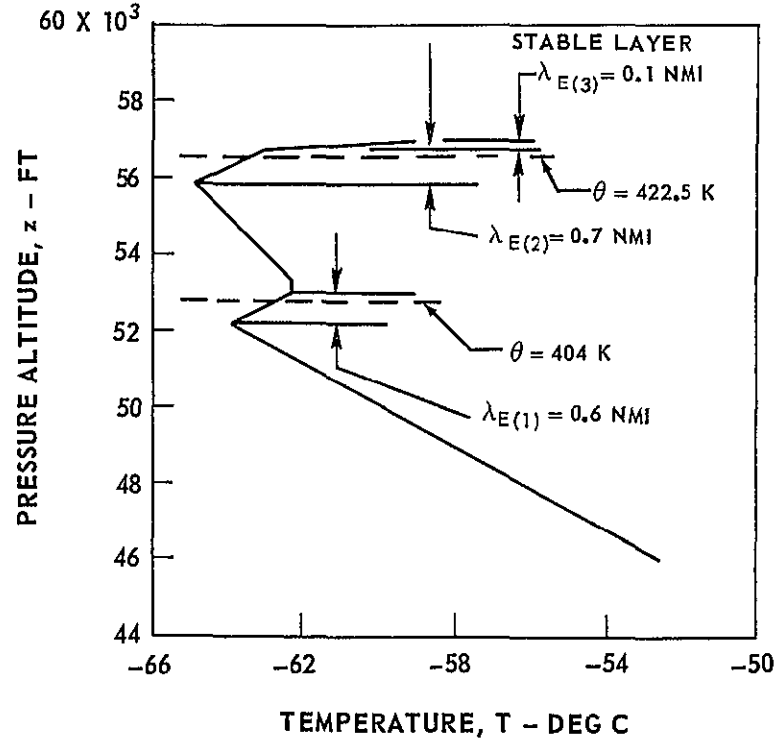
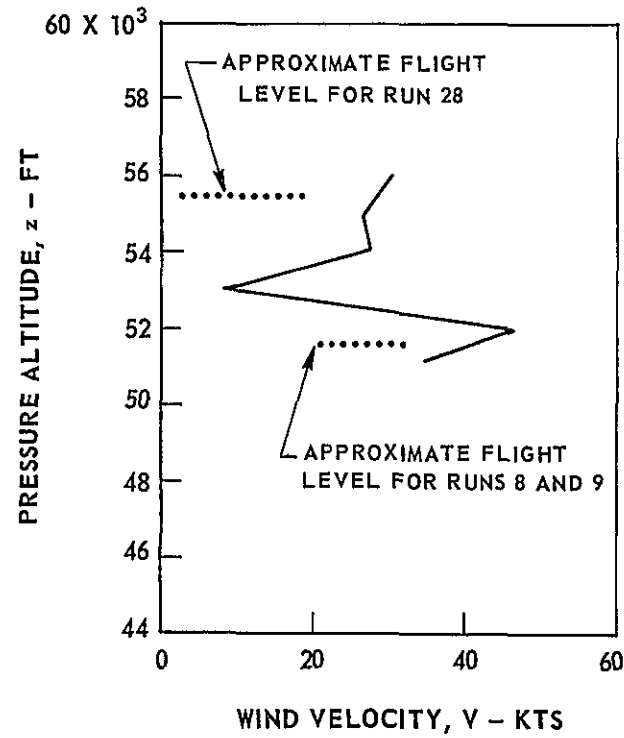
PROFILES ARE COMPOSITES OF AIRCRAFT AND RAWINSONDE DATA

$$\lambda_E = (2\pi/\sqrt{2}) \cdot 2d$$

SEE TABLE I FOR ADDITIONAL DETAILS

(a) WIND - FLIGHT DATA (0312-0545 GMT)

(b) TEMPERATURE - ALBUQUERQUE RADIOSONDE (2400 GMT)



ISENTROPE FOR PROJECT HICAT TEST 282, RUN 2

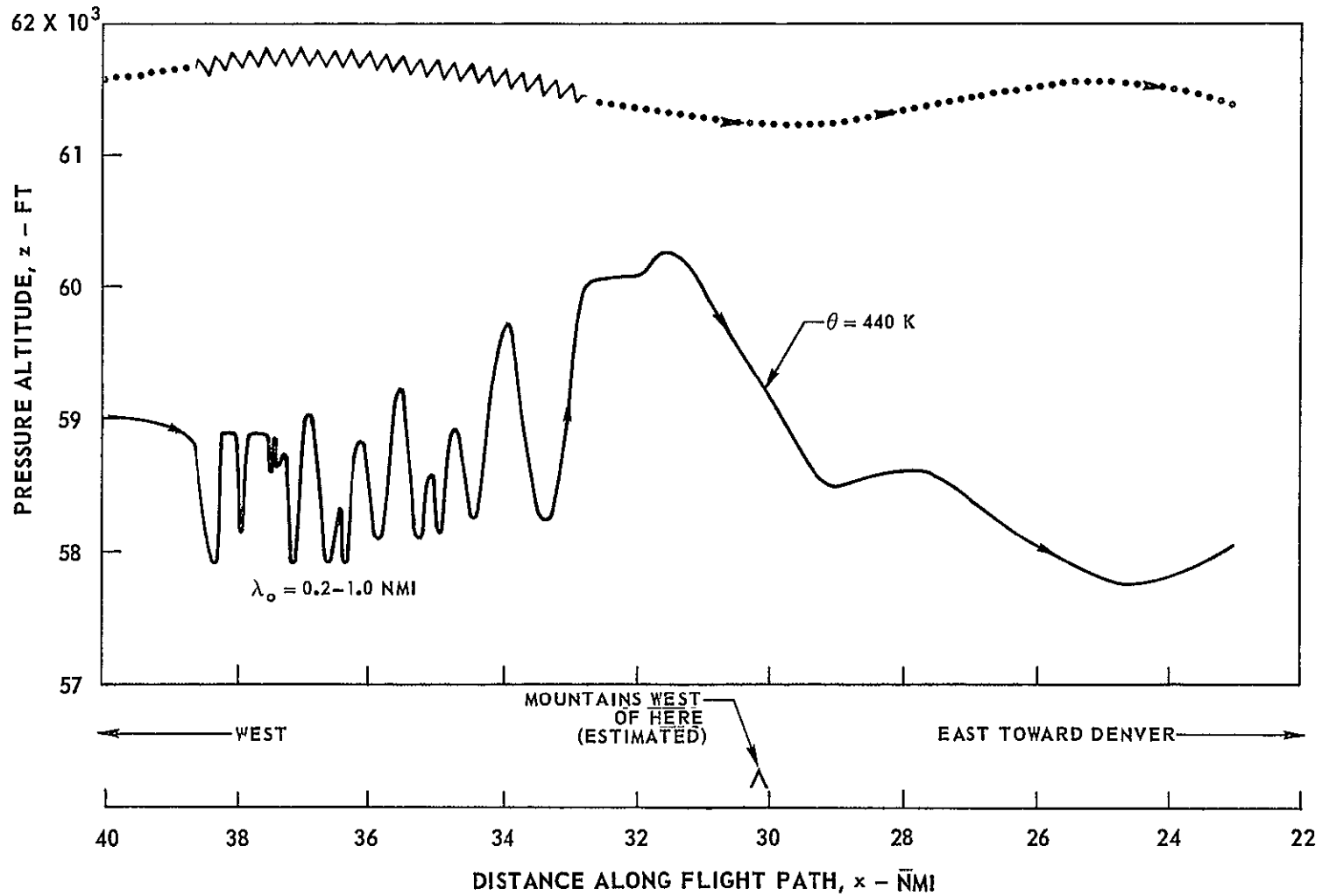
CAT ASSOCIATED WITH LEE WAVES

2212 GMT FEBRUARY 19, 1968

AIRCRAFT HEADING APPROXIMATELY 22 DEG TO WIND

———— ISENTROPE FLIGHT PATH ~~~~~ TURBULENCE REPORTED

SEE FIG 18 FOR WIND AND TEMPERATURE PROFILES



WIND AND TEMPERATURE PROFILES FOR PROJECT HICAT TEST 282, RUN 2

J910563-14

BASED ON DATA FROM DR. D.K. LILLY OF NCAR
 GRANBY 2000 GMT, FEBRUARY 19, 1963
 PROFILES FROM RAWINSONDE DATA

$\lambda_E = (2\pi/\sqrt{2}) 2d$ λ_E^* DENOTES WAVES UNLIKELY TO OCCUR
 SEE TABLE I FOR ADDITIONAL DETAILS

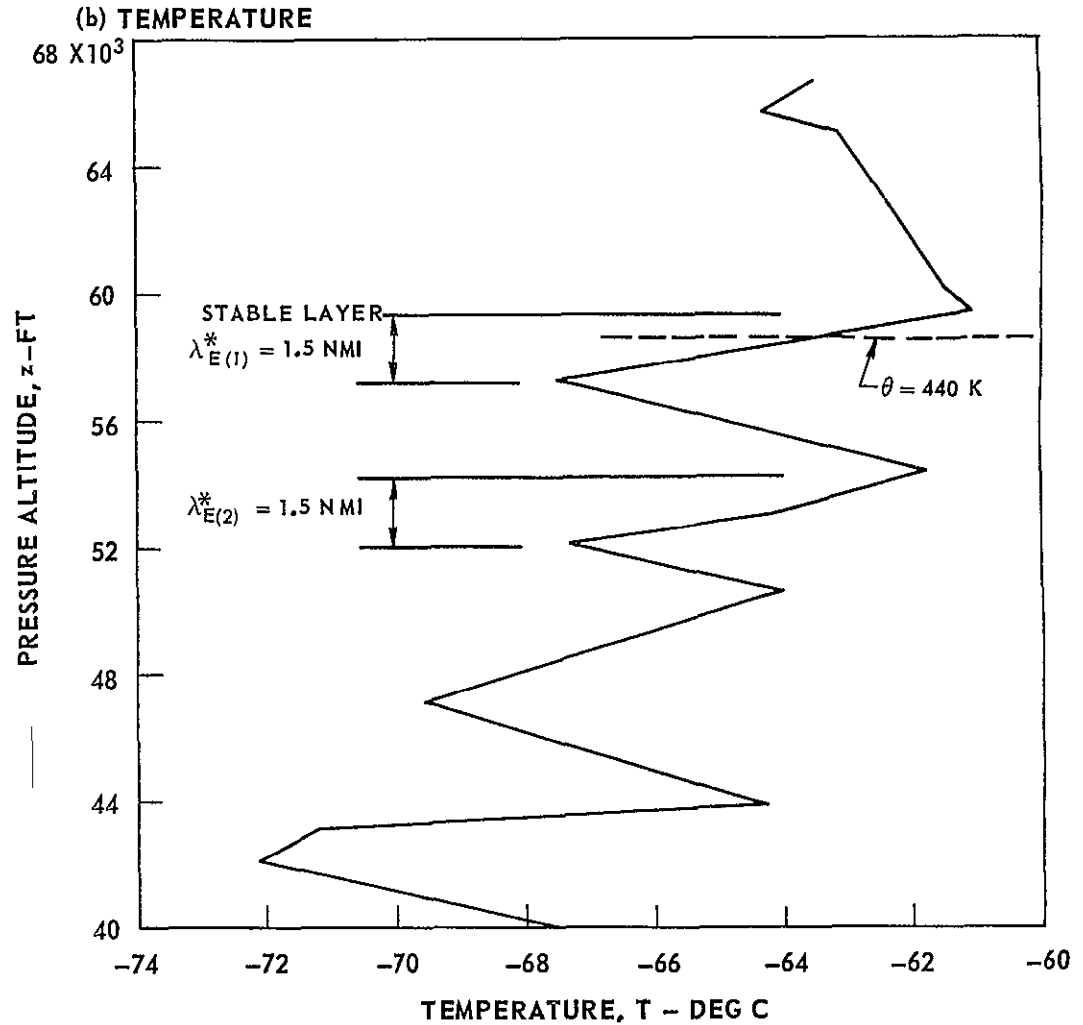
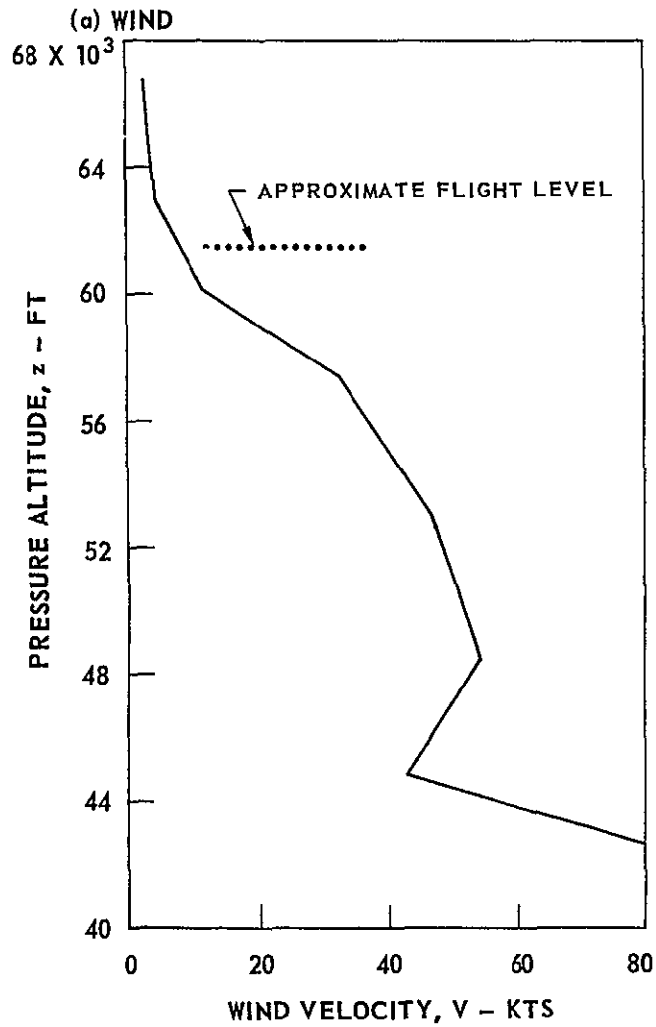


FIG. 18

ISENTROPES FOR COLORADO LEE WAVE CASE OF FEBRUARY 13, 1970

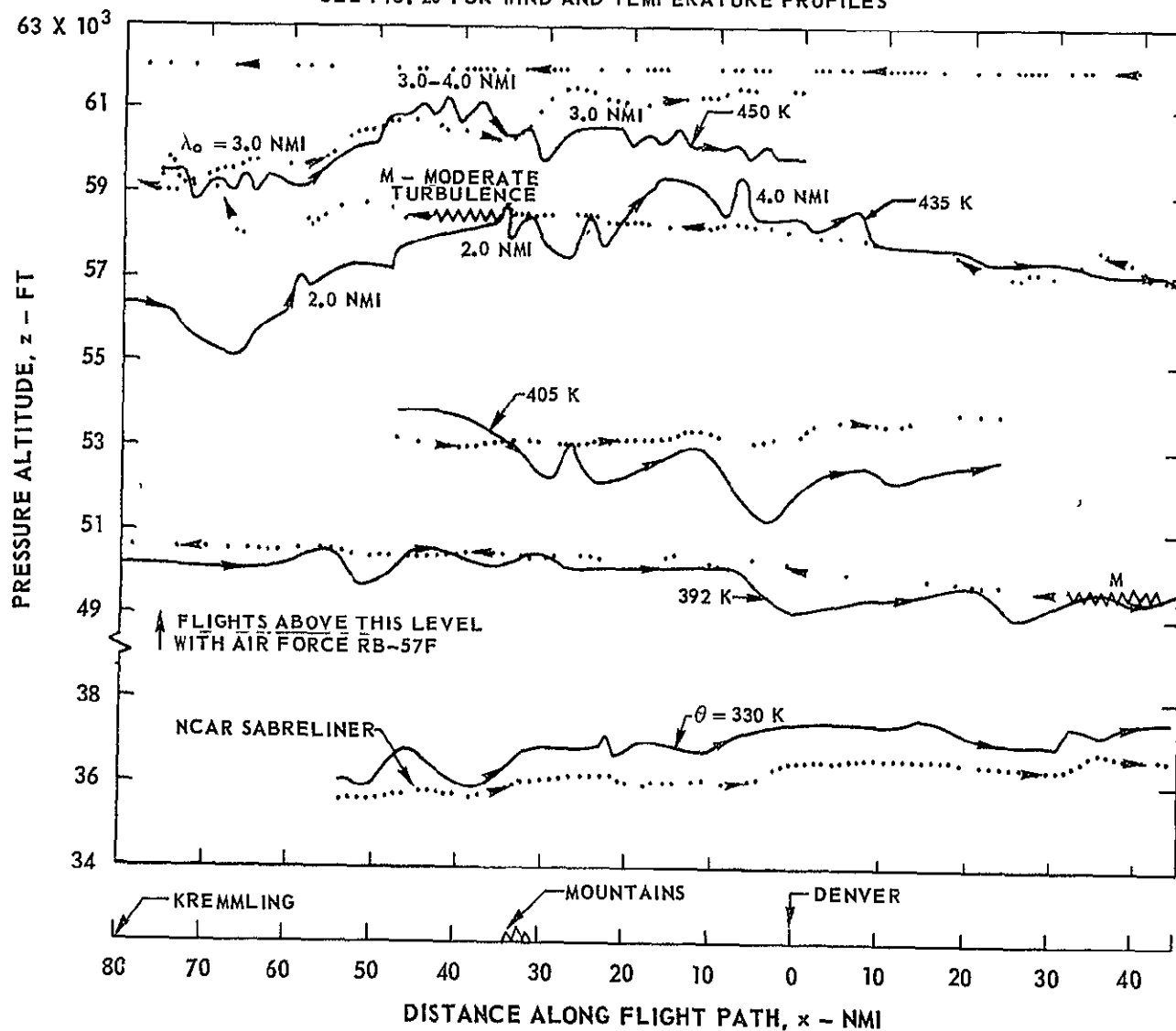
BASED ON DATA FROM 1970 LEE WAVE OBSERVATIONAL PROGRAM

1300-1600 GMT

AIRCRAFT FLIGHT PATHS APPROXIMATELY PARALLEL TO WIND

———— ISENTROPE FLIGHT PATH $\wedge\wedge\wedge$ TURBULENCE REPORTED

SEE FIG. 20 FOR WIND AND TEMPERATURE PROFILES



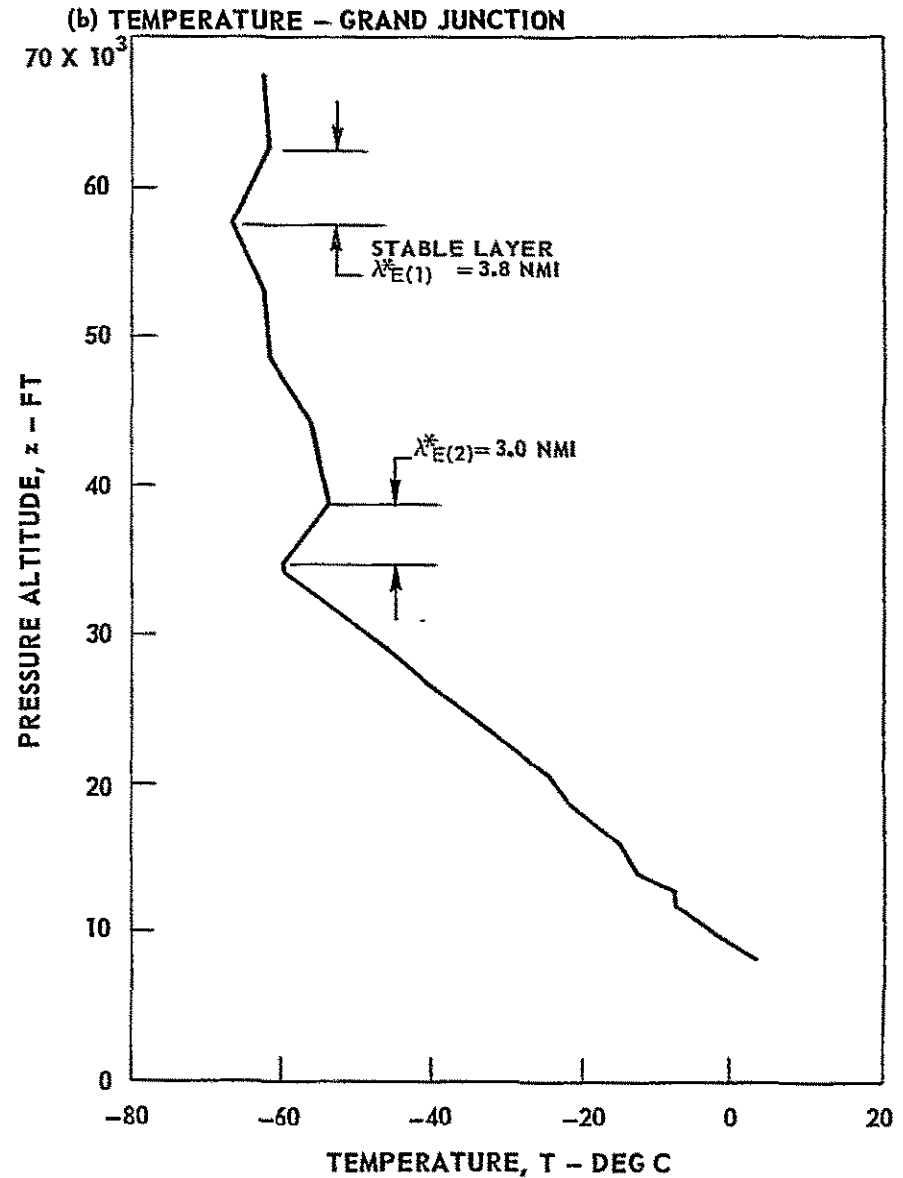
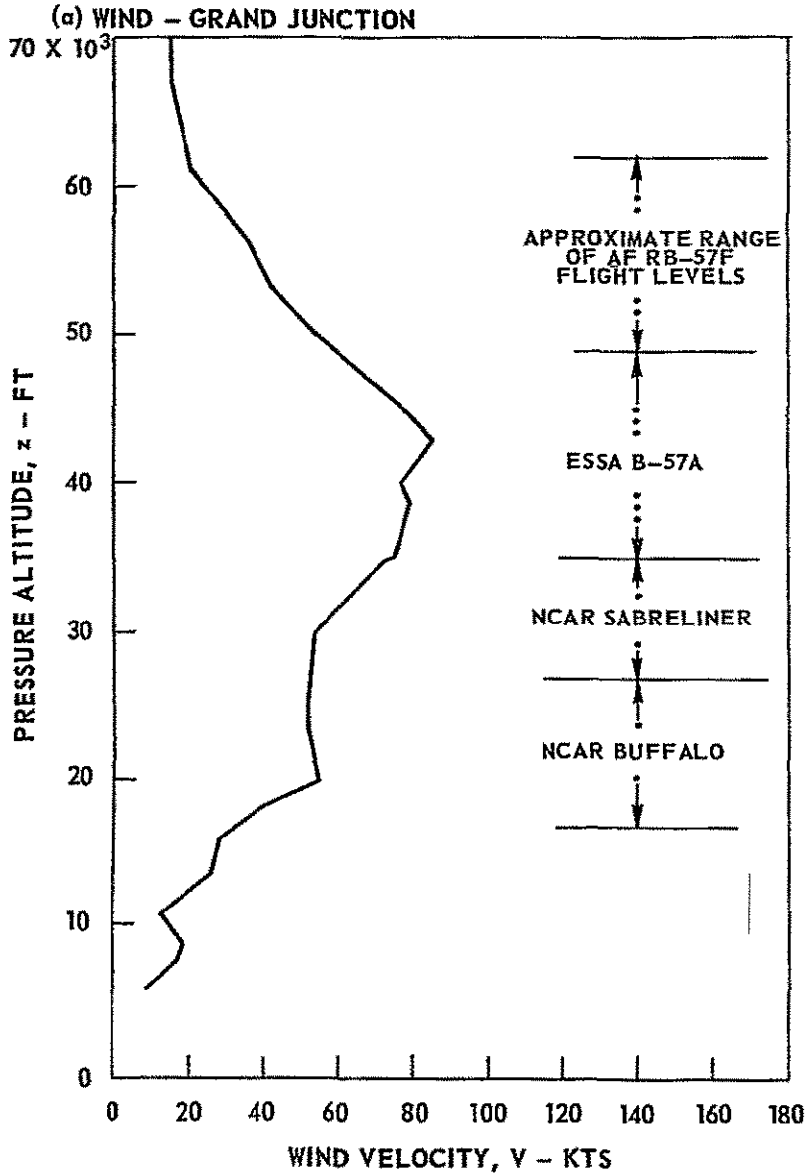
WIND AND TEMPERATURE PROFILES FOR COLORADO LEE WAVE CASE OF FEBRUARY 13, 1970

1200 GMT

PROFILES FROM RAWINSONDE DATA

$\lambda_E = (2\pi/\sqrt{2}) \cdot 2d$ λ_E^* DENOTES WAVES UNLIKELY TO OCCUR

SEE TABLE I FOR ADDITIONAL DETAILS



J910563-14

FIG. 20 (a), (b)

(CONTINUED)

WIND AND TEMPERATURE PROFILES FOR COLORADO LEE WAVE CASE OF FEBRUARY 13, 1970

(CONTINUED)

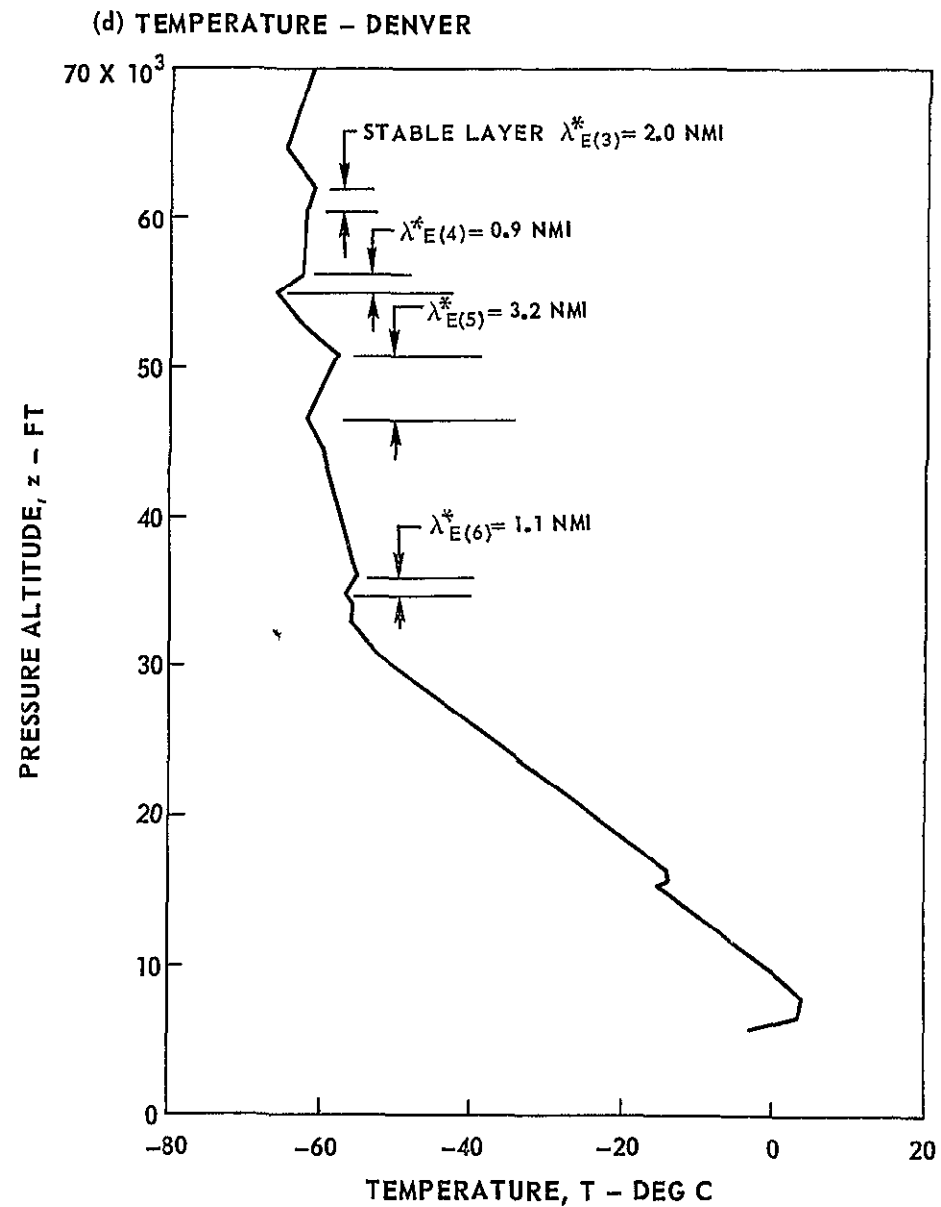
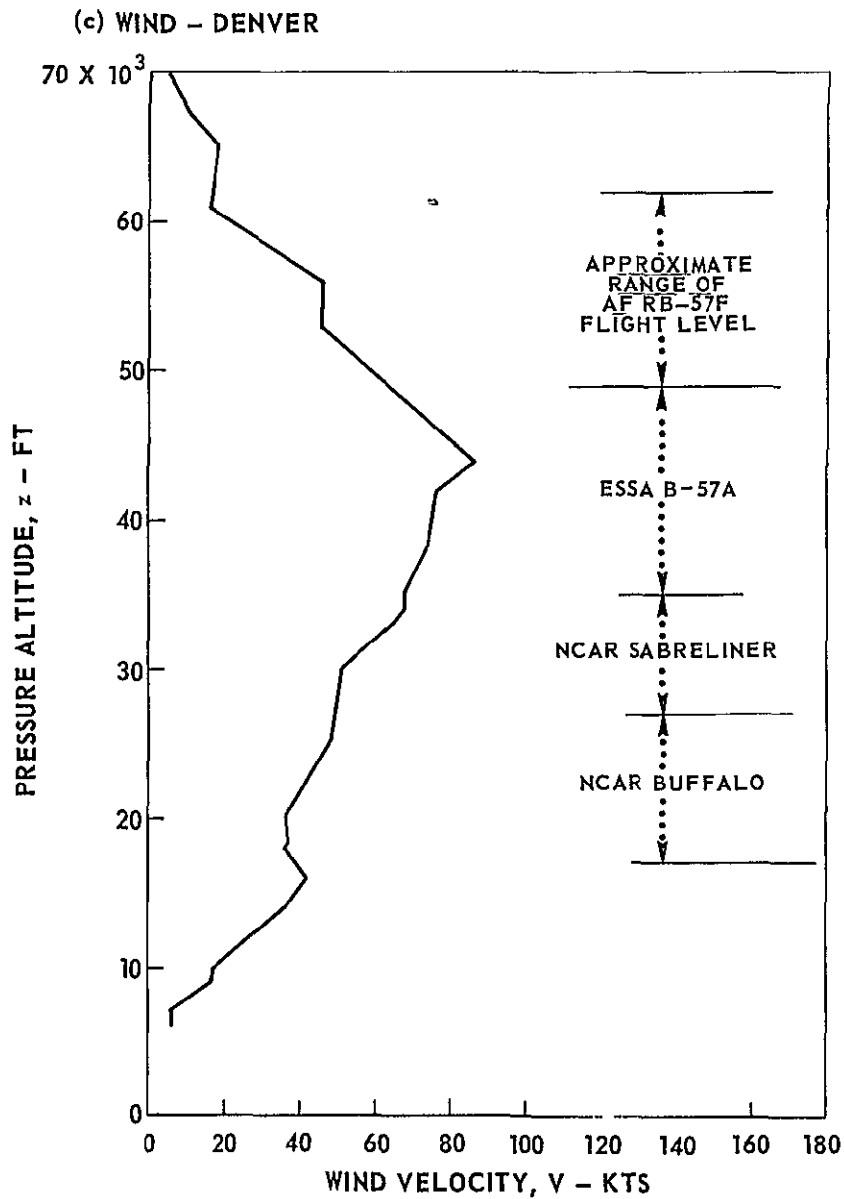


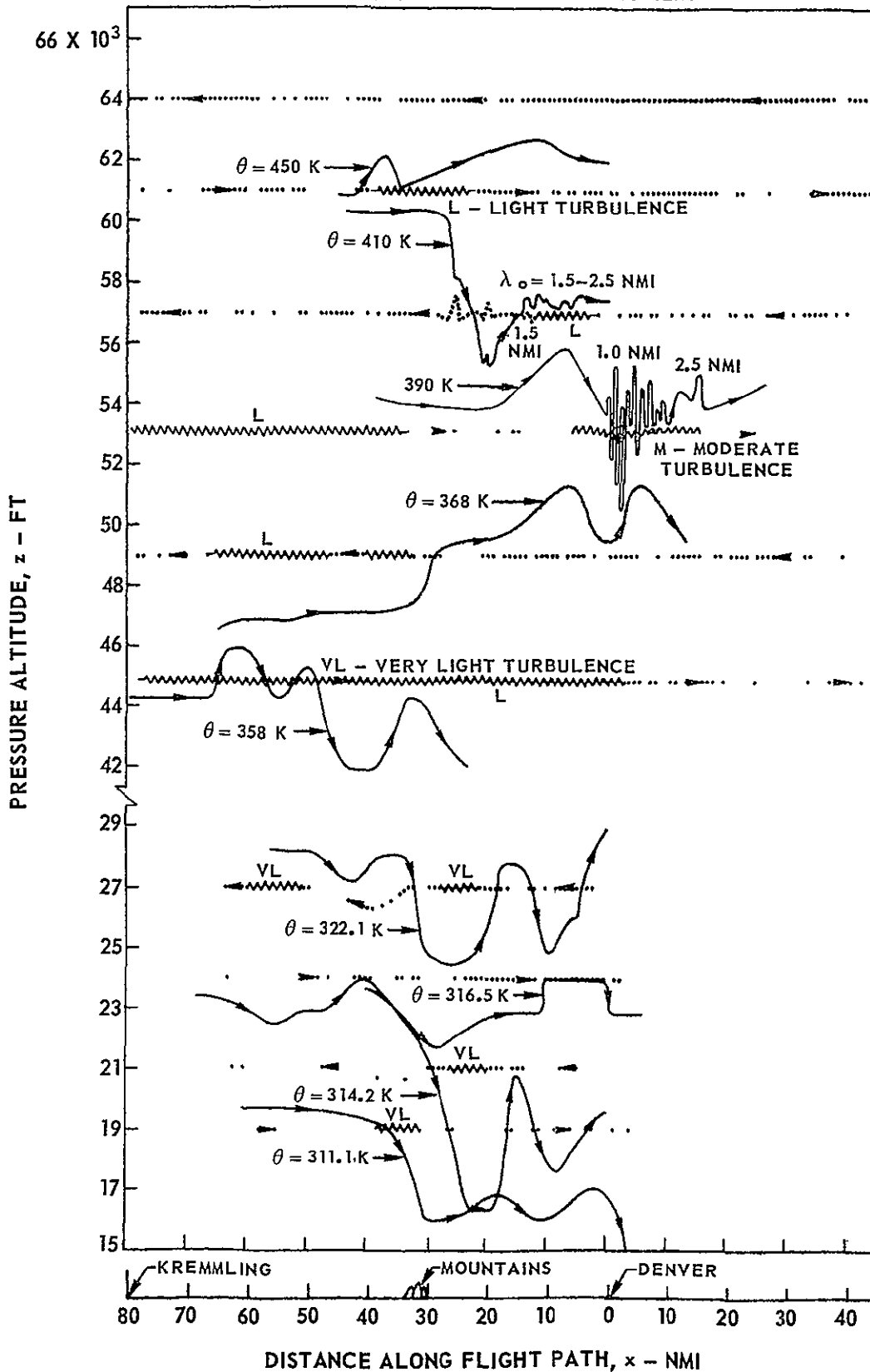
FIG. 20 (c),(d)

ISENTROPES FOR COLORADO LEE WAVE CASE OF FEBRUARY 17, 1970

BASED ON DATA FROM 1970 LEE WAVE OBSERVATIONAL PROGRAM
1300-1600 GMT

AIRCRAFT FLIGHT PATHS APPROXIMATELY PARALLEL TO WIND

— ISENTROPE ····· FLIGHT PATH  TURBULENCE REPORTED
SEE FIG. 22 FOR WIND AND TEMPERATURE PROFILES



WIND AND TEMPERATURE PROFILES FOR COLORADO LEE WAVE CASE OF FEBRUARY 17, 1970

PROFILES FROM RAWINSONDE DATA

$$\lambda_E = (2\pi/\sqrt{2}) \cdot 2d \quad \lambda_E^* \text{ DENOTES WAVE UNLIKELY TO OCCUR}$$

SEE TABLE I FOR ADDITIONAL DETAILS

J910563-14

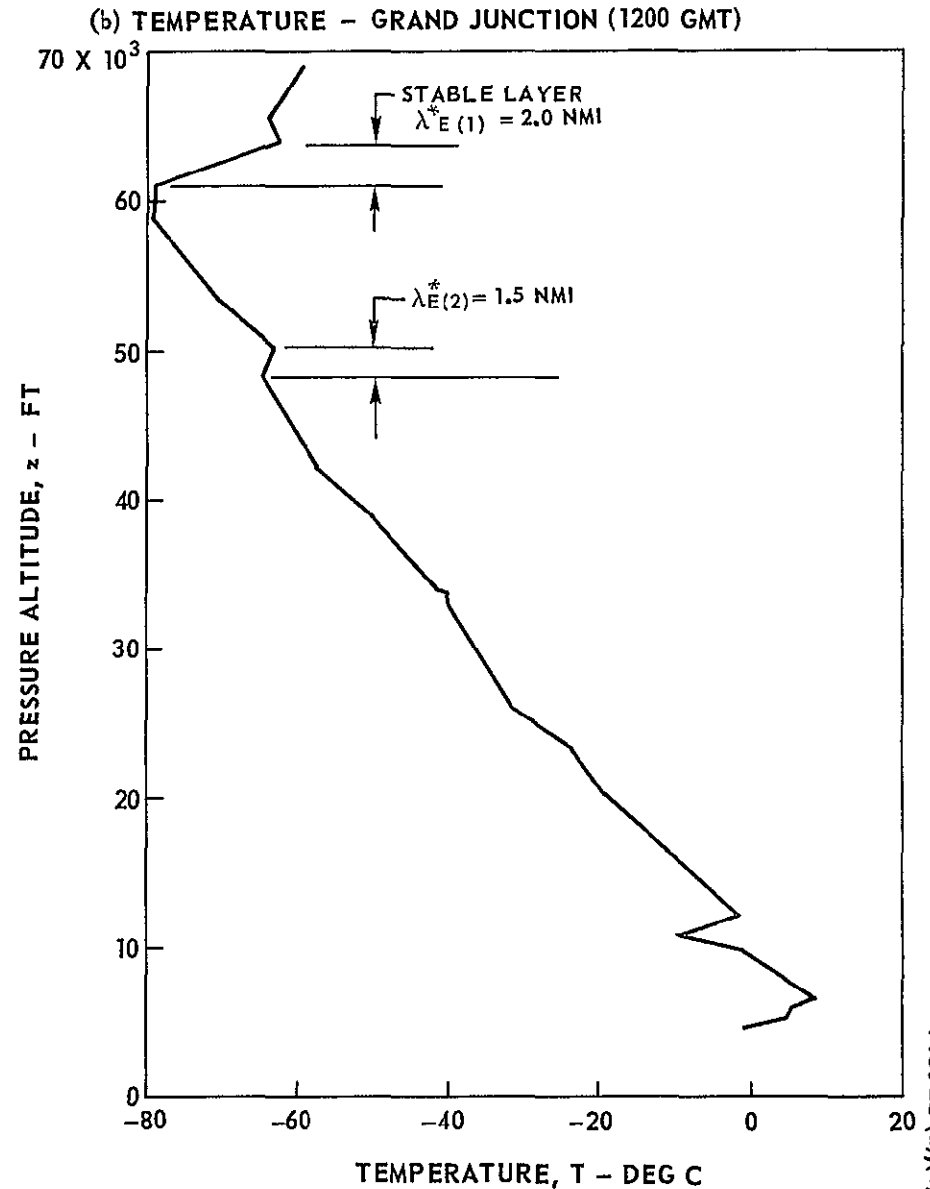
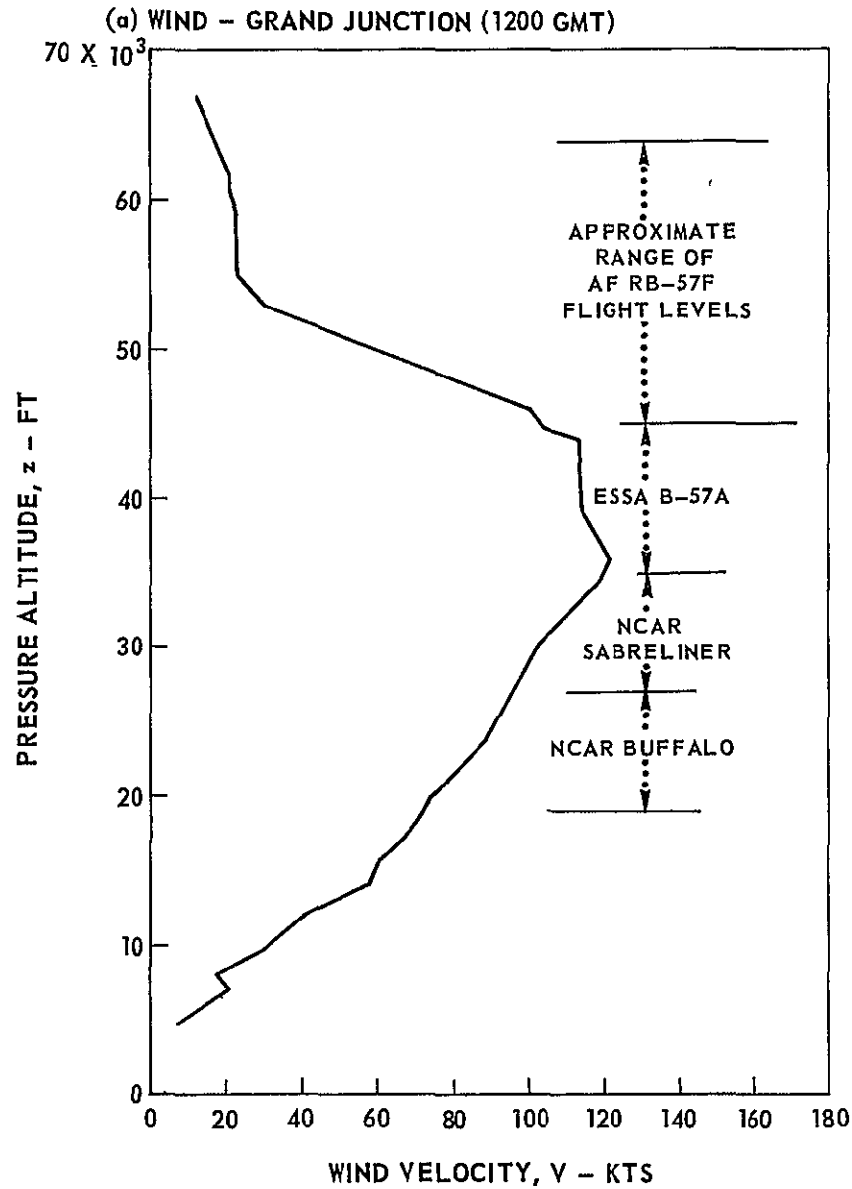


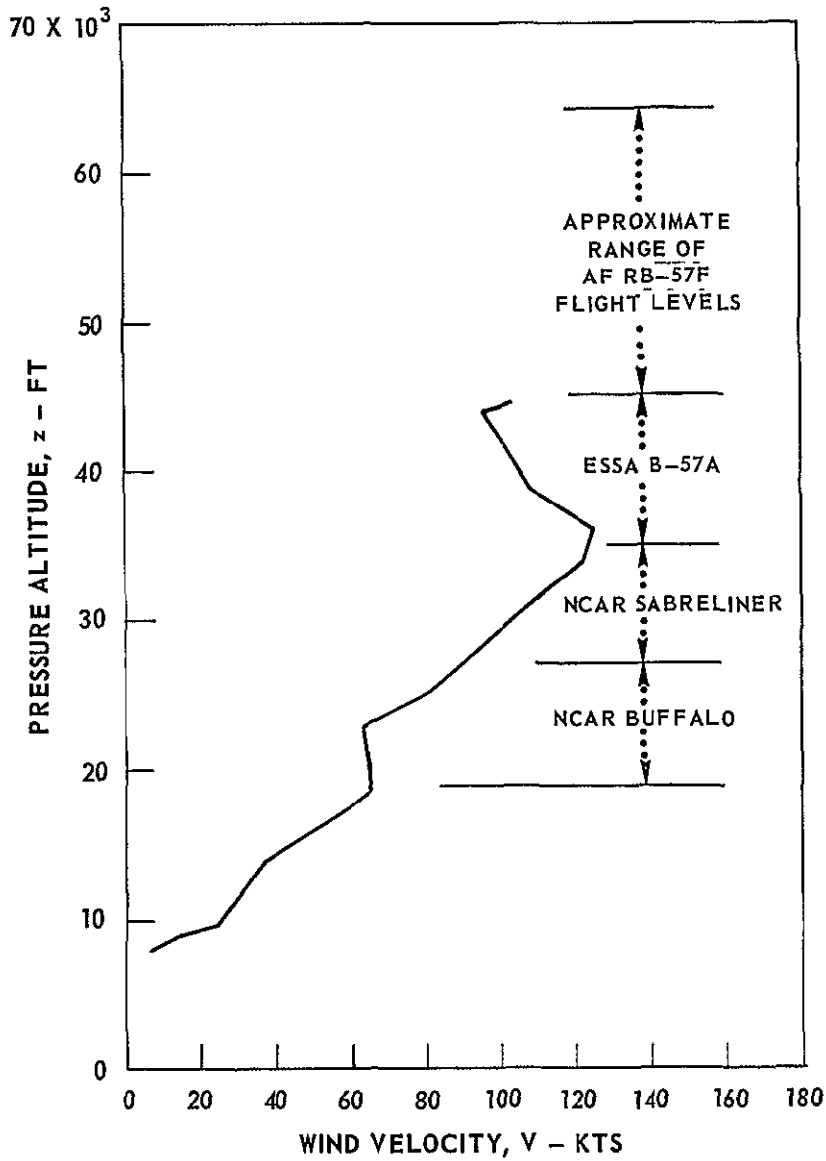
FIG. 22 (a),(b)

(CONTINUED)

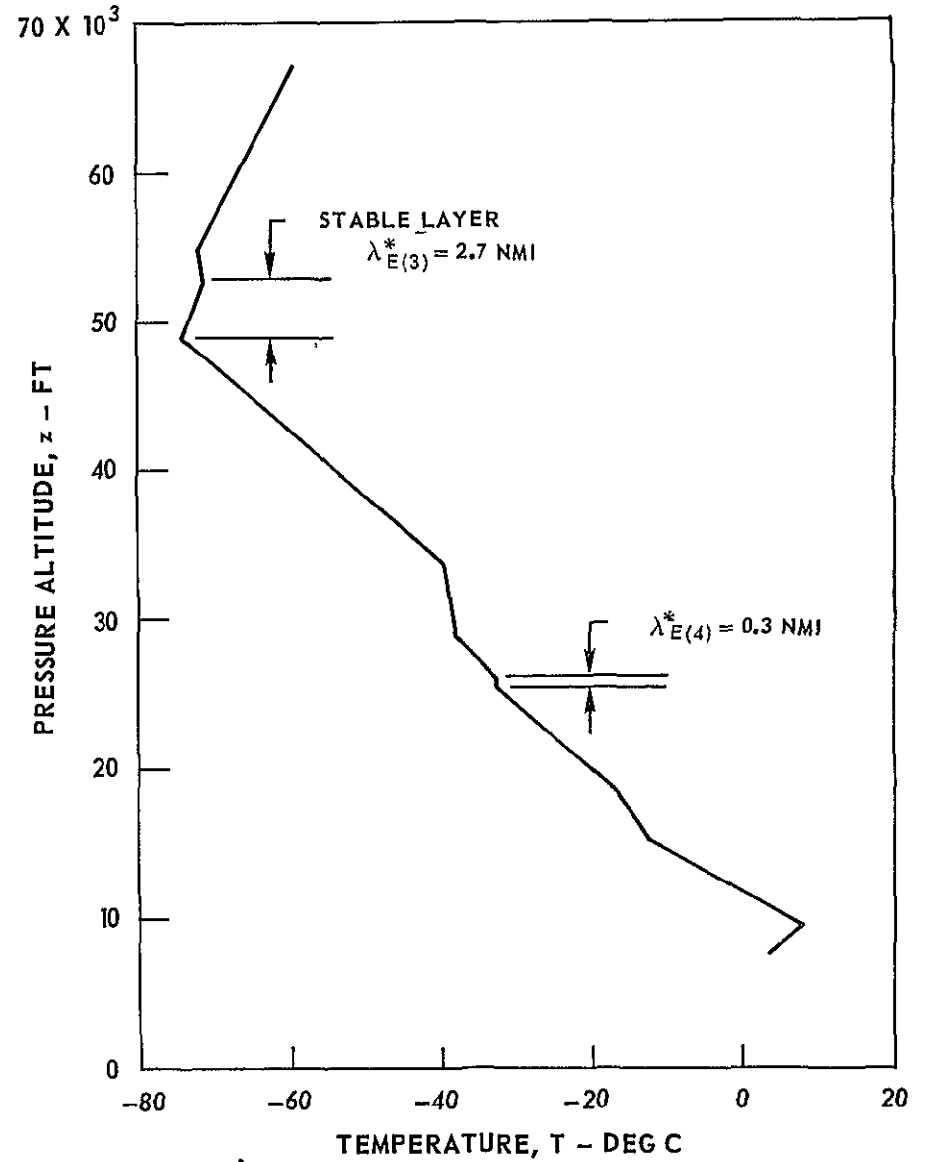
WIND AND TEMPERATURE PROFILES FOR COLORADO LEE WAVE CASE OF FEBRUARY 17, 1970

(CONTINUED)

a) WIND - KREMMLING (0900 GMT)



b) TEMPERATURE - KREMMLING (0900 GMT)



J910563-14

FIG. 22 (c),(d)

(CONTINUED)

WIND AND TEMPERATURE PROFILES FOR COLORADO LEE WAVE CASE OF FEBRUARY 17, 1970
(CONTINUED)

J910563-14

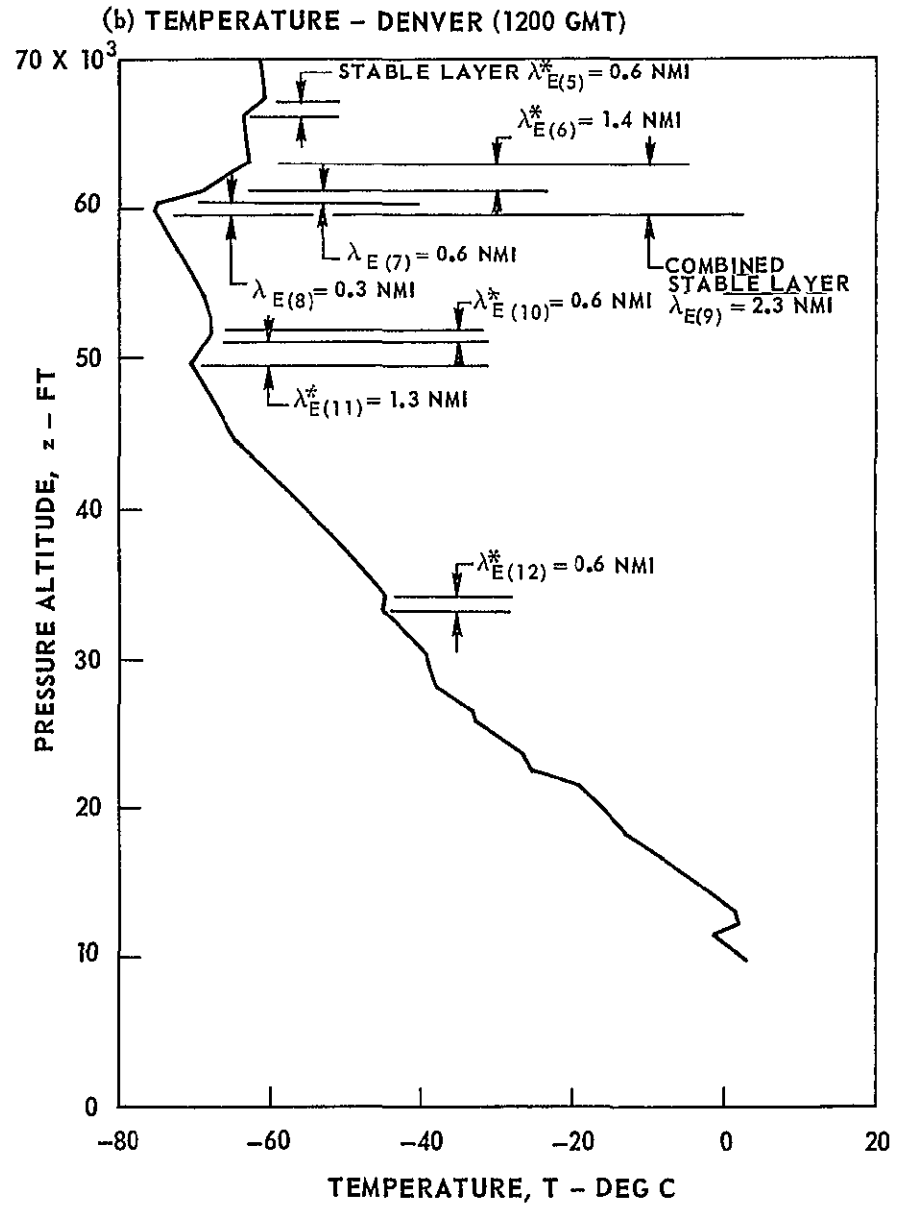
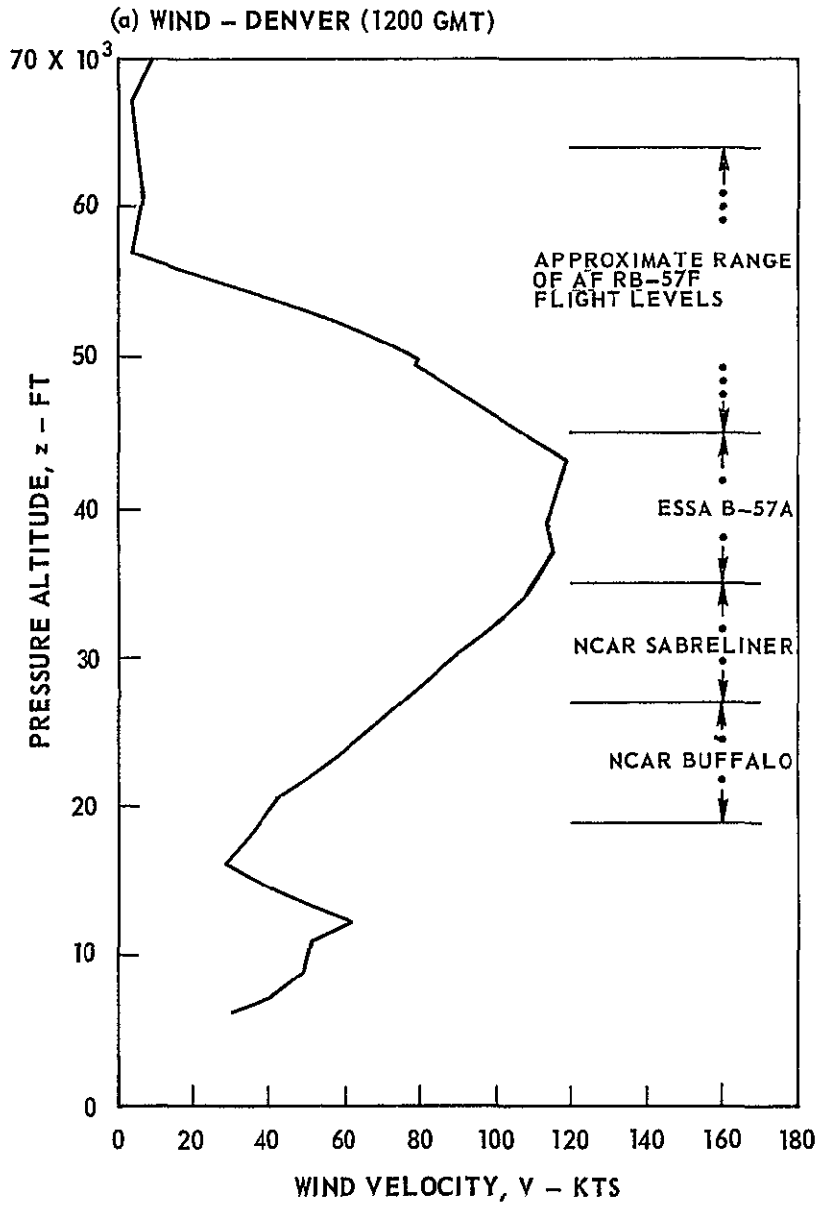


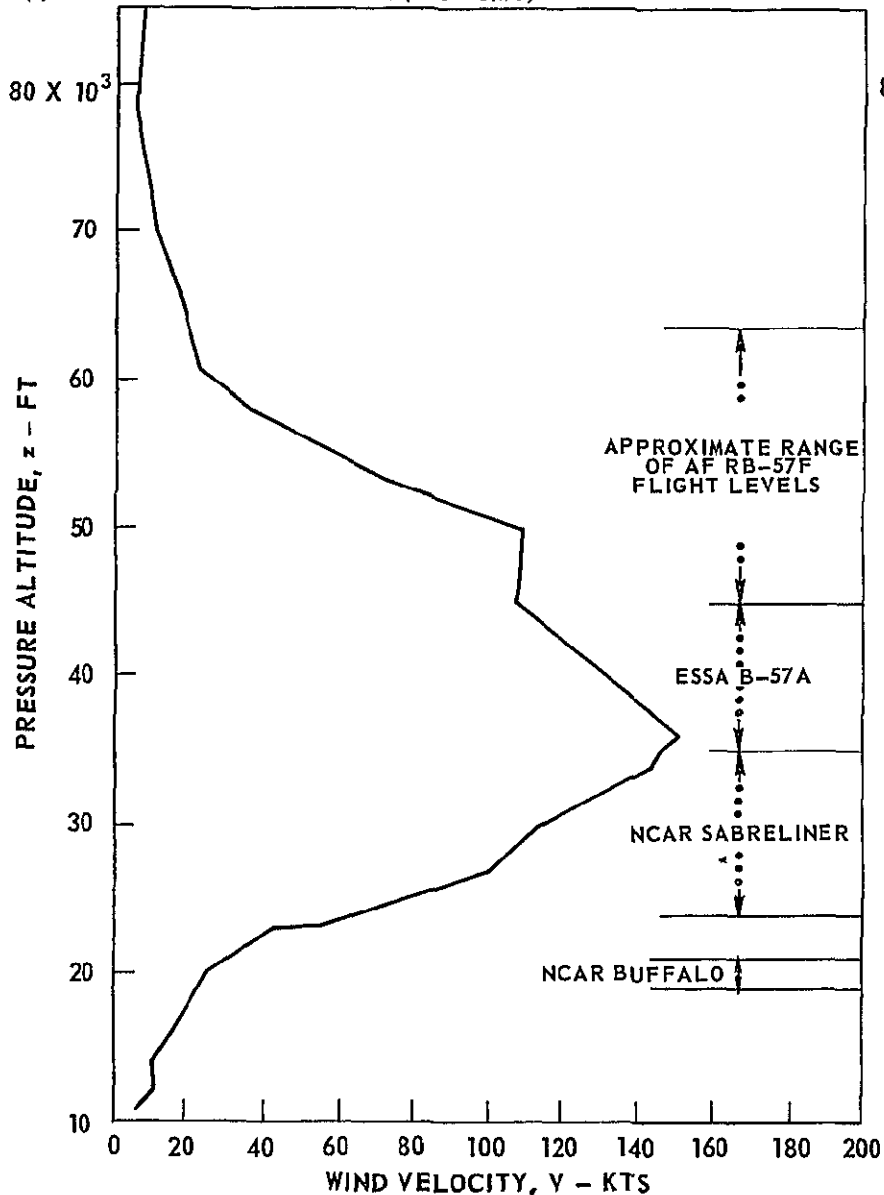
FIG. 22 (e), (f)

WIND AND TEMPERATURE FOR COLORADO LEE WAVE CASE FOR FEBRUARY 18, 1970

PROFILES FROM RAWINSONDE DATA
 $\lambda_E = (2\pi/\sqrt{2}) 2d$ λ_E^* DENOTES WAVE UNLIKELY TO OCCUR
 SEE TABLE I FOR ADDITIONAL DETAILS

J910563-14

(a) WIND - GRAND JUNCTION (2400 GMT)



(b) TEMPERATURE - GRAND JUNCTION (2400 GMT)

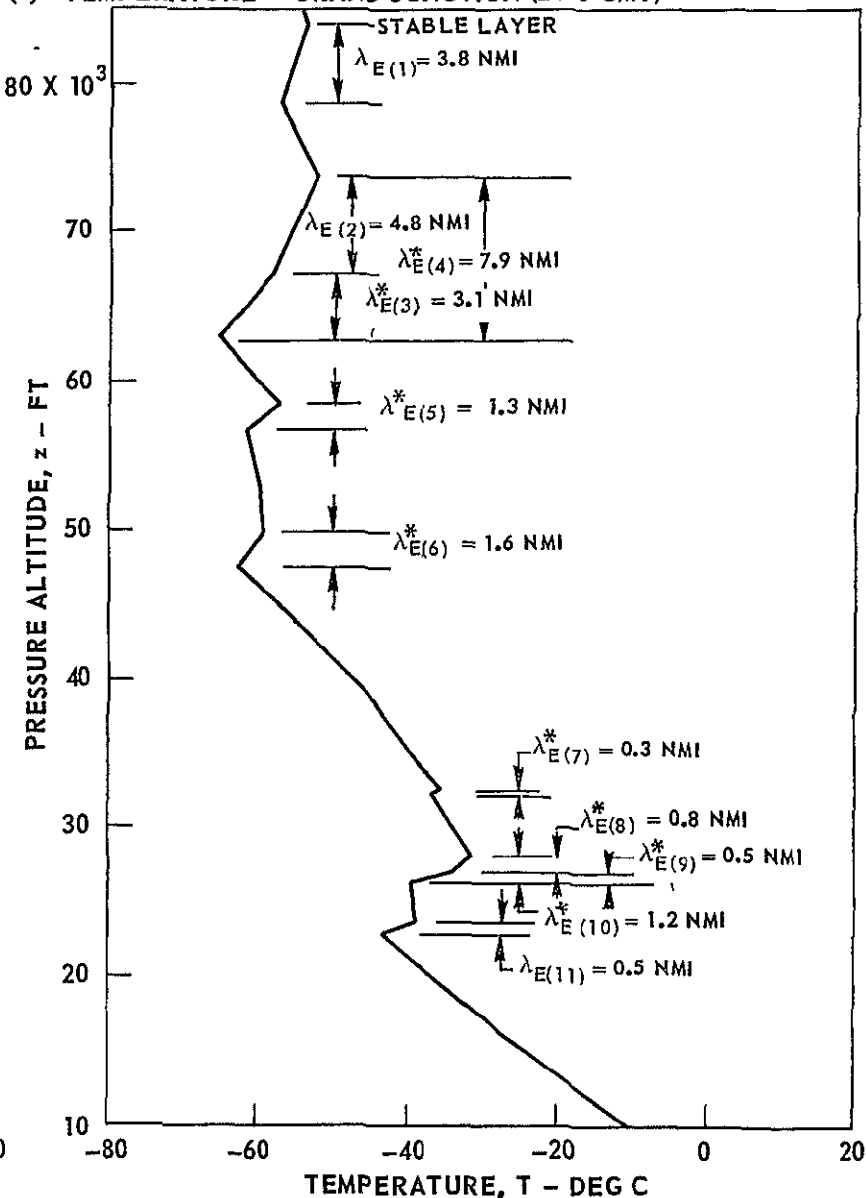


FIG. 24 (a),(b)

(CONTINUED)

WIND AND TEMPERATURE PROFILES FOR COLORADO LEE WAVE CASE OF FEBRUARY 18, 1970
(CONTINUED)

J910563-14

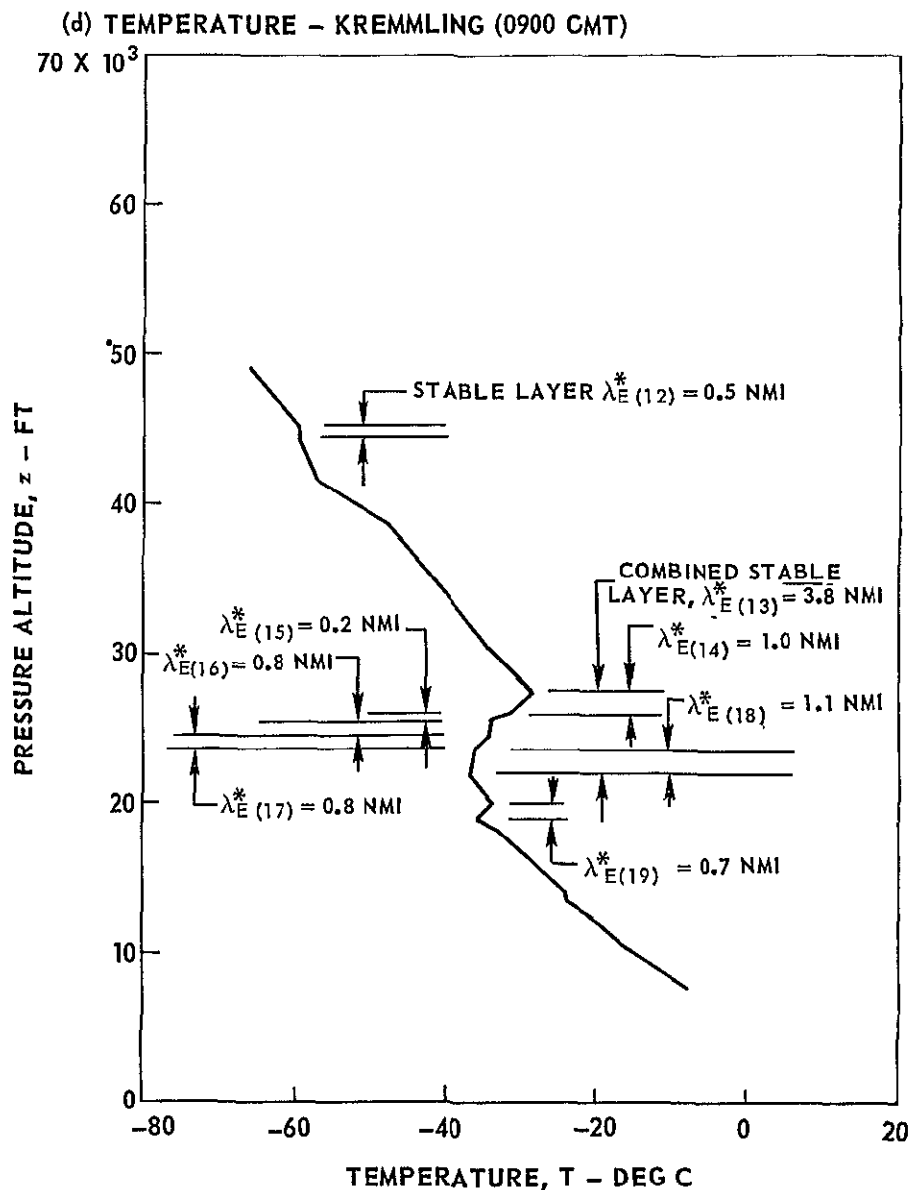
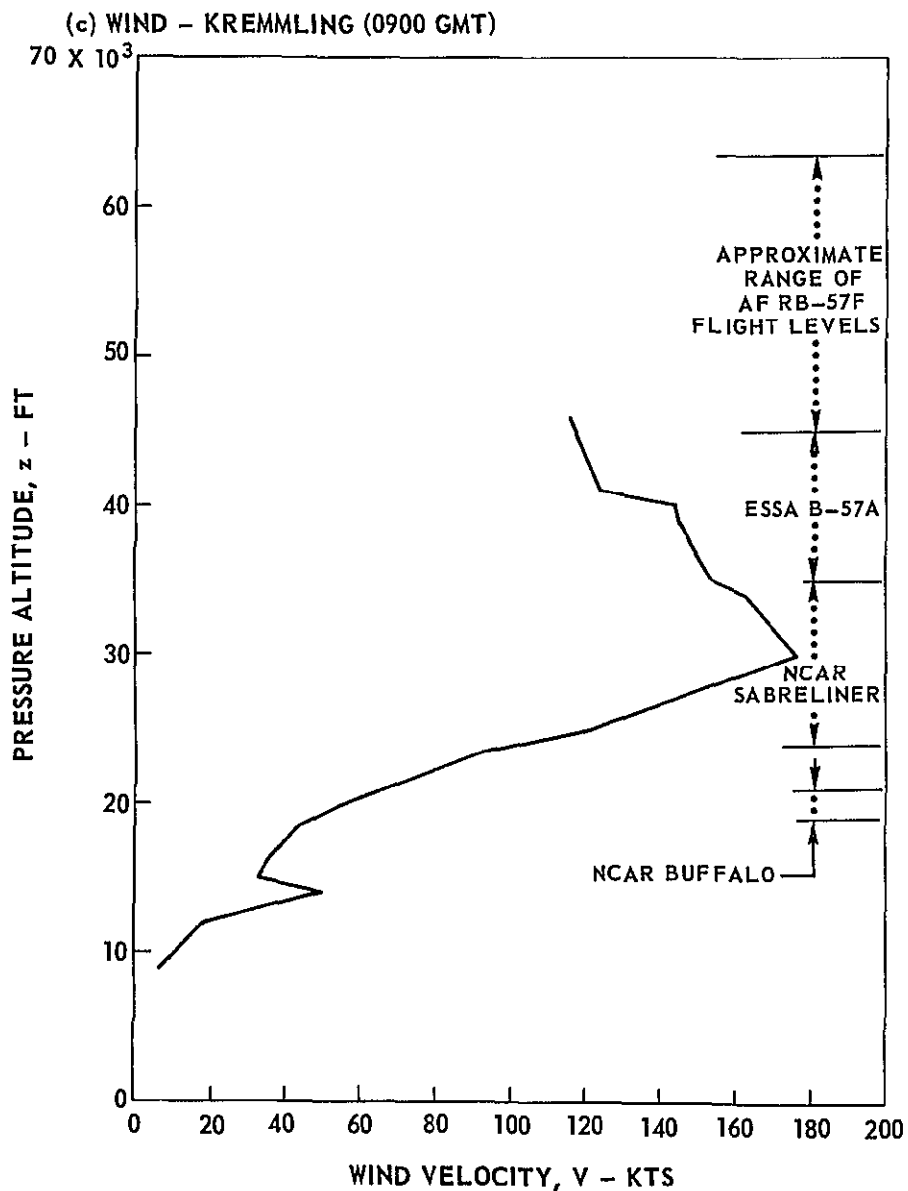


FIG. 24 (c),(d)

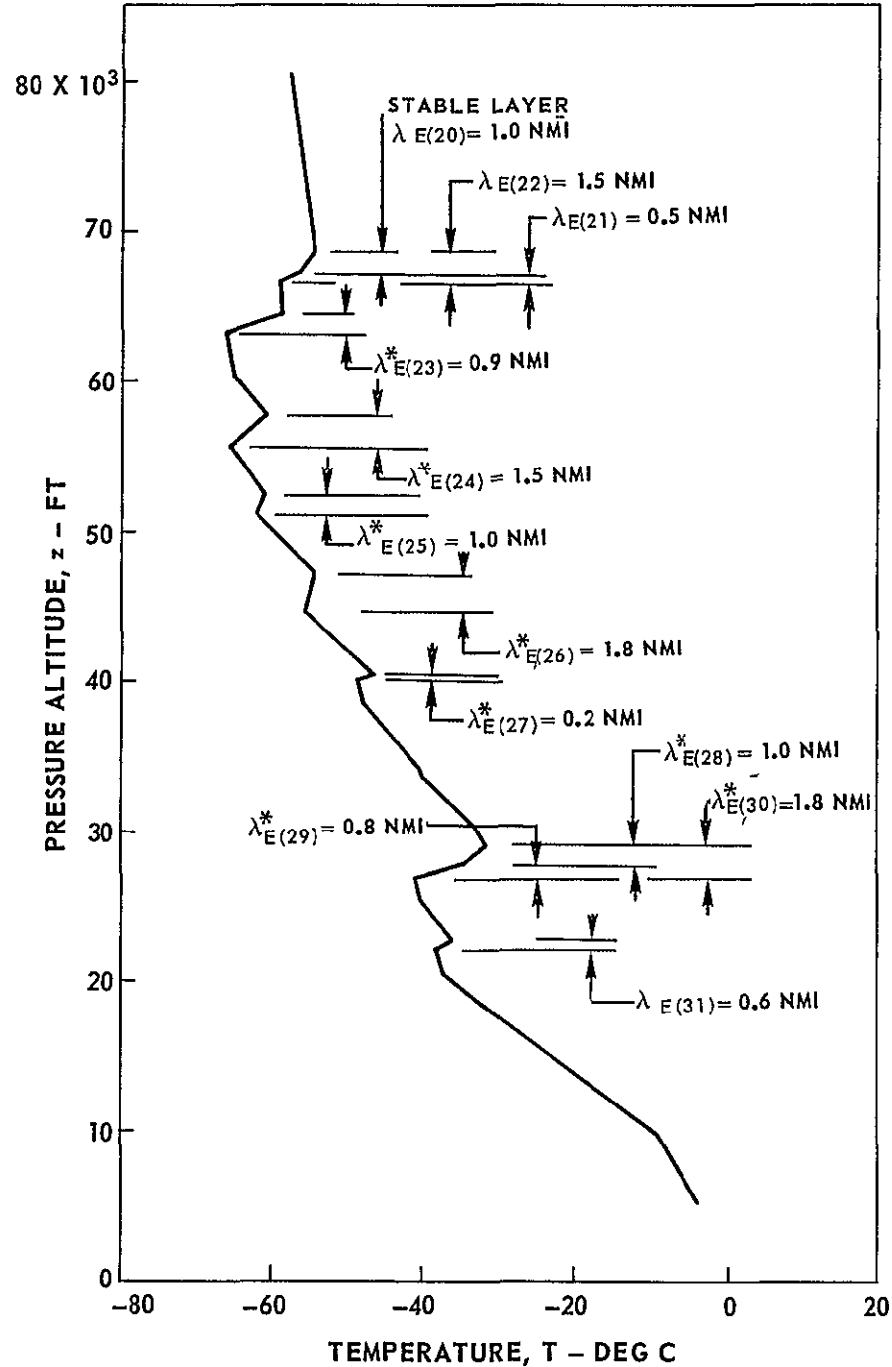
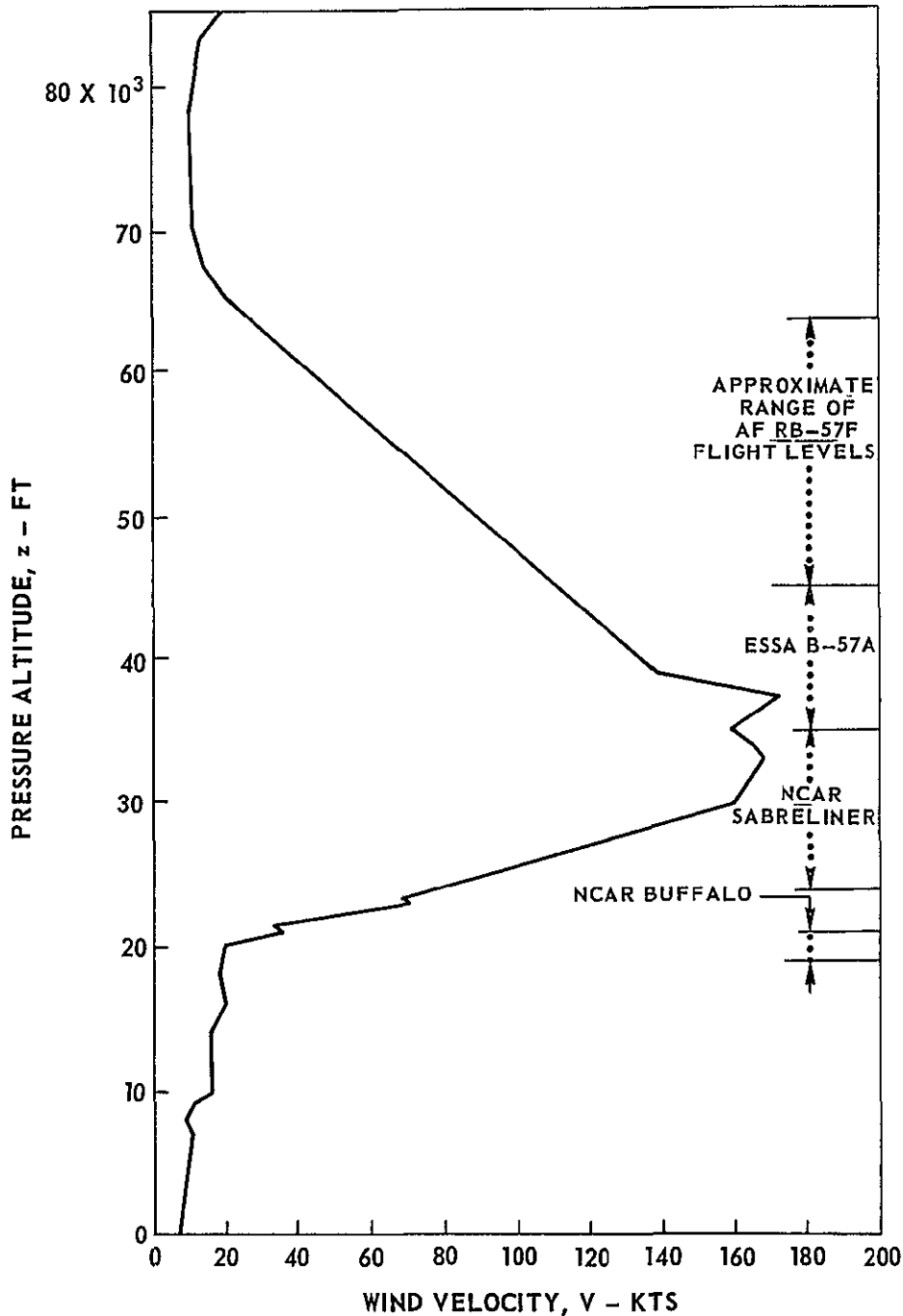
(CONTINUED)

WIND AND TEMPERATURE PROFILES FOR COLORADO LEE WAVE CASE FOR FEBRUARY 18, 1970

(CONTINUED)

(e) WIND - DENVER (2400 GMT)


(f) TEMPERATURE - DENVER (2400 GMT)



ISENTROPES FOR PROJECT HICAT TEST 198, RUNS 9, 12 AND 13

CAT ASSOCIATED WITH THUNDERSTORM ACTIVITY

MAY 5, 1967

———— ISENTROPE FLIGHT PATH  TURBULENCE REPORTED
SEE FIG 26 FOR WIND AND TEMPERATURE PROFILES

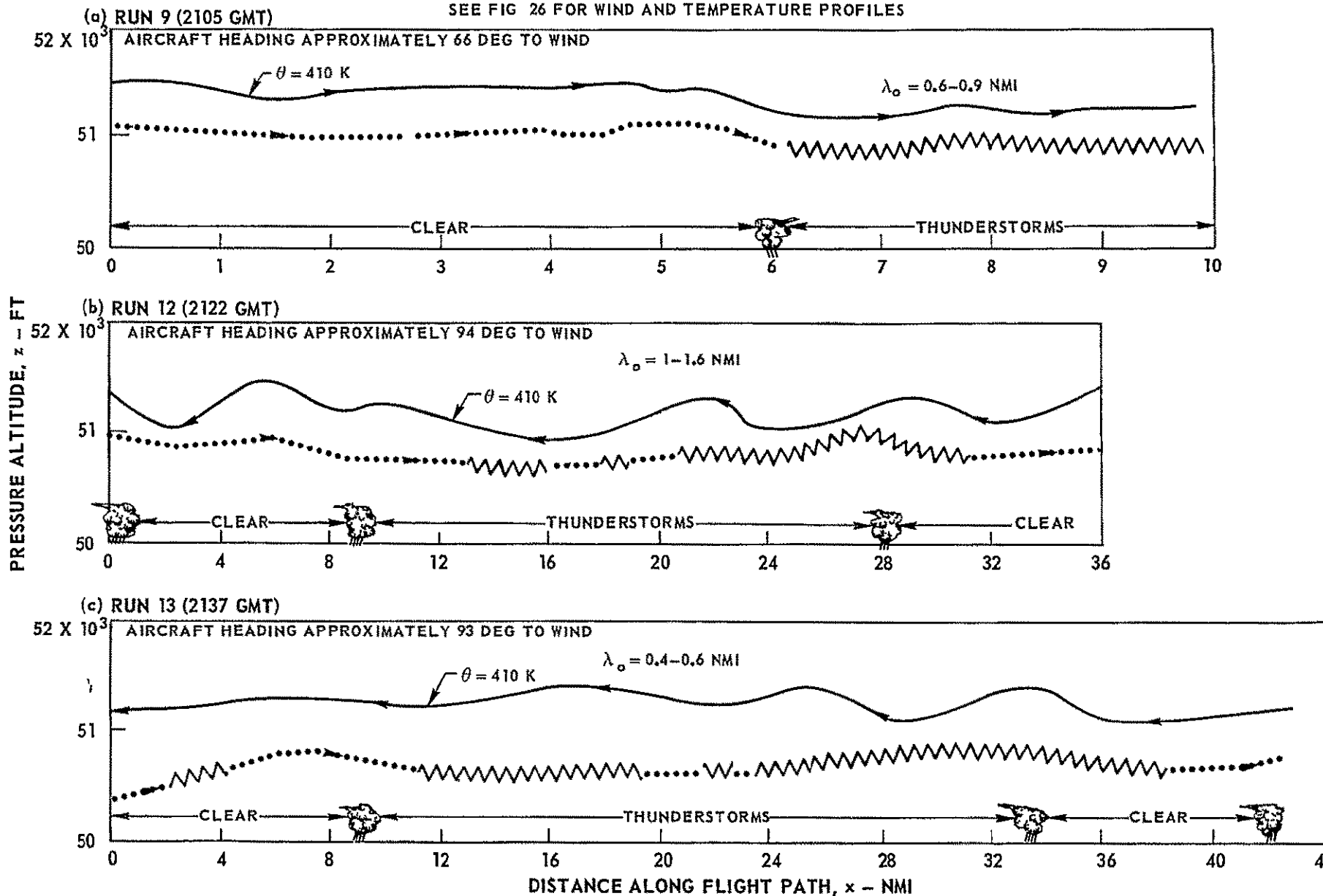


FIG. 25

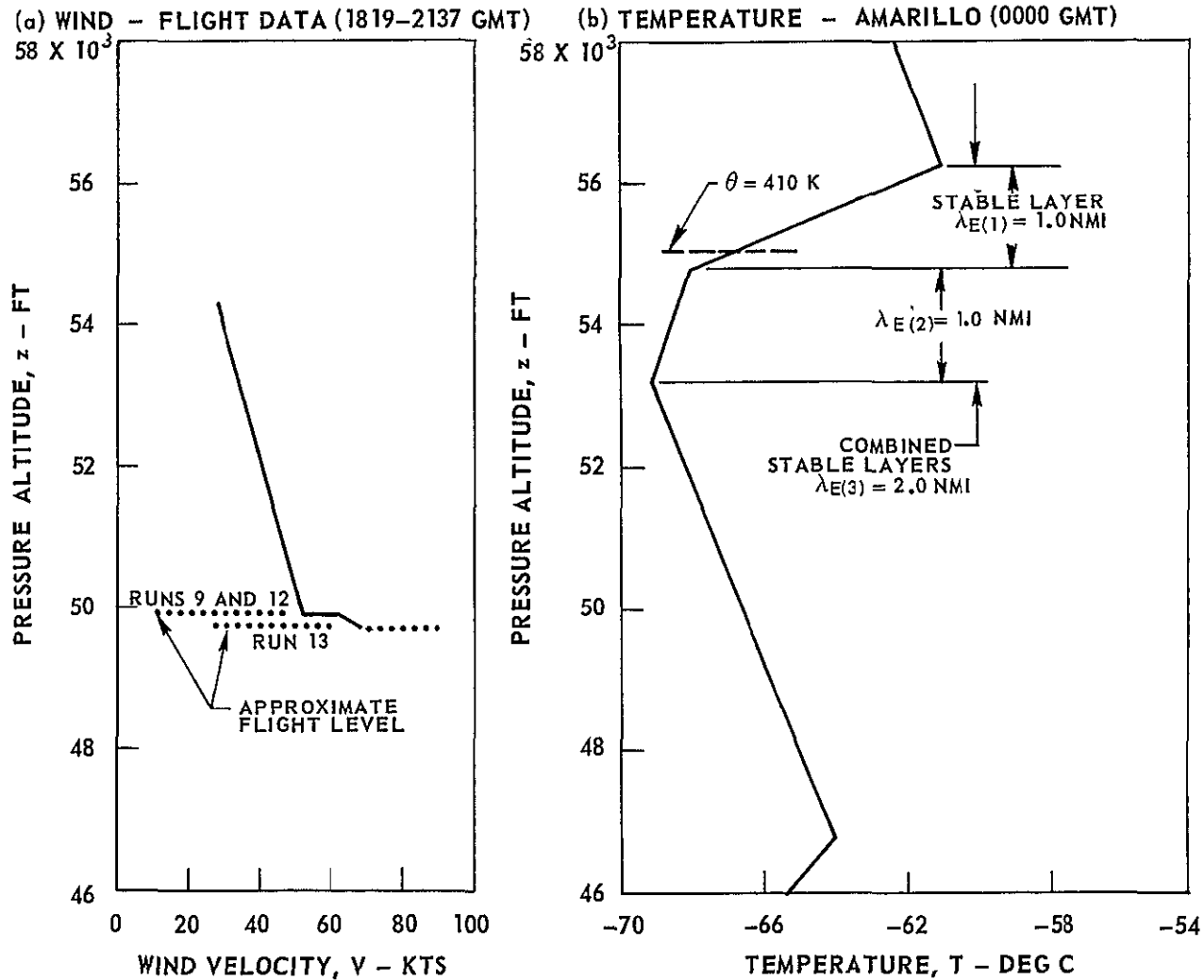
WIND AND TEMPERATURE PROFILES FOR PROJECT HICAT TEST 198, RUNS 9, 12, AND 13

MAY 5, 1967

PROFILES ARE COMPOSITES OF AIRCRAFT AND RAWINSONDE DATA

$$\lambda_E = (2\pi / \sqrt{2}) \cdot 2d$$

SEE TABLE I FOR ADDITIONAL DETAILS



WIND AND TEMPERATURE PROFILES AND ISENTROPE FOR PROJECT HICAT TEST 202, RUN 8

CAT ASSOCIATED WITH THUNDERSTORM ACTIVITY

MAY 12, 1967

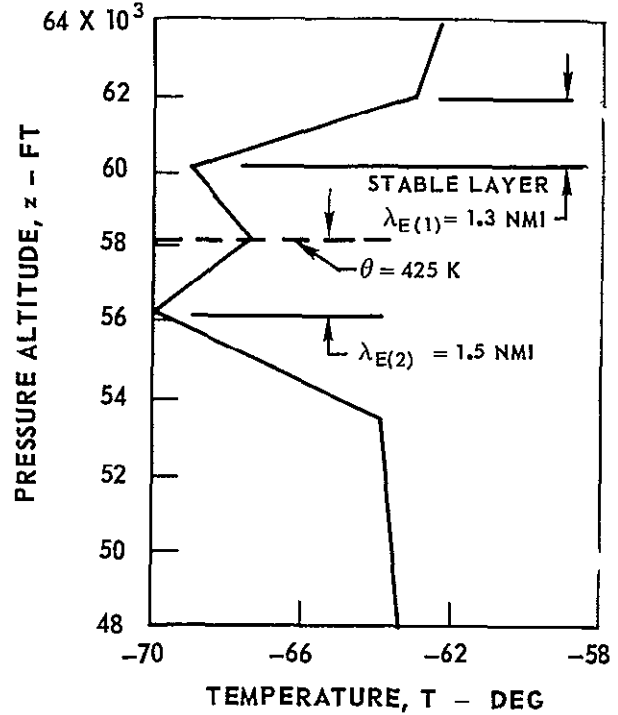
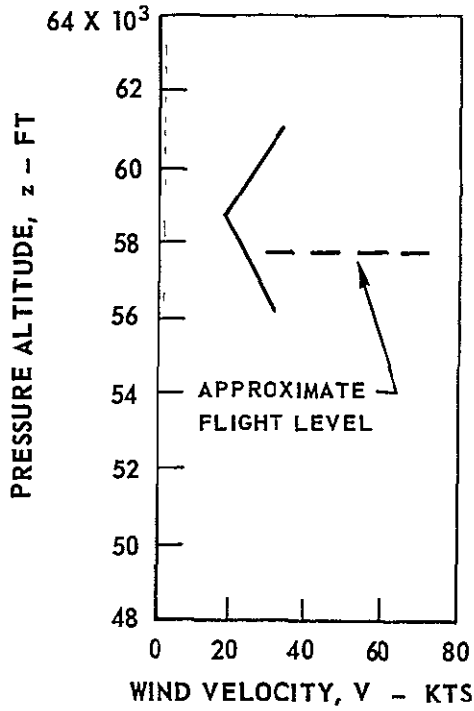
PROFILES ARE COMPOSITES OF AIRCRAFT AND RAWINSONDE DATA

$$\lambda_E = (2\pi/\sqrt{2}) \cdot 2d$$

SEE TABLE I FOR ADDITIONAL DETAILS

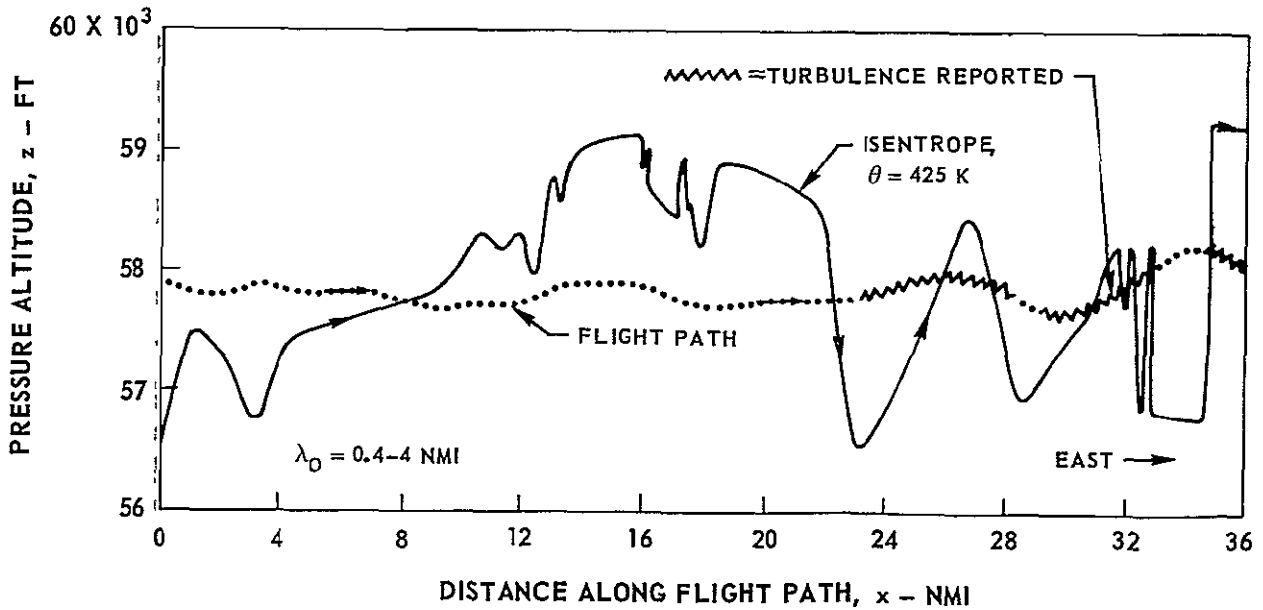
(a) WIND - FLIGHT DATA (1813-2022 GMT)

(b) TEMPERATURE - OKLAHOMA CITY, (1200 GMT)



(c) ISENTROPE

AIRCRAFT HEADING APPROXIMATELY 22 DEG TO WIND



WIND AND TEMPERATURE PROFILES AND ISENTROPE FOR PROJECT HICAT TEST 233, RUN 3

CAT ASSOCIATED WITH THUNDERSTORM ACTIVITY

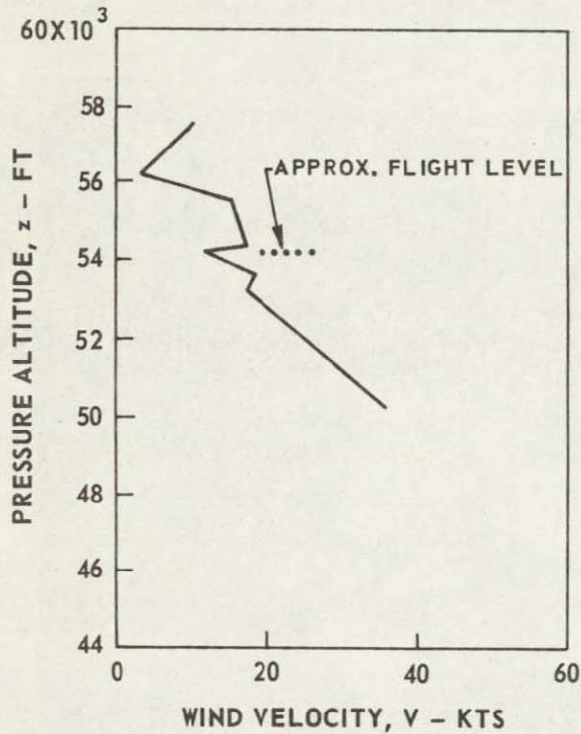
AUGUST 7, 1967

PROFILES ARE COMPOSITES OF AIRCRAFT AND RAWINSONDE DATA

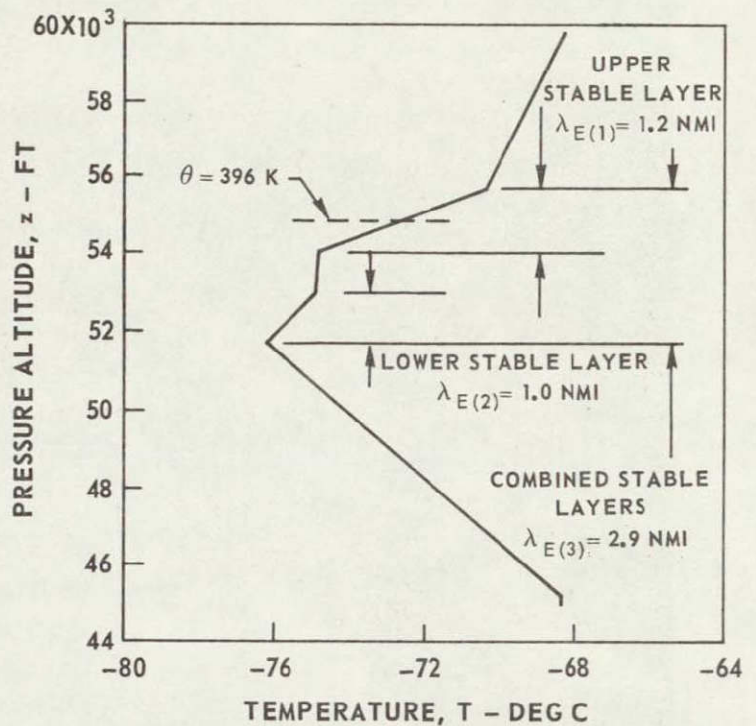
$$\lambda_E = (2\pi/\sqrt{2}) \cdot 2d$$

SEE TABLE I FOR ADDITIONAL DETAILS

(a) WIND - FLIGHT DATA (1546-1809 GMT)

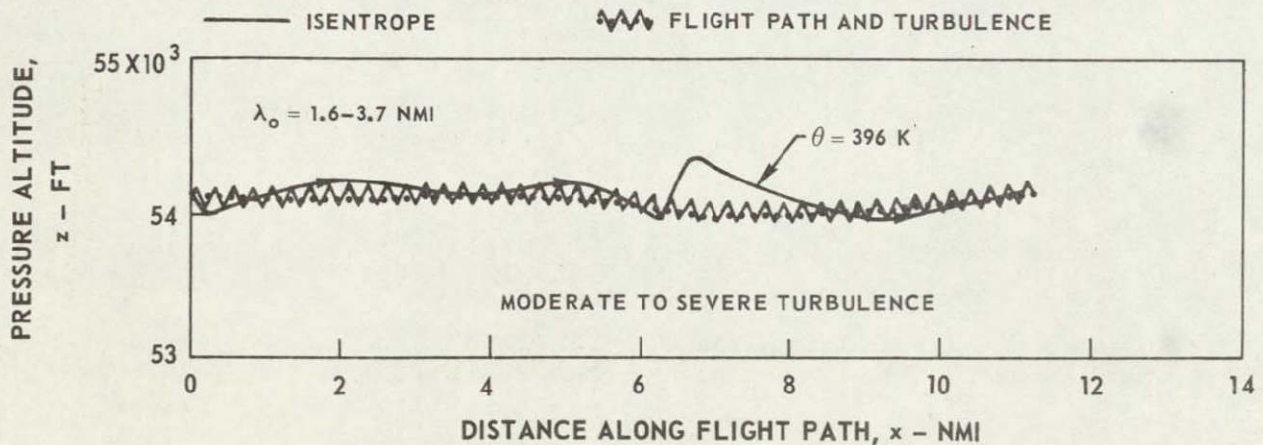


(b) TEMPERATURE - HOWARD AFB (0000 GMT)

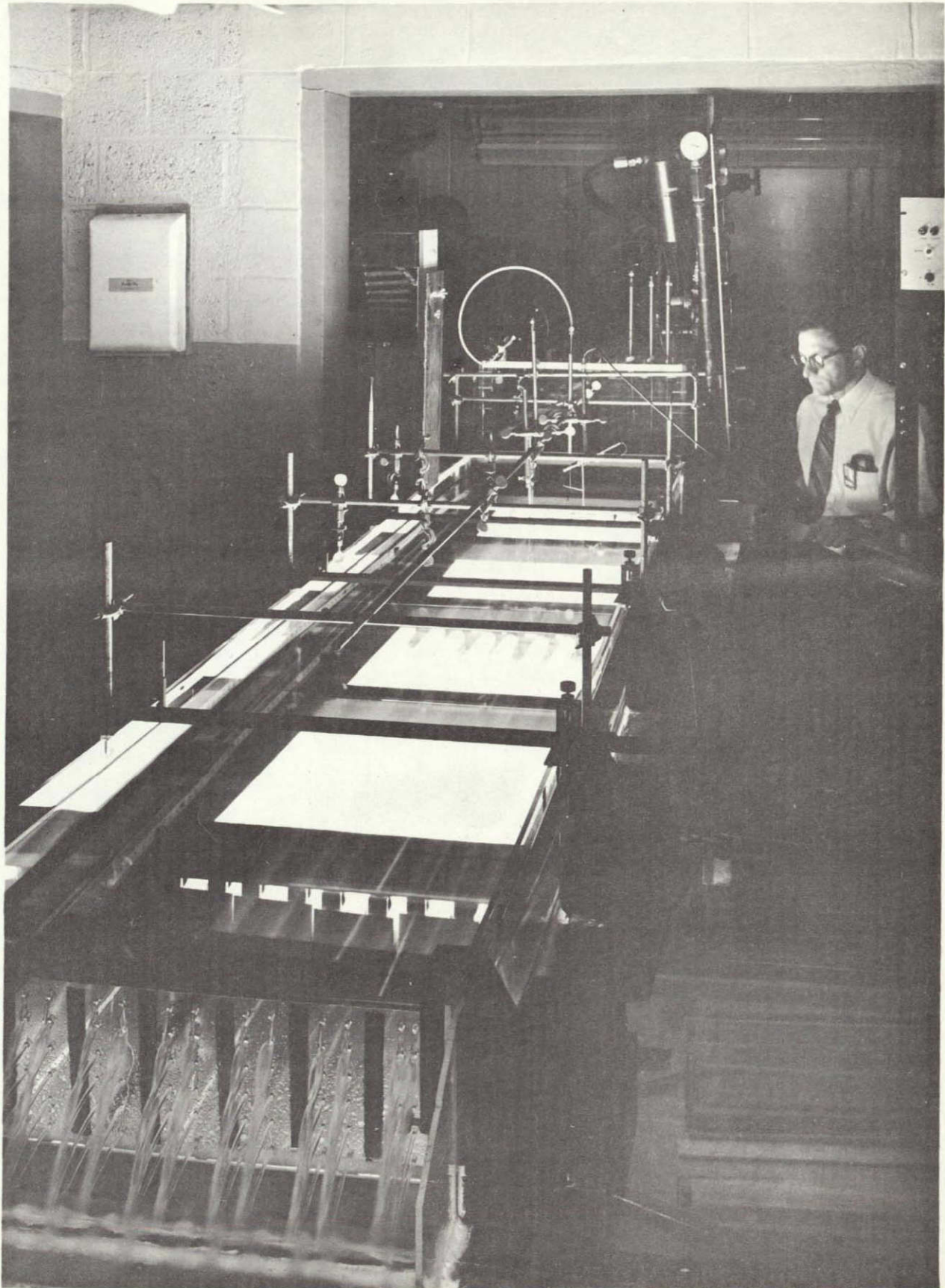


(c) ISENTROPE

AIRCRAFT HEADING APPROXIMATELY 13 DEG TO WIND



PHOTOGRAPH OF UARL OPEN WATER CHANNEL



SKETCH OF UARL OPEN WATER CHANNEL

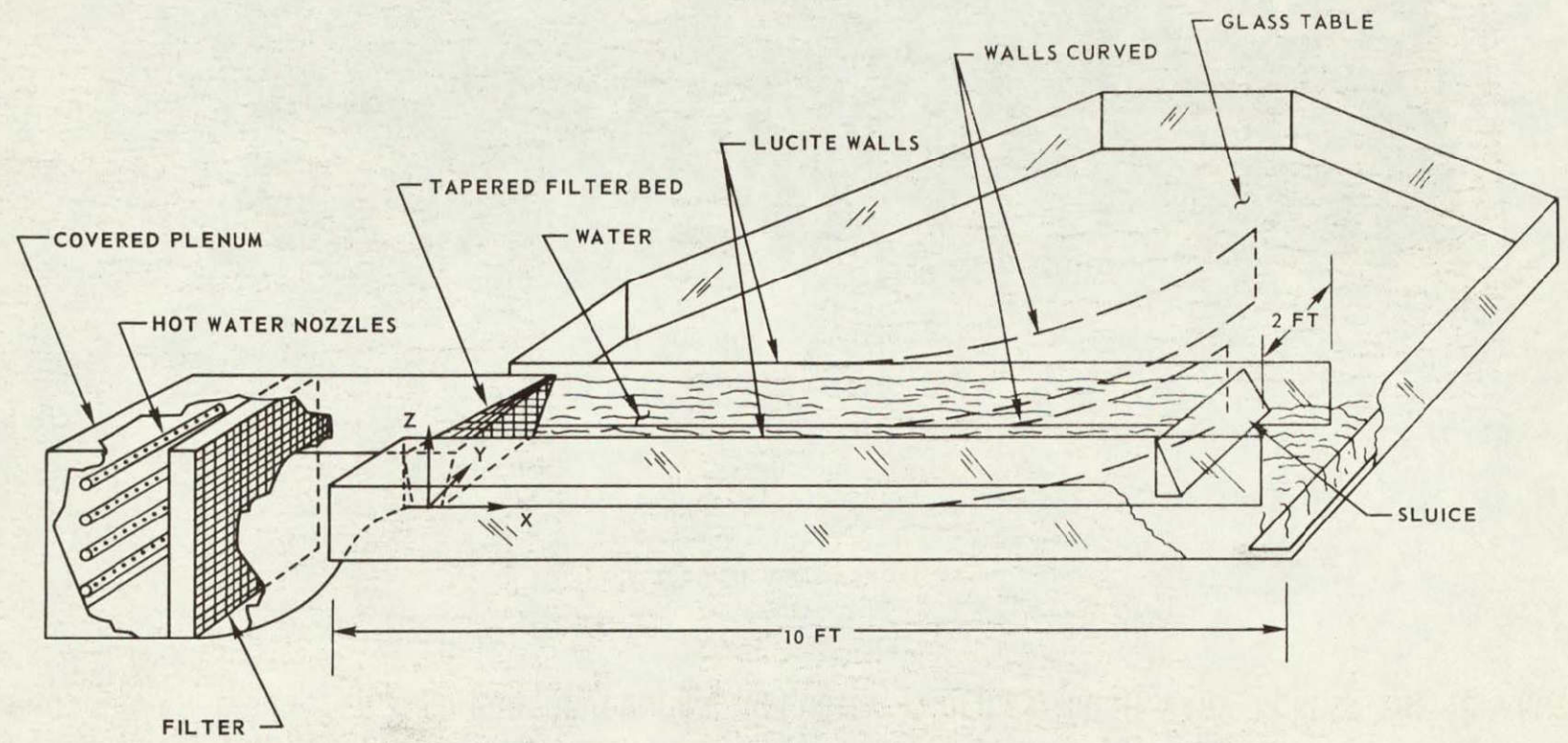
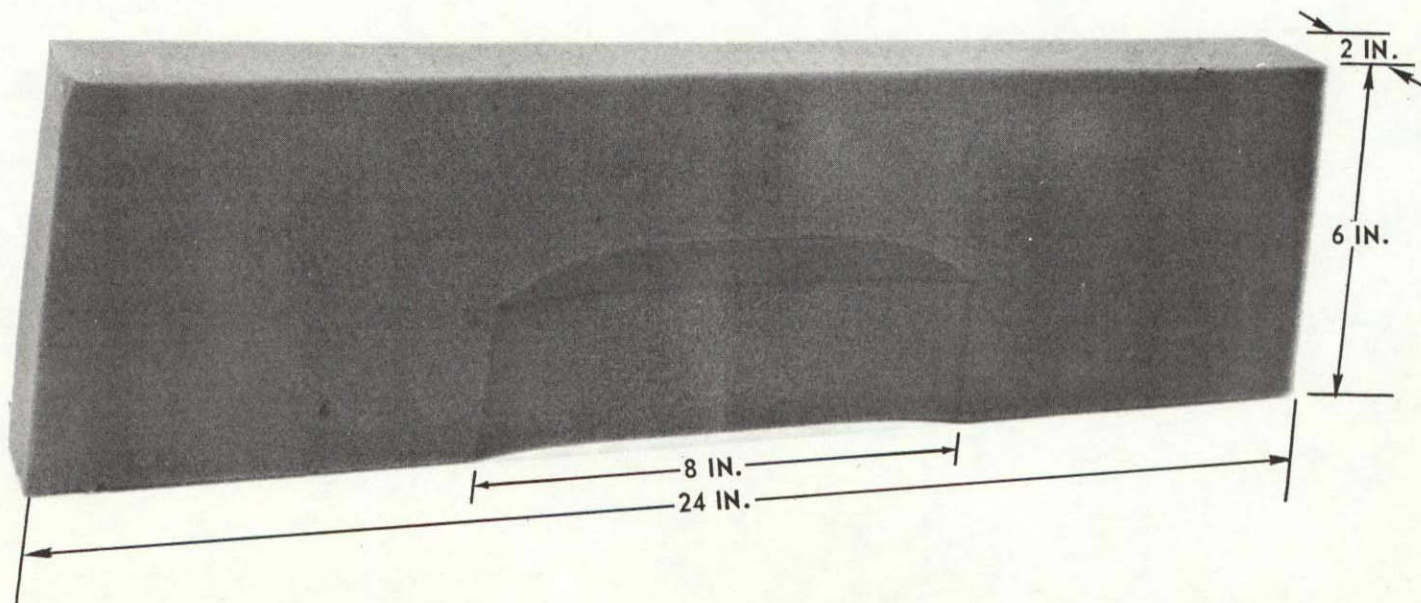


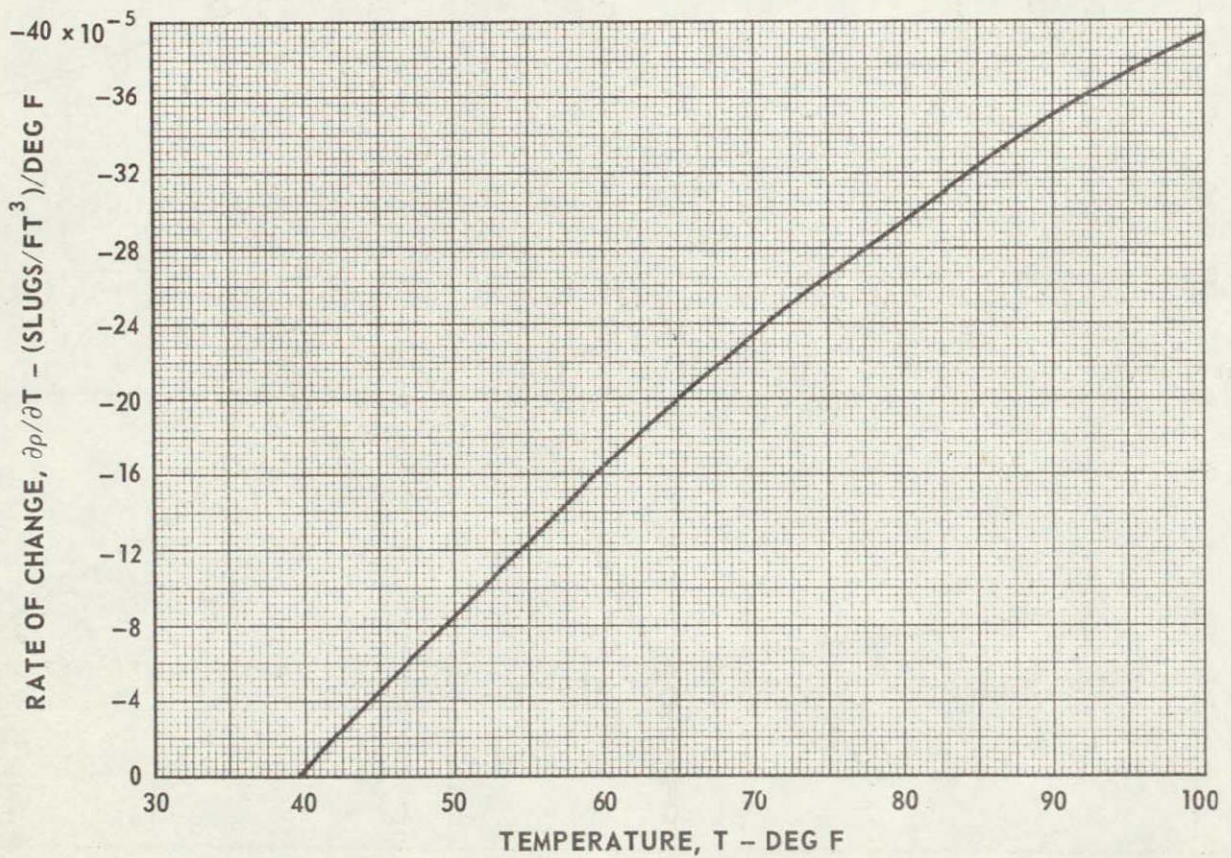
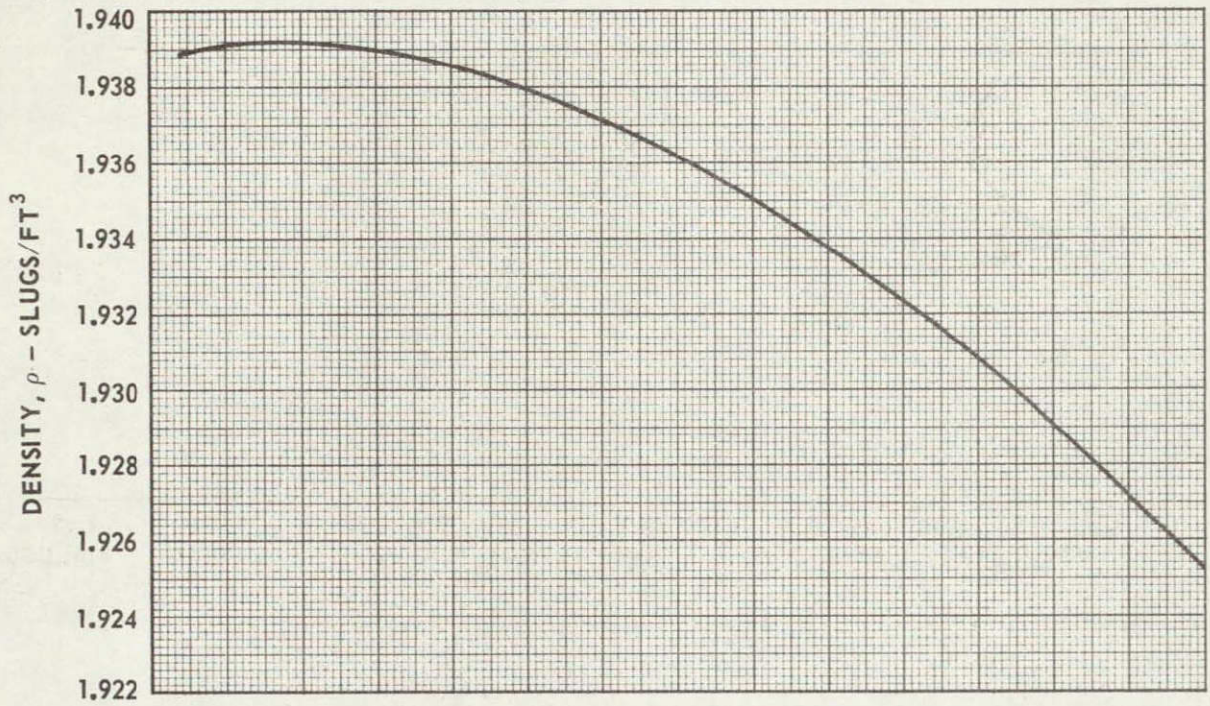
FIG. 30

PHOTOGRAPH OF FILTER BED FOR DEVELOPING VELOCITY PROFILES WHICH VARY ACROSS THE CHANNEL

ALL DIMENSIONS APPROXIMATE



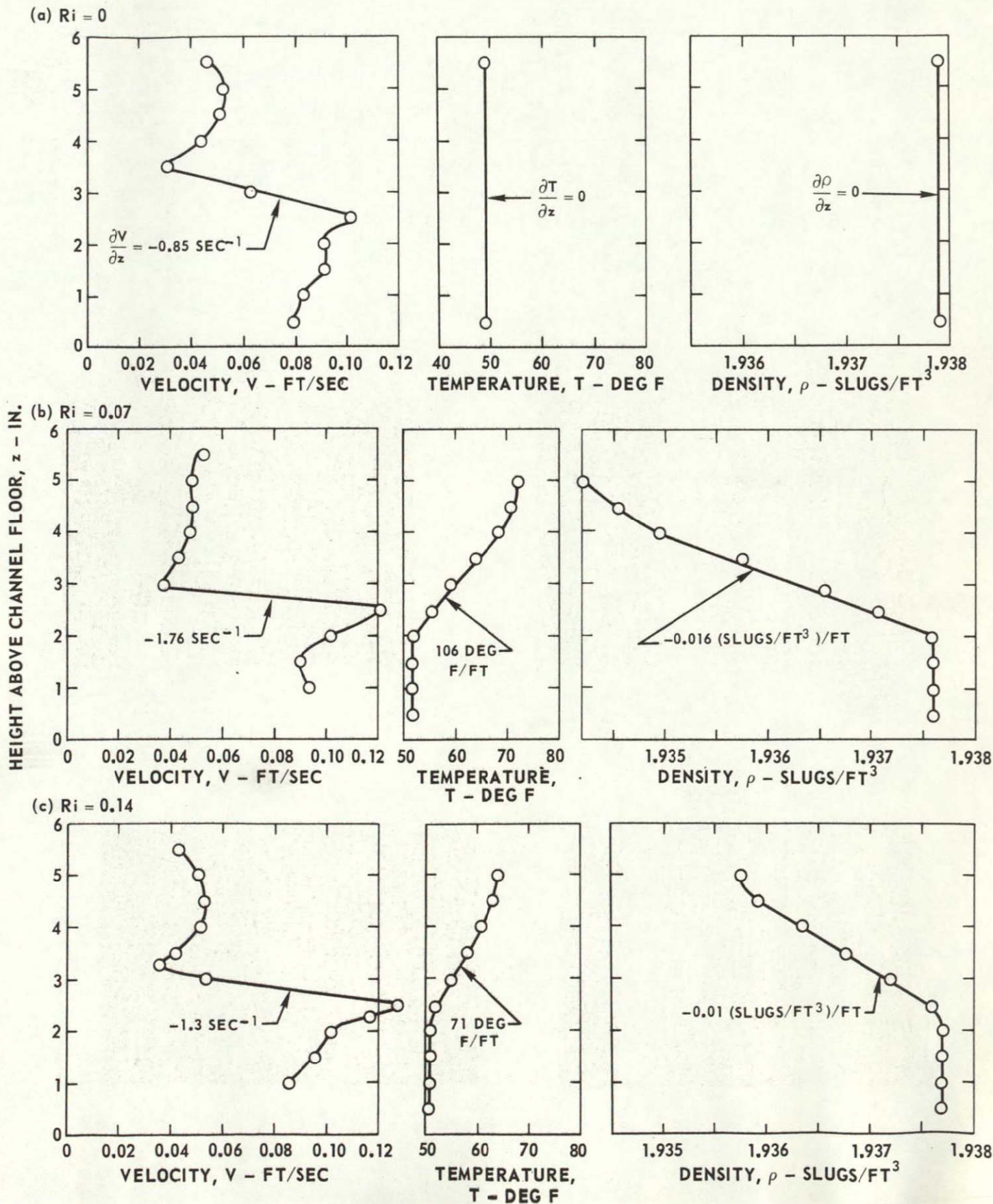
EFFECT OF TEMPERATURE ON PROPERTIES OF WATER



TYPICAL VELOCITY, TEMPERATURE AND DENSITY PROFILES FOR "THREE-DIMENSIONAL" SHEAR-FLOW EXPERIMENTS

ALL MEASUREMENTS 2 IN. DOWNSTREAM FROM TAPERED FILTER BED AT CENTER OF CHANNEL

THREE-DIMENSIONAL CUTOUT OF FILTER BED ONLY IN CENTER 1/3 OF CHANNEL SPAN (SEE FIG. 31)

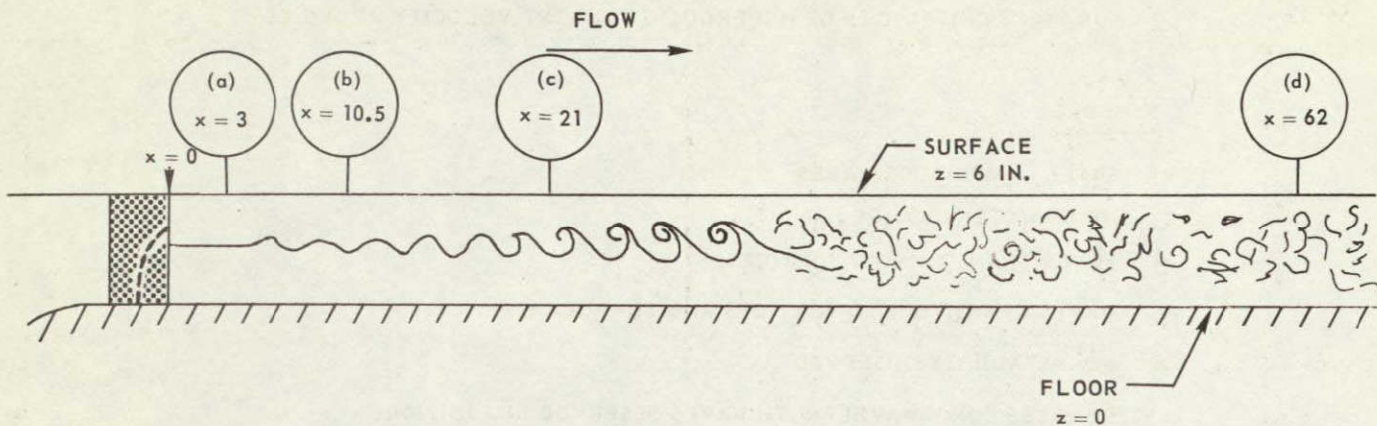


TYPICAL STAGES OF BREAKDOWN OF FLOW IN SHEAR LAYERS HAVING
 "THREE-DIMENSIONAL" VELOCITY PROFILES

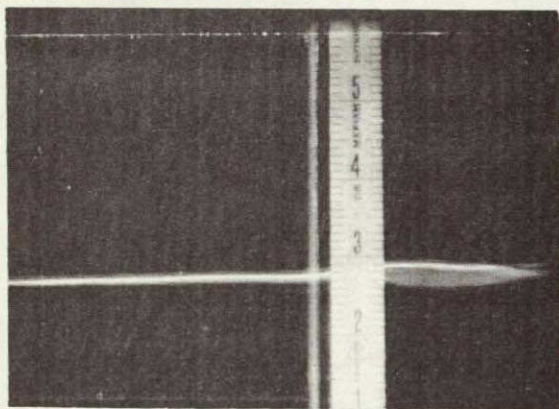
$V_0 = 0.07 \text{ FT/SEC}$

$\partial V / \partial z = 2.2 \text{ SEC}^{-1}$

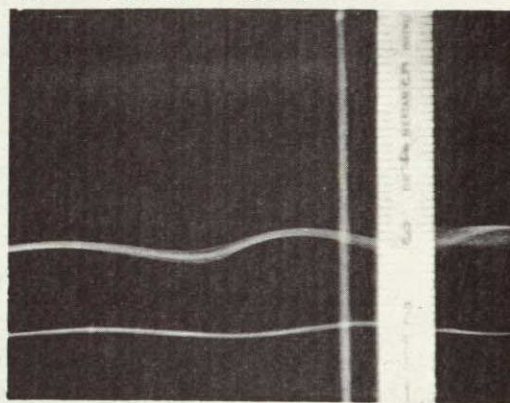
$\partial T / \partial z = 0$



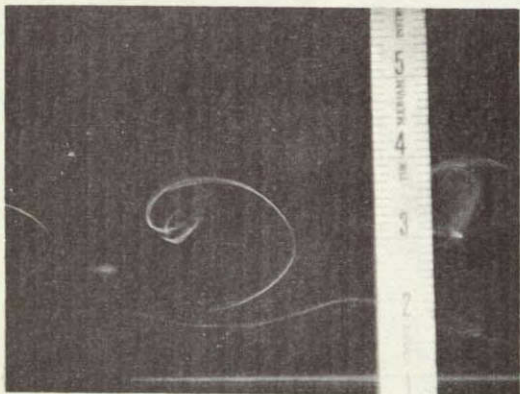
(a) x = 3 IN. - UNDISTURBED



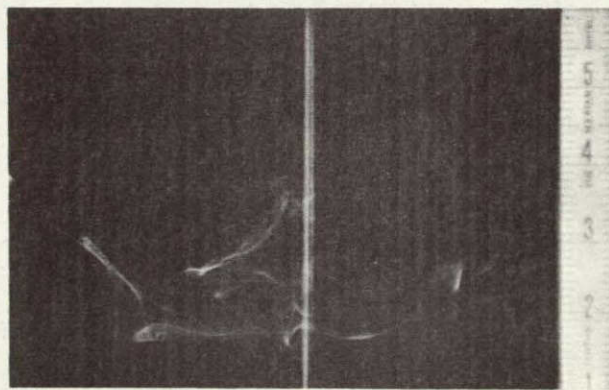
(b) x = 10.5 IN. - WAVES



(c) x = 21 IN. - VORTICES



(d) x = 62 IN. - TURBULENCE



COMPARISON OF WATER CHANNEL RESULTS FOR FLOWS HAVING "THREE-DIMENSIONAL" VELOCITY PROFILES WITH DRAZIN'S CRITERION FOR STABILITY OF TWO-DIMENSIONAL FLOWS

DRAZIN'S CRITERION FOR HYPERBOLIC TANGENT VELOCITY PROFILES

SYMBOLS

- SMALL -AMPLITUDE WAVES
 - ◊ INTERMITTENT WAVES
 - WAVES TRANSITION TO VORTICES
 - WAVES TRANSITION TO VORTICES AND TURBULENCE
 - × NO INSTABILITY OBSERVED
- (LW) DENOTES LONG-WAVELENGTH WAVES OBSERVED IN ADDITION TO CONDITION INDICATED BY SYMBOL

